

國立交通大學  
光電工程學系暨研究所  
博士論文

摻鎂氧化鋅材料之激子-聲子交互作用研究

Influence of phonons on excitonic characteristics in  
Mg-incorporated ZnO



研究生：潘晴如

指導教授：謝文峰 教授

中華民國九十七年一月

摻鎂氧化鋅材料之激子-聲子交互作用研究

Influence of phonons on excitonic characteristics in  
Mg-incorporated ZnO

研究生：潘晴如

Student : Ching-Ju Pan

指導教授：謝文峰 教授

Advisor : Dr. Wen-Feng Hsieh

國立交通大學

光電工程研究所



A Dissertation

Submitted to Department of Photonics and Institute of Electro-Optical Engineering  
College of Electrical Engineering and Computer Science  
National Chiao Tung University  
In Partial Fulfillment of the Requirements  
for the Degree of  
Doctor of Philosophy  
in  
Electro-Optical Engineering

January 2008  
Hsinchu, Taiwan, Republic of China

中華民國九十七年一月

## 誌謝

耶!!耶!!耶!!我終於畢業了~~好感動喔,終於完成求學生涯的最後一個階段。也即將邁入人生的另一個階段,工作賺錢嫁人去嚕^^。回想博士班生活的點點滴滴,所有的一切都還歷歷在目,要感謝的人、感動的事實在不勝枚舉。首先,我要非常感謝我的指導老師 謝文峰教授。老師真的是一位有教無類的好老師,能發掘每個學生潛藏的長處而將其發揮,不僅耐心的引領我找到研究方向,並且適當的訓練我在學術研究上建立一套邏輯性的思考模式,所謂一日為師終身為父丫,老師真的像一個爸爸ㄝ,特別是在天南地北的閒聊中感受最為明顯。然後我要感謝口試委員們對論文的指導及建議,使得論文更臻完善。很開心 周武清老師見證了我從大學、碩士班到博士班的求學歷程。再來我要謝謝雷射診測實驗室那些曾經陪伴我一起走過這些年的夥伴們:智章學長給我課業上的幫助,丫政學長以及吳俊毅學弟在我初踏入這個領域時的引導;林國峰在物理觀念及數據分析的無私分享與大力協助以及徐瑋澤學弟在實驗量測方面的幫忙;而黃同慶就像一個負責任的大家長,處理實驗室相當多的公務與雜事,感覺有他在實驗室就有大大的支柱呢,也謝謝他在我博士生涯最難熬的時候給我鼓勵,另外我們與楊松間許多吃喝玩樂的經驗分享也增添了刻板實驗室生活的色彩;此外玫丹、明容及盈璇學妹帶給我的歡樂仍然記憶猶新,妳們真是太好玩了!當然還有謝謝對我注入刺激的那些人,讓我更有動力往前邁進,在此祝福大家未來學業順利萬事順心~

最後我要感謝我親愛的爸爸媽媽偉大的奉獻與支持,拔拔我要回家陪你啦~~當然我也知道天上的媽媽一直默默的守護著我。感謝一直在我身旁給予我全部的那個人♥

# 摻鎂氧化鋅材料之激子-聲子交互作用研究

研究生：潘晴如

指導教授：謝文峰 教授

國立交通大學光電工程學系暨研究所

## 摘要

我們利用熱擴散與溶膠-凝膠法製備氧化鎂鋅合金半導體。利用拉曼散射與光激發光實驗研究氧化鎂鋅合金的晶格動力學、組成擾動以及激子相關特性(即激子與聲子、自由載子或其他激子的交互作用)在摻雜不同鎂成分之下的變化情形。我們藉由 x-光繞射與光激發光的光譜概略地估計氧化鎂鋅合金中鎂所取代鋅的比例。從室溫光激發光與吸收光譜譜峰的藍位移以及晶格常數的改變，可以證明鎂離子摻入氧化鋅晶體中而且成功地佔據鋅離子的位置。

一般來說，由於合金引起的組成成分擾動會使得拉曼光譜中各種聲子模態發生變化，如局部晶格改變引發的振動模態、因擾動而活化的振動模態、聲子頻率的位移、譜形變寬與不對稱等特性。因此，我們利用拉曼光譜分析當鎂摻入氧化鋅奈米結構後，氧化鎂鋅晶格振動模態的變化情形。除了氧化鋅原有的聲子模態之外，我們亦觀察到  $383$  與  $510\text{ cm}^{-1}$  兩個異常的聲子模態，據推測可能來自於鎂相關的振動模。由於鎂離子與鋅離子在半徑上的差異，鎂的摻入會產生某些新的晶格缺陷抑或是原有的晶格缺陷因擾動而活化進而出現一些額外的振動模。

我們用spatial correlation model探討組成成分的擾動造成拉曼光譜譜形變寬與不對稱的行為;而這個理論模型的概念是考慮聲子的傳播受到合金位能異動(alloy potential fluctuations)的侷限與晶粒分布(grain size distribution)的影響。因此可藉由分析氧化鎂鋅奈米粉末摻鎂的含量多寡與 $E_2(\text{high})$ 聲子的頻率變化之關聯性得知。我們發現隨著鎂含量的增加,合金位能異動造成晶粒相對變小,那是由於受到氧化鎂對氧化鋅溶解度的限制。多餘的鎂離子無法取代氧化鋅晶體中鋅離子的位置因而形成氧化鎂群環繞氧化鎂鋅晶體。

在輻射放光過程中雙激子(biexciton)的產生是束縛兩個激子形成,因此激發能量與輻射放光的強度之間會有接近於2的一個理想指數關係。我們在氧化鋅粉末中觀察到聲學聲子(acoustic phonon)與光學聲子(optical phonon)在雙激子形成的過程中扮演著不可或缺的角色。研究發現當溫度低於某個程度,也就是激子動能低於光學聲子動能時,激子或載子(carriers)冷卻(relaxation or cooling)過程僅有聲學聲子的放射,此時的指數值是小於1的;然而當溫度提高到使得激子動能接近於光學聲子最低動能的時候,激子或載子冷卻過程多了光學聲子的參與,此時的指數值則是接近於理論上的理想值。

最後,我們使用變溫光激發光光譜研究摻雜不同鎂成分的氧化鎂鋅粉末其激子與縱光學聲子(longitudinal optical phonon)耦合強度的變化。激子與縱光學聲子的耦合強度可經由分析激子的能量隨著溫度變化所產生的位移來決定。除此之外,觀察到隨著鎂成分的提高激子的束縛能相對增加,其原因可能是激子位能受到合金引發的組成擾動而產生變化。激子束縛能的增加是由於激子波爾半徑(Bohr radius)的減小造成激子極性減弱所致,因而降低了激子與縱光學聲子的耦合強度。

# Influence of phonons on excitonic characteristics in Mg-incorporated ZnO

Student: Ching-Ju Pan

Advisor: Dr. Wen-Feng Hsieh

Department of Photonics & Institute of Electro-Optical Engineering  
National Chiao Tung University

## Abstract

MgZnO alloys with various Mg contents were successfully synthesized using thermal diffusion and sol-gel methods. We investigated on the lattice dynamics, compositional disorder, and exciton-related characteristics (i.e., interactions between excitons and acoustic phonons, LO phonons, free carriers and other excitons) of the  $\text{Mg}_x\text{Zn}_{1-x}\text{O}$  alloy semiconductors which depend critically on the Mg substitution using Raman and photoluminescence spectroscopy. Alloy compositions can be estimated from X-ray diffraction patterns and photoluminescence spectra. The blueshift of near-band-edge emission and excitonic absorption along with the variation of lattice parameters reveal that  $\text{Mg}^{2+}$  is incorporated into the ZnO host lattice and substitutes for  $\text{Zn}^{2+}$ .

In ternary semiconductor alloys, the Raman spectra show changes of various phonon modes with compositional disorder, including emergence of local vibration modes and disorder-activated modes, a shift in phonon frequency and changes of the linewidth and asymmetry. In addition to the host phonons of ZnO, two anomalous modes around 383 and 510  $\text{cm}^{-1}$  are presumably attributed to the Mg-related vibrational modes. Due to the differences in the ionic radii of Mg impurity and host

ions, the Mg-induced extrinsic or intrinsic lattice defects in either substitutional sites or the interstitial sites would become activated. As a result, disorder-activated scattering or local lattice vibration occur in Raman scattering.

The broadening in linewidth and asymmetry can be investigated in terms of the modified spatial correlation model based on the finite correlation length of a propagation phonon due to the alloy potential fluctuations and grain size distribution. The microscopic nature of the substitutional disorder is discussed by analyzing the compositional dependence of the  $E_2(\text{high})$  phonon mode in  $\text{Mg}_x\text{Zn}_{1-x}\text{O}$  submicropowders. With increasing Mg concentration, the alloy potential fluctuations lead to a decrease in the grain size, which is induced by the surplus  $\text{Mg}^{2+}$  that could form MgO clusters surrounding the MgZnO crystalline.

Moreover, it is well known that efficient exciton relaxation is required for bounding two cooled excitons to form biexciton. Acoustic and optical phonon scattering playing key roles in exciton relaxation are responsible for formation of biexcitons at various temperatures. Using ZnO powders, we observed a sublinear dependence on excitation power at low temperature, in which the relaxation process involves only emission of acoustic phonons due to the excitons having kinetic energy lower than those of the optical phonons. However, the exponent comes near theoretical value of 2 for participation of optical phonons when the exciton kinetic energy approaches to the energy of the lowest optical phonon.

Finally, the coupling between exciton and longitudinal optical (LO) phonon was investigated in use of the temperature-dependent photoluminescence from  $\text{Mg}_x\text{Zn}_{1-x}\text{O}$  powders ( $0 \leq x \leq 0.05$ ). The exciton binding energy increases to 73 meV for 5 at. % Mg incorporated powders. It is suggested that the localization of excitons originating from the compositional fluctuation takes place in  $\text{Mg}_x\text{Zn}_{1-x}\text{O}$  alloys. The

strength of exciton-LO-phonon coupling was deduced from the energy shift of exciton emission with temperature variation. The increase of the exciton binding energy results from decrease of the exciton Bohr radius that is responsible for reducing the coupling strength of exciton-LO-phonon as increasing Mg content.





# Contents

Abstract in Chinese.....	I
Abstract in English .....	III
Contents.....	VI
List of Figures.....	X
List of Tables.....	XIII
<b>Chapter 1 Introduction.....</b>	<b>1</b>
1.1 Basic properties of ZnO and general review of $Mg_xZn_{1-x}O$ materials.....	
1	
1.1.1 Basic properties of ZnO.....	1
1.1.2 General review of $Mg_{1-x}Zn_xO$ materials.....	3
1.2 Motives.....	6
1.3 Organization of the dissertation.....	7
References.....	9
<b>Chapter 2 Theoretical background.....</b>	<b>13</b>
2.1 Crystal structures and Lattice dynamics.....	13
2.1.1 Crystal structures.....	13
2.1.2 Selection rules and phonon modes.....	
.....15	
2.1.3 Polar-optical phonons: Fröhlich interaction.....	20
2.2 Fundamental optical transitions.....	24
2.2.1 General conceptions.....	24
2.2.2 Exciton-related emission .....	26

2.2.2.1 Free excitons and polaritons.....	27
2.2.2.2 Bound excitons.....	31
2.2.2.3 Two-electron satellites.....	33
2.2.2.4 LO-phonon replicas.....	35
2.2.3 Defect emission.....	36
2.2.4 Biexciton and exciton-exciton scattering.....	38
References .....	42
<b>Chapter 3 Experimental procedures and characterization techniques.....</b>	<b>44</b>
3.1 Synthesis mechanism .....	44
3.1.1 Vapor-Liquid-Solid (VLS) method.....	44
3.1.2 Sol-gel process.....	45
3.2 Sample preparation.....	48
3.2.1 ZnMgO nanostructures formed by Mg in-diffused ZnO nanowires.....	48
3.2.2 Mg <sub>x</sub> Zn <sub>1-x</sub> O nanopowders synthesized by varying volume ratio of MgO/ ZnO.....	49
3.2.3 Mg <sub>x</sub> Zn <sub>1-x</sub> O powders synthesized by varying molar ratio of Mg/Zn.....	49
3.3 Characterization of lattice dynamics .....	50
3.3.1 X-ray Diffraction .....	50
3.3.2 Scanning Electron Microscopy .....	50
3.3.3 Raman scattering measurement .....	50
3.4 Characterization of optical properties .....	52
3.4.1 Photoluminescence system .....	52
3.4.2 Optical absorption system .....	52
References .....	54

<b>Chapter 4 Raman study of Mg incorporation in MgZnO alloys.....</b>	<b>56</b>
4.1 Structural and optical properties of ZnMgO nanostructures formed by Mg in-diffused ZnO nanowires.....	57
4.1.1 Morphology.....	57
4.1.2 Determination of Mg concentration.....	59
4.1.3 Raman spectra analysis.....	62
4.2 Raman study of alloy potential fluctuations in $Mg_xZn_{1-x}O$ submicropowders.....	65
4.2.1 Morphology and bandgap modulation.....	66
4.2.2 Raman spectra analysis.....	68
4.3 Summary.....	73
References .....	75
<b>Chapter 5 Acoustic and optical phonon assisted formation of biexcitons.....</b>	<b>78</b>
5.1 Morphology and temperature-dependent photoluminescence.....	79
5.2 Excitation-power-dependent photoluminescence.....	81
5.3 Photoluminescence spectra analysis.....	83
5.4 Summary.....	86
References .....	87
<b>Chapter 6 Reducing exciton–longitudinal optical phonon coupling with increasing Mg incorporation in MgZnO powders.....</b>	<b>89</b>
6.1 Morphology and temperature-dependent photoluminescence.....	90
6.2 Binding energy.....	93
6.3 Photoluminescence spectra analysis.....	95
6.4 Summary.....	98
References .....	99

**Chapter 7 Conclusion and Prospective.....101**  
7-1 Conclusion.....101  
7-2 Prospective.....104  
References.....107  
  
**Resume .....109**  
**Publication list.....110**



## List of Figures

Fig. 1-1 The wurtzite structure model of ZnO.....	1
Fig. 1-2 Typical room temperature PL spectrum of ZnO.....	3
Fig. 1-3 Tentative form of the system MgO-ZnO.....	5
Fig. 2-1 Schematic representation of a wurtzite ZnO structure.....	15
Fig. 2-2 Phonon dispersion curves for ZnO crystal of wurtzite structure.....	18
Fig. 2-3 Displacement vectors of the phonon modes in ZnO wurtzite structure.....	19
Fig. 2-4 A pair excitation in the scheme of valence and conduction band in the exciton picture for a direct gap semiconductor.....	26
Fig. 2-5 The electronic band structure of wurtzite ZnO.....	28
Fig. 2-6 Free excitonic fine structure region of the 10 K PL spectrum for the ZnO single crystal.....	29
Fig. 2-7 Dispersion curves of exciton and exciton polaritons.....	31
Fig. 2-8 Bound excitonic region of the 10 K PL spectrum for the ZnO single crystal.....	32
Fig.2-9 10 K PL spectrum in the TES region of the main bound exciton lines.....	34
Fig.2-10 10 K PL spectrum in the region where DAP transition and LO-Phonon replicas are expected to appear.....	3
Fig.2-11 Inelastic scattering processes in the intermediate density regime: biexciton decay and inelastic exciton-exciton scattering.....	39
Fig.2-12 PL spectra of a ZnO epilayer for various excitation intensities at 77 K.....	40
Fig. 3-1 Vapor-Liquid-Solid method.....	45
Fig.3-2 Schematic of the routes that one could follow within the scope of sol-gel processing.....	47

Fig. 3-3 XRD $\omega$ - $2\theta$ scans geometry.....	50
Fig. 3-4 The scheme of the Raman system.....	51
Fig. 3-5 PL detection system.....	52
Fig. 3-6 Optical absorption system.....	53
Fig. 4-1 The SEM images of the Mg in-diffused ZnO nanowires. The inset shows the original aligned ZnO nanowires.....	58
Fig. 4-2 The Rietveld refinement plot of ZMO nanostructures and ZnO nanowires...	59
Fig. 4-3 The normalized room-temperature PL spectra of ZMO nanostructures and ZnO nanowires.....	61
Fig. 4-4 The Raman spectra of ZMO nanostructures and ZnO nanowires.....	62
Fig. 4-5 The SEM image of the 10.9% Mg sample.....	66
Fig. 4-6 Photoluminescence and absorption spectra of $Mg_xZn_{1-x}O$ alloys for different MgO/ZnO volume ratios.....	67
Fig. 4-7 The calculated Mg content in the $Mg_xZn_{1-x}O$ submicropowders as a function of the MgO/ZnO volume ratio.....	68
Fig. 4-8 Micro-Raman spectra of the $Mg_xZn_{1-x}O$ submicropowders with various Mg contents .....	69
Fig. 4-9 Experimental and calculated line shapes of the $E_2(\text{high})$ band for $Mg_xZn_{1-x}O$ submicropowders with $x = 6\%$ , $11\%$ , and $13\%$ .....	71
Fig. 4-10 Linewidth $\Delta\tau$ and correlation length $L_o$ of $E_2(\text{high})$ phonon as a function of Mg concentration.....	72
Fig. 5-1 The SEM image of the ZnO powders.....	79
Fig. 5-2 Temperature dependence of PL spectra in ZnO powders.....	80
Fig. 5-3 Dependence of the PL spectra on the excitation power measured at 10 K....	81
Fig. 5-4 Dependence of PL spectra on excitation power measured at 80 K.....	82

Fig. 5-5 Integrated emission intensity of biexciton as a function of excitation power under various temperatures.....	83
Fig. 5-6 Experimental and calculated exciton energies plotted against inverse temperature.....	85
Fig. 6-1 The SEM image of the 5% Mg sample.....	90
Fig. 6-2 Temperature dependence of PL spectra in ZnO powders.....	92
Fig. 6-3 Temperature dependence of PL spectra in Mg <sub>0.05</sub> Zn <sub>0.95</sub> O powders.....	93
Fig. 6-4 Normalized integrated intensity of ZnO sample as a function of temperature.....	94
Fig. 6-5 Normalized integrated intensity of Mg <sub>0.05</sub> Zn <sub>0.95</sub> O sample as a function of temperature.....	94
Fig. 6-6 Diagram of exciton-phonon interaction in the unit cell.....	95
Fig. 6-7 Dependence of PL peak energy positions on temperature for the Mg <sub>x</sub> Zn <sub>1-x</sub> O alloys.....	96
Fig. 6-8 The coupling strength of the exciton-LO-phonon given as the average ratio $\lambda_{\text{ratio}} = \lambda_{\text{Mg}_x\text{Zn}_{1-x}\text{O}}/\lambda_{\text{ZnO}}$ for comparison with the exciton Bohr radius $a_{\text{EB}}$ .....	97

## List of Tables

Table 1-1 Properties of wurtzite ZnO.....	2
Table 2-1 Phonon mode frequencies of wurtzite ZnO at the center of the Brillouin zone obtained from infrared spectroscopic ellipsometry and Raman scattering measurements in comparison with theoretical predictions.....	19
Table 4-1 Phonon modes frequencies in our work and tentative assignments of all the peaks.....	63
Table 6-1 Summary of the results of the temperature-dependent photoluminescence characterization.....	97





# Chapter 1 Introduction

## 1.1 Basic properties of ZnO and general review of $Mg_xZn_{1-x}O$ materials

### 1.1.1 Basic properties of ZnO

The ZnO crystal has wurtzite structure as schematically shown in Fig. 1-1 with lattice constants of  $a = 3.249 \text{ \AA}$  and  $c = 5.207 \text{ \AA}$ . The gray and red spheres denote Zn and O atoms, respectively. The center picture of Fig. 1-1 displayed the top view image parallel to the  $z$ -axis, i.e.,  $c$ -axis, while the right-most picture displayed the side view image perpendicular to the  $z$ -axis. The detailed discussion and crystal structure can be seen in Section 2.1.

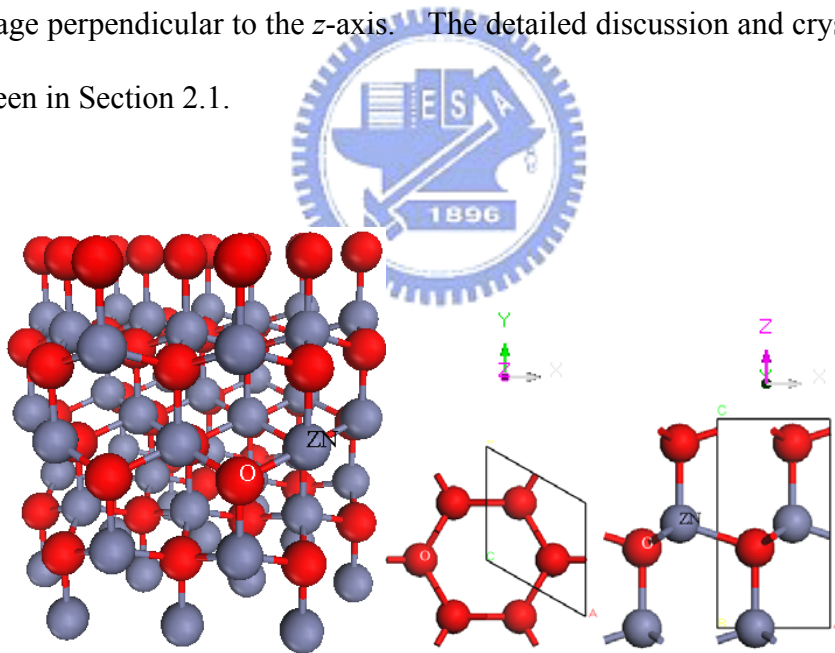


Fig. 1-1 The wurtzite structure model of ZnO.

The basic materials parameters of ZnO are shown in Table 1-1. ZnO is a direct band gap semiconductor with  $E_g = 3.37 \text{ eV}$  at room temperature (RT). The band gap of ZnO can be tuned via divalent substitution on the cation site to produce heterostructures. Cd doping will decrease the band gap to as low as 3.0 eV, whereas

Mg doping increase the band gap to as high as 4.0 eV. Electron doping in nominally undoped ZnO has been attributed to Zn interstitials, oxygen vacancies, or hydrogen. The intrinsic defect levels that lead to *n*-type doping lie approximately at around 0.01-0.05 eV below the conduction band. The optical properties of ZnO, studied using photoluminescence (PL), photoconductivity, and absorption reflect the intrinsic direct band gap, a strongly bound exciton state, and gap states arising from point defects. Shown in Fig. 1.2 is the typical RT PL spectrum. A strong RT, near-band-edge (NBE) UV photoluminescence peak at  $\sim 3.2$  eV is attributed to an exciton state, as the exciton binding energy is  $\sim 60$  meV. In addition, visible emission is also observed as a result of defect states. The detailed optical transitions of PL spectrum will be further discussed in Section 2.2.

Table 1-1 Properties of wurtzite ZnO. [1]

Property	Value
Lattice parameters at 300 K:	
$a_0$	0.32495 nm
$c_0$	0.52069 nm
$a_0/c_0$	1.602 (1.633 for ideal hexagonal structure)
$u$	0.345
Density	5.606 g/cm <sup>3</sup>
Stable phase at 300 K	wurtzite
Melting point	1975°C
Thermal conductivity	0.6, 1-1.2
Linear expansion coefficient (/°C)	$a_0$ : $6.5 \times 10^{-6}$ , $c_0$ : $3.0 \times 10^{-6}$
Static dielectric constant	8.656
Refractive index	2.008, 2.029
Energy gap	3.4 eV (direct)
Intrinsic carrier concentration	$< 10^6$ /cm <sup>3</sup>
Exciton binding energy	60 meV
Electron effective mass	0.24
Electron Hall mobility at 300 K for low <i>n</i> -type conductivity	200 cm <sup>2</sup> /V·s
Hole effective mass	0.59
Hole Hall mobility at 300 K for low <i>p</i> -type conductivity	5-50 cm <sup>2</sup> /V·s

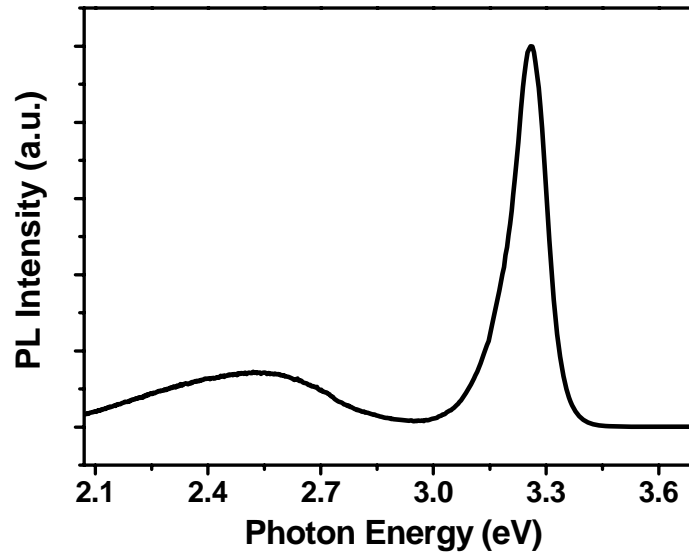


Fig. 1-2 Typical room temperature PL spectrum of ZnO.

### 1.1.2 General review of $\text{Mg}_{1-x}\text{Zn}_x\text{O}$ materials

ZnO is a direct band gap semiconductor with optical properties similar to GaN. Its high band gap energy of 3.37 eV at RT [2] and free-exciton binding energy of 60 meV [3] (much larger than that of GaN  $\sim$  26 meV) along with its larger absorption coefficient compared to GaN make ZnO a promising candidate for the development of short-wavelength photonic devices, such as ultraviolet detectors, light-emitting diodes (LEDs), and laser diodes (LDs). The large exciton binding energy has enabled observation of laser action and/or stimulated emission of exciton at temperatures well above RT in ZnO thin films [4-6] and in ZnO/(Mg,Zn)O superlattices (SLs) [7]. A lower lasing threshold can be expected, if exciton-related recombination is used, rather than recombination of an electron-hole plasma, which is the dominant mechanism of laser action in (In,Ga)N devices. Therefore, it is expected that a ZnO-based light emitter should be much brighter than its counterpart of GaN light emitter. Furthermore, the recent availability of large size high crystalline quality bulk ZnO can also be considered as an advantage not only for homoepitaxial ZnO

growth, but also for GaN growth due to its potential as a suitable substrate with similar crystalline properties.

ZnO is typically *n*-type and attempts to fully utilize ZnO-based technologies; *p*-type doping and band gap engineering are still the remaining issues in modern optoelectronics. Jingbo *et al.* [8] proposed that, using the first-principles band-structure calculations, the *p*-type dopability of ZnO can be improved by lowering the ionization energy of acceptors in ZnO by codoping acceptors with donor or isovalent atoms (e.g., Mg or Be). Many groups have successfully achieved *p*-type ZnO by single doping of I or V group elements, such as N [9-15], P [16-19], As [20-23], Li [24], etc., and by codoping of III-N groups, such as Al-N, Ga-N etc [25,26]. ZnO *p-n* junction LEDs have also been produced by using N-doped *p*-type ZnO recently, which emit blue or yellow light.[27-29] However, the dominant emissions do not come from near-band-edge (NBE) recombination but is related to defects with deep levels. To obtain strong NBE violet emission and even high effective UV laser, it is necessary to prepare LED and LD with active layers of ZnO SL or quantum well (QWs), which need high quality *p*-type ZnO and *p*-type ZnO alloy barrier materials. Lately, *p*-type ZnMgO has been achieved by doped with N, P, Li, and Sb elements.[30-33]

Moreover, band gap modulation has played an important role in modern optoelectronics since the emergence of SLs and QWs. The widely used semiconductors GaN and GaAs both have their counterparts of AlGaN and AlGaAs with adjustably enlarged band gap to combine with to fabricate various heterostructures so as to realize desired functions. In recent years, alloying the ZnO with MgO has been investigated for widening the band gap of ZnO-based structures by adjusting the Mg concentration. MgO ( $E_g = 7.8$  eV) has a NaCl type cubic

structure with the lattice constant of  $a = 4.24 \text{ \AA}$ , while ZnO has a wurtzite structure. According to the phase diagram of ZnO-MgO binary system shown in Fig. 1-3, the thermodynamic solubility limit of MgO in ZnO is less than 4 mol % in the bulk form.[34] However, ionic radius of  $\text{Mg}^{2+}$  ( $0.57 \text{ \AA}$ ) is similar to that of  $\text{Zn}^{2+}$  ( $0.60 \text{ \AA}$ ), which may allow by significant replacement of one another. In spite of a large structural dissimilarity between ZnO and MgO, the successful growth of ternary solid solutions  $\text{Mg}_x\text{Zn}_{1-x}\text{O}$  with metastable wurtzite for Mg compositions up to  $x = 0.45$  or with zinc blende crystals for  $x > 0.5$  as demonstrated by Koike *et al.* [35] and Choopun *et al.* [36], respectively.

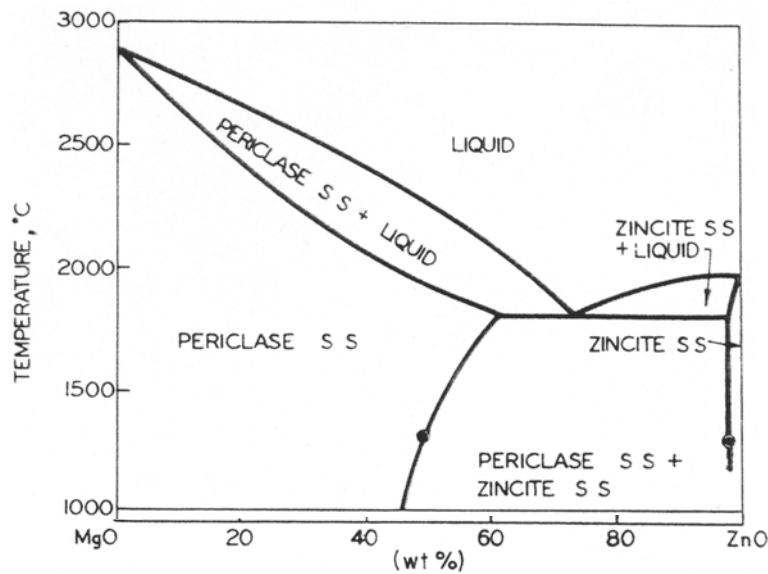


Fig. 1-3 Tentative form of the system MgO-ZnO.

(Mg,Zn)O alloys have been proved feasible to realize the band gap modulation of ZnO. So MgZnO can be used as barrier layers for carrier confinement. For example, Lim *et al.* [37] demonstrated the operation of the ZnO light-emitting devices emitted 380 nm UV light at room temperature with a turn-on voltage of 3.2 V. The intensity of near band edge emission was increased further and greatly suppressed the

deep level emission by using  $\text{Mg}_{0.1}\text{Zn}_{0.9}\text{O}$  layers as energy barrier layers to confine the carriers to the high-quality *n*-type ZnO.  $\text{ZnO}/\text{Mg}_{0.2}\text{Zn}_{0.8}\text{O}$  coaxial nanorod single quantum well structures were reported by Bae *et al.* [38], who proposed that the quantum confinement effect would depend on the  $\text{Mg}_{0.2}\text{Zn}_{0.8}\text{O}$  barrier layer thickness as well as the ZnO well layer thickness. Additionally, they are also very promising materials for use as active layers in double heterostructures, not only as barrier layers, e.g., Shibata *et al.* [39] reported high-quality  $\text{Zn}_{1-x}\text{Mg}_x\text{O}$  alloys are very brilliant light emitters, even more brilliant than ZnO, particularly in the high-temperature region. The authors have revealed that the increase in the oscillator strength is mainly due to the increase in the activation energy required for the nonradiative recombination processes. It is inferred that the localization of excitons originating from the compositional fluctuation takes place in  $\text{Zn}_{1-x}\text{Mg}_x\text{O}$  alloys. 347 nm UV electroluminescence resulted from the NBE emission of  $\text{Mg}_x\text{Zn}_{1-x}\text{O}$  was realized on a  $\text{Mg}_x\text{Zn}_{1-x}\text{O}$ -based metal-insulator ( $\text{SiO}_2$ )-semiconductor (MIS) structure on a silicon substrate. Therefore, these applications require a full understanding of optical and structural properties of  $\text{MgZnO}$  materials.

## 1.2 Motives

Since Raman scattering can yield important information about the nature of the solid on a scale of the order of a few lattice constants, it can be used to study the microscopic nature of structural and/or topological disorder. Raman scattering thus has been widely used to study the local lattice vibration and alloy potential fluctuations of substitutional semiconductor alloys. Besides, PL measurement is a suitable tool to determine the crystalline quality and the presence of impurities in the material as well as exciton fine structures. It is imperative to fully characterize the

excitons in ZnO since not only are excitons a sensitive indicator of material quality but also they play an important role in the stimulated emission and gain processes in real device structures. Especially, the exciton-phonon interaction has significant influence on the optical properties of alloy semiconductors.

To date, little is known about the influence of phonons on optical characteristics in the  $\text{Mg}_x\text{Zn}_{1-x}\text{O}$  ternary solid solutions. A precise knowledge of fundamental material parameters is essential, in particular, the lattice dynamic properties, exciton-related parameters, and the exciton-phonon interaction as Mg was introduced into the ZnO. In the dissertation, the MgZnO samples were prepared by the vapor-phase transport and sol-gel process as described in the experimental procedures of the sample preparation in the later chapter. We will investigate the interesting optical features of *local lattice structure, Raman vibrational properties, alloy potential fluctuations, and exciton-LO-phonon coupling* in use of Raman and PL spectroscopy.



### **1.3 Organization of the dissertation**

This dissertation is organized as follows. Chapter 2 presents a general concept of crystal structures, lattice dynamics, and fundamental optical transitions. Optical transitions in ZnO systems are reviewed in terms of PL features, including exciton-related emissions, defect-related transitions, biexciton and exciton-exciton scattering. In Chapter 3, the synthesis of the MgZnO alloys with different processes is demonstrated. We also show the brief illustrations of characterization techniques. In Chapter 4, the band gap modulation of the  $\text{Mg}_x\text{Zn}_{1-x}\text{O}$  alloys is discussed. The changes of lattice structure and vibrational properties of ZnO caused by Mg incorporation are also investigated. The Mg-related lattice vibrations and the nature

of the alloy potential fluctuations are demonstrated by Raman study. Chapter 5 elucidates a detailed discussion on the formation of biexciton assisted by acoustic and optical phonon scatterings. In Chapter 6, we discuss the increase of exciton binding energy may result from the decrease of exciton Bohr radius making the exciton less polar thereby reducing the coupling to LO phonons. Reducing exciton-LO phonon coupling with increasing Mg substitution in MgZnO powders will be explained. In the final Chapter 7, we conclude the studies on the MgZnO alloys and propose the several topics of the future work.





## References

- [1] D. P. Norton, Y. W. Heo, M. P. Ivill, K. Ip, S. J. Pearton, M. F. Chisholm, and T. Steiner, *Materials Today* **34** (2004).
- [2] Y. F. Chen, D. M. Bagnall, H. Koh, K. Park, K. Hiraga, Z. Zhu, and T. Yao, *J. Appl. Phys.* **84**, 3912 (1998).
- [3] K. Hümmer, *Phys. Status Solidi B* **56**, 249 (1943).
- [4] P. Yu, Z. K. Tang, G. K. L. Wong, M. Kawasaki, A. Ohtomo, H. Koinuma, and Y. Segawa, in *Proceedings of the 23rd International Conference on Physics of Semiconductors, Berlin*, edited by M. Scheffler and R. Zimmermann (World Scientific, Singapore, 1996), Vol. 2, p. 1453.
- [5] P. Yu, Z. K. Tang, G. K. L. Wong, M. Kawasaki, A. Ohtomo, H. Koinuma, and Y. Segawa, *Solid State Commun.* **103**, 459 (1997).
- [6] D. M. Bagnall, Y. F. Chen, Z. Zhu, T. Yao, S. Koyama, M. Y. Shen, and T. Goto, *Appl. Phys. Lett.* **70**, 2230 (1997).
- [7] A. Ohtomo, K. Tamura, M. Kawasaki, T. Makino, Y. Segawa, Z. K. Tang, G. Wong, Y. Matsumoto, and H. Koinuma, *Appl. Phys. Lett.* **77**, 2204 (2000).
- [8] J. Li, S. H. Wei, S. S. Li, and J. B. Xia, *Phys. Rev. B* **74**, 081201 (2006).
- [9] A. Tsukazaki, A. Ohtomo, T. Onuma, M. Ohtani, T. Makino, M. Sumiya, K. Ohtani, S. F. Chichibu, S. Fuke, Y. Segawa, H. Ohno, H. Koinuma, and M. Kawasaki, *Nat. Mater.* **4**, 42 (2005).
- [10] J. M. Bian, X. M. Li, C. Y. Zhang, W. D. Yu, and X. D. Gao, *Appl. Phys. Lett.* **85**, 4070 (2004).
- [11] D. C. Look, D. C. Reynolds, C. W. Litton, R. L. Jones, D. B. Eason, and G. Cantwell, *Appl. Phys. Lett.* **81**, 1830 (2002).
- [12] H. W. Liang, Y. M. Lu, D. Z. Shen, Y. C. Liu, J. F. Yan, C. X. Shan, B. H. Liu, Z. Z. Zhang, J. Y. Zhang, and X. W. Fan, *Phys. Status Solidi A* **202**, 1060

(2005).

- [13] J. G. Lu, Z. Z. Ye, F. Zhuge, Y. J. Zeng, B. H. Zhao, and L. P. Zhu, *Appl. Phys. Lett.* **85**, 3134 (2004).
- [14] E. Kamińska, A. Piotrowska, J. Kossut, R. Butkutė, W. Dobrowolski, R. Łukasiewicz, A. Barcz, R. Jakiela, E. Dynowska, E. Przeździecka, M. Aleszkiewicz, P. Wojnar, and E. Kowalczyk, *Phys. Status Solidi C* **2**, 1119 (2005).
- [15] X. Li, Y. Yan, T. A. Gessert, C. L. Perkins, D. Young, C. DeHart, M. Young, and T. J. Coutts, *J. Vac. Sci. Technol. A* **21**, 1342 (2003).
- [16] D. K. Hwang, H. S. Kim, J. H. Lim, J. Y. Oh, J. H. Yang, S. J. Park, K. K. Kim, D. C. Look, and Y. S. Park, *Appl. Phys. Lett.* **86**, 151917 (2005).
- [17] V. Vaithianathan, B. T. Lee, and S. S. Kim, *Phys. Status Solidi A* **201**, 2837 (2004).
- [18] K. K. Kim, H. S. Kim, D. K. Hwang, J. H. Lim, and S. J. Park, *Appl. Phys. Lett.* **83**, 63 (2003).
- [19] Z. Q. Chen, A. Kawasuso, Y. Xu, H. Naramoto, X. L. Yuan, T. Sekiguchi, R. Suzuki, and T. Ohdaira, *J. Appl. Phys.* **97**, 013528 (2005).
- [20] Y. R. Ryu, T. S. Lee, and H. W. White, *Appl. Phys. Lett.* **83**, 87 (2003).
- [21] D. C. Look, G. M. Renlund, R. H. Burgener II, and J. R. Sizelove, *Appl. Phys. Lett.* **85**, 5269 (2004).
- [22] V. Vaithianathan, B. T. Lee, and S. S. Kim, *Appl. Phys. Lett.* **86**, 062101(2005).
- [23] T. S. Jeong, M. S. Han, C. J. Youn, and Y. S. Park, *J. Appl. Phys.* **96**, 175 (2004).
- [24] J. G. Lu, Y. Z. Zhang, Z. Z. Ye, L. P. Zhu, L. Wang, and B. H. Zhao, *Appl. Phys. Lett.* **88**, 222114 (2006).
- [25] A. V. Singh, R. M. Mehra, A. Wakahara, and A. Yoshida, *J. Appl. Phys.* **93**, 396

(2003).

- [26] D. C. Park, I. Sakaguchi, N. Ohashi, S. Hishita, and H. Haneda, *Appl. Surf. Sci.* **203/204**, 359 (2003).
- [27] A. Tsukazaki, T. Onuma, M. Ohtani, T. Makino, M. Sumiya, K. Ohtani, S. F. Chichibu, S. Fuke, Y. Segawa, H. Ohno, H. Koinuma, and M. Kawasaki, *Nat. Mater.* **4**, 42 (2005).
- [28] S. J. Jiao, Z. Z. Zhang, Y. M. Lu, D. Z. Shen, B. Yao, J. Y. Zhang, B. H. Li, D. X. Zhao, X. W. Fan, and Z. K. Tang, *Appl. Phys. Lett.* **88**, 031911 (2006).
- [29] W. Liu, S. L. Gu, J. D. Ye, S. M. Zhu, S. M. Liu, X. Zhou, R. Zhang, Y. Hang, and C. L. Zhang, *Appl. Phys. Lett.* **88**, 092101 (2006).
- [30] Y. M. Ye, Z. Z. Ye, L. L. Chen, B. H. Zhao, and L. P. Zhu, *Appl. Surf. Sci.* **253**, 2345 (2006).
- [31] Y. W. Heo, Y. W. Kwon, Y. Li, S. J. Pearton, and D. P. Norton, *Appl. Phys. Lett.* **84**, 3474 (2004).
- [32] P. Wana, N. F. Chen, Z. G. Yin, R. X. D., and Y. M. Bai, *Appl. Phys. Lett.* **89**, 202102 (2004).
- [33] M. X. Qiu, Z. Z. Ye, H. P. He, Y. Z. Zhang, X.Q. Gu, L. P. Zhu, and B. H. Zhao, *Appl. Phys. Lett.* **90**, 182116 (2007).
- [34] J. F. Sarver, F. L. Katnack, and F. A. Hummel, *J. Electrochem. Soc.* **106**, 960 (1959).
- [35] K. Koike, K. Hama, I. Nakashima, G. Takada, K. Ogatha, S. Sasa, M. Inoue, and M. Yano, *J. Cryst. Growth* **278**, 288 (2005).
- [36] S. Choopun, R. D. Vispute, W. Yang, R. P. Sharma, T. Venkatesan, and H. Shen, *Appl. Phys. Lett.* **80**, 1529 (2002).
- [37] J. H. Lim, C. K. Kang, K. K. Kim, I. K. Park, D. K. Hwang, and S. J. Park, *Adv. Mater.* **18**, 2720 (2006).

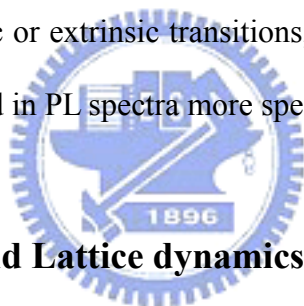
[38] J. Y. Bae, J. Yoo, and G. C. Yi, Appl. Phys. Lett. **89**, 173114 (2006).

[39] H. Shibata, H. Tampo, K. Matsubara, A. Yamada, K. Sakurai, S. Ishizuka, and S. Niki, and M. Sakai, Appl. Phys. Lett. **90**, 124104 (2007).



## Chapter 2 Theoretical background

In this chapter, crystal structures, lattice dynamics, and fundamental optical transitions of ZnO are reviewed. Lattice dynamics corresponding to the selection rules, lattice vibrational properties, and polar-optical phonon scattering mechanism are discussed. Optical transitions in ZnO have been studied by a variety of experimental techniques such as optical absorption, transmission, reflection, photoluminescence (PL), and cathodoluminescence spectroscopies, etc. In Section 2.2, we reviewed some fundamental issues related to the optical properties of ZnO single crystal by PL measurement. After understanding the excitonic fine structures associated with either intrinsic or extrinsic transitions, we would describe the various sharp emission peaks observed in PL spectra more specifically for Chapter 5 and 6.



### 2.1 Crystal structures and Lattice dynamics

#### 2.1.1 Crystal structures [1]

ZnO is a II-VI compound semiconductor whose ionicity resides at the borderline between covalent and ionic semiconductor. The crystal structures shared by ZnO are wurtzite, zinc blende, and rocksalt. At ambient conditions, the thermodynamically stable phase is wurtzite. The wurtzite structure has a hexagonal unit cell with two lattice parameters,  $a$  and  $c$ , and belongs to the space group of  $C_{6v}^4$  or  $P6_{3mc}$ . A schematic representation of the wurtzitic ZnO structure is revealed in Fig. 2-1. The structure is composed of two interpenetrating hexagonal-close-packed (hcp) sublattices, each of which consists of one type of atom displaced with respect to each other along the threefold  $c$ -axis by the amount of  $u$  in fractional coordinates (the  $u$

parameter is defined as the length of the bond parallel to the  $c$  axis, in units of  $c$ ). Each sublattice includes four atoms per unit cell and every atom of one kind (group-II atom) is surrounded by four atoms of the other kind (group VI), or vice versa, which are coordinated at the edges of a tetrahedron. In a real ZnO crystal, the wurtzite structure deviates from the ideal arrangement, by changing the  $c/a$  ratio or the  $u$  value. It should be pointed out that a strong correlation exists between the  $c/a$  ratio and the  $u$  parameter in that when the  $c/a$  ratio decreases, the  $u$  parameter increases in such a way that those four tetrahedral distances remain nearly constant through a distortion of tetrahedral angles due to long-range polar interactions.

The lattice parameters of any crystalline material are commonly and most accurately measured by high resolution x-ray diffraction. Several groups reported the measured and calculated lattice parameters,  $c/a$  ratio, and  $u$  parameter for ZnO crystallized wurtzite structures. The lattice constants mostly range from 3.2475 to 3.2501 Å for the  $a$  parameter and from 5.2042 to 5.2075 Å for the  $c$  parameter. The  $c/a$  ratio and  $u$  parameter vary in a slightly wider range, from 1.593 to 1.6035 and from 0.383 to 0.3856, respectively. The deviation from that of the ideal wurtzite crystal is probably due to lattice stability and ionicity. It has been reported that free charge is the dominant factor responsible for expanding the lattice proportional to the deformation potential of the conduction-band minimum and inversely proportional to the carrier density and bulk modulus. The point defects such as zinc antisites, oxygen vacancies, and extended defects, such as threading dislocations, also increase the lattice constant, albeit to a lesser extent in the heteroepitaxial layers.

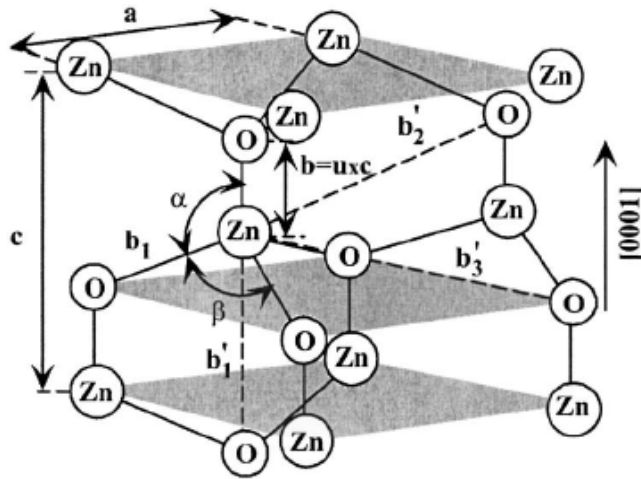


Fig. 2-1 Schematic representation of a wurtzite ZnO structure having lattice constants  $a$  and  $c$ ;  $u$  is the bond length, and  $\alpha$  and  $\beta$  are the bond angles. [1]

### 2.1.2 Selection rules and phonon modes [2,3]

When photons from a laser are scattered from a crystal with emission or absorption of phonons, the energy shifts of the photons are small, but can be measured by interferometric techniques. Usually, the phonon wave vectors are very small compared to the size of the Brillouin zone so that the interactions are only with zone center phonon. Thus, one can have interaction with either the zone center acoustic phonons or the optical phonons. The interaction with acoustic phonons is called Brillouin scattering while the interaction with optical phonons is called Raman scattering. All of the Raman mode frequencies, intensities, line-shapes, and line-widths, as well as polarizations can be used to characterize the lattices and impurities. The intensity gives information on crystallinity. The line-width increases when a material is damaged or disordered, because damage or disorder occurs in a material will increase phonon damping rate or relax the rules for momentum conservation in Raman process.

The different long-wavelength phonon branches in a given crystal correspond to

different symmetries of vibration of the atoms in the unit cell and are characterized by irreducible representations of the space group of the crystal lattice. If the wavelengths of the Raman phonons are assumed to be effectively infinite, then the crystal point group can be used in classifying the phonon symmetries. This infinite wavelength assumption is not valid for Raman-active phonons which are also infrared active, and this type of vibration will be discussed separately in the following section.

The selection rules for Raman-active phonons can be determined by standard group-theoretical methods and the calculation is described in some detail by Heine, who based his work on the polarizability derivative theory of Born and Bradburn. The result of this approach is that a phonon can participate in a first-order Raman transition if and only if its irreducible representation is the same as one of the irreducible representations which occur in the reduction of the representation of the polarizability tensor. The irreducible representations by which the components of the polarizability tensor transform are conveniently listed by Herzberg and Wilson *et al.* for the set of molecular point groups, which includes the 32 crystal point groups.

The intensity of the Raman-scattered radiation depends in general on the directions of observation and illumination relative to the principal axes of the crystal. The angular variation of the scattering gives information about the symmetry of the lattice vibration responsible. The anisotropy of the scattering can be predicted for a vibration of any given symmetry by standard group-theoretical methods.

GaN-, AlN- and InN-based materials are highly stable in the hexagonal wurtzite structure although they can be grown in the zinc blende phase and unintentional phase separation and coexistence may occur. The wurtzite crystal structure belongs to the space group  $C_{6v}^4$  and group theory predicts zone-center optical modes are  $A_1$ ,  $2B_1$ ,  $E_1$  and  $2E_2$ . The  $A_1$  and  $E_1$  modes and the two  $E_2$  modes are Raman active while the  $B$



modes are silent. The  $A$  and  $E$  modes are polar, resulting in a splitting of the LO and the transverse (TO) modes. The Raman tensors for the wurtzite structure are as follows:

$$\begin{aligned}
 & \begin{pmatrix} a & 0 & 0 \\ 0 & a & 0 \\ 0 & 0 & b \end{pmatrix} & A_1(z) \text{ mode} \\
 & \begin{pmatrix} 0 & 0 & c \\ 0 & 0 & 0 \\ c & 0 & 0 \end{pmatrix} & E_1(x) \text{ mode} \\
 & \begin{pmatrix} 0 & 0 & 0 \\ 0 & 0 & c \\ 0 & c & 0 \end{pmatrix} & E_1(y) \text{ mode} \\
 & \begin{pmatrix} f & 0 & 0 \\ 0 & -f & 0 \\ 0 & 0 & 0 \end{pmatrix} \begin{pmatrix} 0 & -f & 0 \\ -f & 0 & 0 \\ 0 & 0 & 0 \end{pmatrix} & E_2 \text{ mode.}
 \end{aligned} \tag{2.1}$$

Here  $x, y$  or  $z$  in brackets after an irreducible representation indicates that the vibration is also infra-red active and has the direction of polarization indicated. Such vibrations occur only in piezo-electric crystals (i.e. crystals with no center of inversion symmetry). In crystals which do have a center of inversion symmetry, only even-parity vibrations, whose representations have a subscript  $g$ , can be Raman active and only odd-parity (subscript  $u$ ) vibrations can be infrared active. This fact leads to the important complementary nature of infra-red absorption and Raman effect measurements. Directly above each irreducible representation is a matrix which gives the non-vanishing components of the Raman tensor, i.e. of  $\alpha_{\rho\sigma,\mu}$  or  $R_{\sigma\rho}^{\mu}$ . The different elements of the matrices are the nine components of the tensor obtained by allowing both  $\rho$  and  $\sigma$  to take on the values  $x, y$  and  $z$ . Here  $x, y$ , and  $z$  are the crystal principal axes chosen to be identical with the principal axes  $x_1, x_2$  and  $x_3$  defined for all the crystal classes by Nye. The component  $\mu$  of the phonon polarization for the

case of infrared-active vibrations is the quantity given in brackets after the irreducible representation symbol.

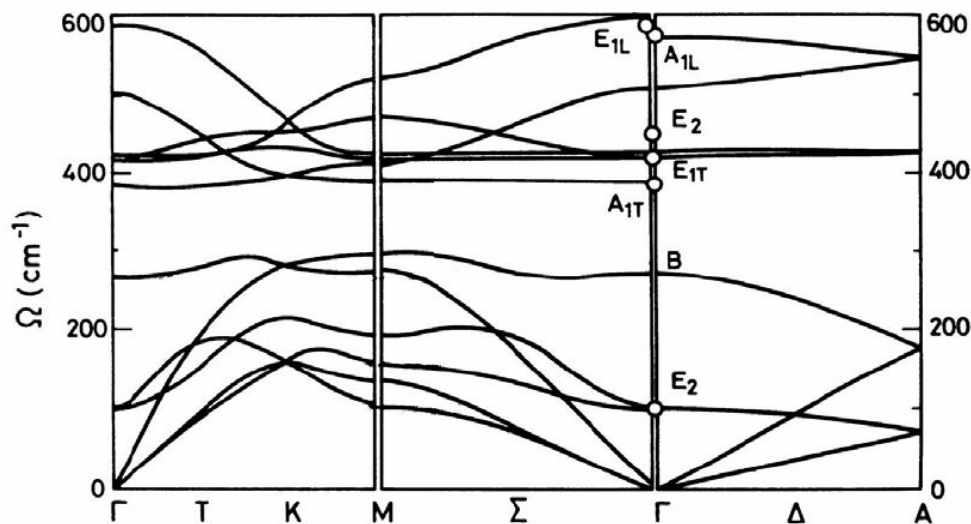


Fig. 2-2 Phonon dispersion curves for ZnO crystal of wurtzite structure. (after Calleja *et al.* [4])

The vibrational modes in ZnO wurtzite structures are given in Figure 2-2. At the  $\Gamma$  point of the Brillouin zone, it can be seen that the existence of the following optic phonon modes:  $A_1+2B_1+E_1+2E_2$ ;  $A_1$  and  $E_1$  modes are both Raman and infrared active; and  $B_1(\text{low})$  and  $B_1(\text{high})$  modes are silent. However, the nonpolar  $E_2$  modes are Raman active and have two frequencies:  $E_2(\text{high})$  is related to the vibration of oxygen atoms and  $E_2(\text{low})$  is associated with the Zn sublattice. The displacement vectors of the phonon normal modes are illustrated in Fig. 2-3. For the lattice vibrations with  $A_1$  and  $E_1$  symmetry, the atoms move parallel and perpendicular to the  $c$ -axis, respectively. Table 2-1 summarizes a list of observed zone-center optical-phonon wave numbers along with those calculated for wurtzite ZnO.

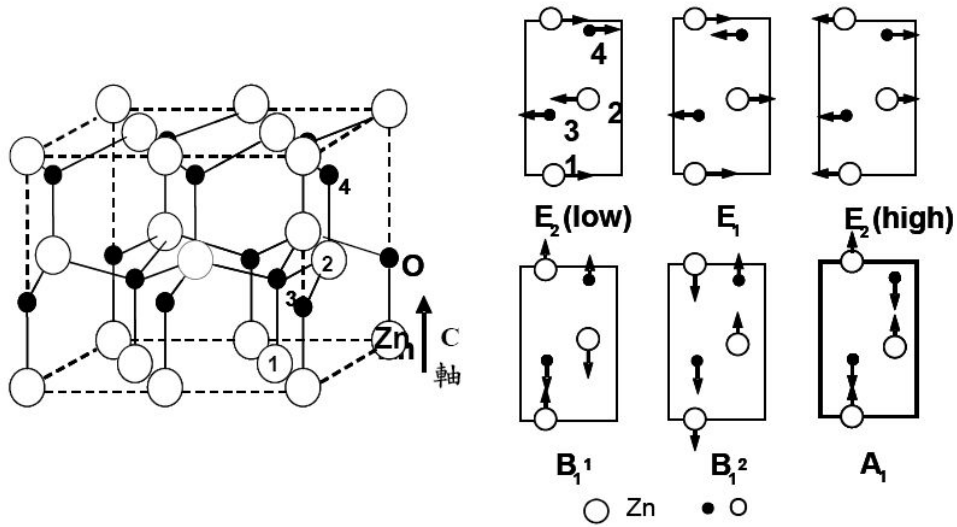


Fig. 2-3 Displacement vectors of the phonon modes in ZnO wurtzite structure. (after Jephcoat *et al.* [5])

Table 2-1 Phonon mode frequencies of wurtzite ZnO at the center of the Brillouin zone obtained from infrared spectroscopic ellipsometry and Raman scattering measurements in comparison with theoretical predictions. [1]

Symmetry	Raman spectroscopy	Infrared spectroscopy	Theor. calc.
$A_1$ -TO	380(2), <sup>a</sup> 379(2), <sup>b</sup> 380, <sup>c</sup> 380, <sup>d</sup> 378, <sup>e</sup> 380 <sup>f</sup>	380 <sup>g</sup>	382, <sup>h</sup> 386 <sup>i</sup>
$E_1$ -TO	409(2), <sup>a</sup> 410(2), <sup>b</sup> 407, <sup>c</sup> 413, <sup>d</sup> 409.5 <sup>e</sup>	409.1(0.9), <sup>a</sup> 408.2(0.3), <sup>b</sup> 412 <sup>g</sup>	316, <sup>h</sup> 407 <sup>i</sup>
$A_1$ -LO	574, <sup>d</sup> 576, <sup>c</sup> 579, <sup>d</sup> 579 <sup>f</sup>	574.5(0.3), <sup>a</sup> 577.1(0.4), <sup>b</sup> 570 <sup>g</sup>	548 <sup>h</sup>
$E_1$ -LO	587(2), <sup>a</sup> 591(2), <sup>b</sup> 583, <sup>c</sup> 588, <sup>c</sup> 591 <sup>d</sup>	588.3(0.7), <sup>a</sup> 592.1(0.2), <sup>b</sup> 591 <sup>g</sup>	628 <sup>h</sup>
$E_2$ -low	102(1), <sup>a</sup> 102(1), <sup>b</sup> 101, <sup>c</sup> 101, <sup>d</sup> 98, <sup>c</sup> 99 <sup>f</sup>		126, <sup>h</sup> 98 <sup>i</sup>
$E_2$ -high	438(1), <sup>a</sup> 437(1), <sup>b</sup> 437, <sup>c</sup> 444, <sup>d</sup> 437.5, <sup>e</sup> 438 <sup>f</sup>		335, <sup>h</sup> 433 <sup>i</sup>
$B_1$ -low			240
$B_2$ -high			540

### 2.1.3 Polar-optical phonons: Fröhlich interaction [3]

One of the most important carrier-phonon scattering mechanisms in semiconductors occurs when charge carriers interact with the electric polarization,  $\mathbf{P}(\mathbf{r})$ , produced by the relative displacement of positive and negative ions. In low-defect polar semiconductors such as GaAs, InP, and GaN, carrier scattering in polar semiconductors at RT is dominated by this polar-optical-phonon (POP) scattering mechanism. The POP-carrier interaction is referred to as the Fröhlich interaction. Here, the potential energy associated with the Fröhlich interaction will be denoted by  $\phi_{\text{Fr}}(\mathbf{r})$ . The polarization  $\mathbf{P}$  associated with polar-optical phonons and the potential energy associated with the Fröhlich interaction,  $\phi_{\text{Fr}}(\mathbf{r})$ , are related by

$$\nabla^2 \phi_{\text{Fr}}(\mathbf{r}) = 4\pi e \nabla \cdot \mathbf{P}(\mathbf{r}). \quad (2.2)$$

In terms of the phonon creation and annihilation operators ( $a_q^+$  and  $a_q$  respectively), the operators act on states each having a given number of phonons. The creation operator acting on a state of  $n_q$  phonons of wavevector  $q$  increases the number of phonons to  $n_q + 1$  and the phonon annihilation operator acting on a state of  $n_q$  phonons of wavevector  $q$  decreases the number of phonons to  $n_q - 1$ . In phonon absorption processes the phonon appears as an incoming wave and the factor  $e^{i(\mathbf{q}\cdot\mathbf{r}-\omega t)}$  multiplies the amplitudes associated with the phonon fields. Likewise, in phonon emission processes the phonon appears as an outgoing wave and the factor  $e^{i(-\mathbf{q}\cdot\mathbf{r}-\omega t)}$  multiplies the amplitudes associated with the phonon fields. Moreover, each incoming or outgoing phonon will be associated with a unit polarization vector; these unit polarization vectors will be denoted by  $\hat{\mathbf{e}}_{\mathbf{q},j}$  for incoming waves and by  $\hat{\mathbf{e}}_{\mathbf{q},j}^*$  for outgoing waves.  $\mathbf{P}(\mathbf{r})$  may be written as

$$\mathbf{P}(\mathbf{r}) = \zeta \sum_{j=1,2,3} \int \frac{d^3 \mathbf{q}}{(2\pi)^3} (a_{\mathbf{q}} e^{i\mathbf{q}\cdot\mathbf{r}} \mathbf{e}_{\mathbf{q},j} + a_{\mathbf{q}}^+ e^{-i\mathbf{q}\cdot\mathbf{r}} \mathbf{e}_{\mathbf{q},j}^*) \quad (2.3)$$

where  $\mathbf{e}_{\mathbf{q},j}$  represents the polarization vector associated with  $\mathbf{P}(\mathbf{r})$ ,  $\mathbf{q}$  is the phonon wavevector and  $\zeta$  is the coupling constant; then, it follows that

$$4\pi \nabla \cdot \mathbf{P}(\mathbf{r}) = 4\pi i \zeta \sum_{j=1,2,3} \int \frac{d^3 \mathbf{q}}{(2\pi)^3} (a_{\mathbf{q}} e^{i\mathbf{q}\cdot\mathbf{r}} \mathbf{q} \cdot \mathbf{e}_{\mathbf{q},j} - a_{\mathbf{q}}^+ e^{-i\mathbf{q}\cdot\mathbf{r}} \mathbf{q} \cdot \mathbf{e}_{\mathbf{q},j}^*). \quad (2.4)$$

Consider the case of a polar crystal with two atoms per unit cell, such as GaAs. The dominant contribution to  $\mathbf{P}(\mathbf{r})$  results from the phonon modes in which the normal distance between the planes of positive and negative charge varies. Such modes are obviously the longitudinal optical (LO) modes since in the case of LO modes  $\mathbf{e}_{\mathbf{q},j}$  is parallel to  $\mathbf{q}$ . However, transverse optical (TO) phonons produce displacements of the planes of charge such that they remain at fixed distances from each other; that is, the charge planes slide by each other but the normal distance between planes of opposite charge does not change. So, TO modes make negligible contributions to  $\mathbf{P}(\mathbf{r})$ . For TO phonons,  $\mathbf{e}_{\mathbf{q},j} \cdot \mathbf{q} = 0$ . Accordingly,

$$4\pi \nabla \cdot \mathbf{P}(\mathbf{r}) = 4\pi i \zeta \int \frac{d^3 \mathbf{q}}{(2\pi)^3} (a_{\mathbf{q}} e^{i\mathbf{q}\cdot\mathbf{r}} q - a_{\mathbf{q}}^+ e^{-i\mathbf{q}\cdot\mathbf{r}} q), \quad (2.5)$$

and the potential energy associated with the Fröhlich interaction,  $\phi_{\text{Fr}}(\mathbf{r})$ , is given by

$$H_{\text{Fr}} = \phi_{\text{Fr}}(\mathbf{r}) = -4\pi i e \zeta \int \frac{d^3 \mathbf{q}}{(2\pi)^3} \frac{1}{q} (a_{\mathbf{q}} e^{i\mathbf{q}\cdot\mathbf{r}} - a_{\mathbf{q}}^+ e^{-i\mathbf{q}\cdot\mathbf{r}}), \quad (2.6)$$

where  $\phi_{\text{Fr}}(\mathbf{r})$ , has been denoted by  $H_{\text{Fr}}$ , the Fröhlich interaction Hamiltonian since  $\phi_{\text{Fr}}(\mathbf{r})$  is the only term contributes to it. The dependence of  $\phi_{\text{Fr}}(\mathbf{r})$  on  $q^{-1}$  is familiar from the Coulomb interaction; the coupling constant  $\zeta$  remains to be determined.

In polar semiconductors, the electron and nucleus having masses  $m$  and  $M$  carry opposite effective charges,  $e^*$ , as a result of the redistribution of the charge associated with polar bonding. The electric polarization  $\mathbf{P}(\mathbf{r})$  may be written as

$$\begin{aligned}
\mathbf{P}(\mathbf{r}) &= \frac{Ne^*}{\varepsilon(\infty)} \mathbf{u}_q(\mathbf{r}) \\
&= \frac{Ne^*}{\varepsilon(\infty)} \frac{1}{\sqrt{N}} \sum_q \sum_{j=1,2,3} \sqrt{\frac{\hbar}{2\left(\frac{mM}{m+M}\right)\omega_{LO}}} \times (a_q e^{i\mathbf{q}\cdot\mathbf{r}} \mathbf{e}_{\mathbf{q},j} - a_q^+ e^{-i\mathbf{q}\cdot\mathbf{r}} \mathbf{e}_{\mathbf{q},j}^*), \tag{2.7}
\end{aligned}$$

where the division by  $\varepsilon(\infty)$  accounts for screening,  $\mathbf{u}(\mathbf{r})$  is the normal-mode phonon displacement,  $q$  is summed over all wavevectors in the Brillouin zone, and  $N$  is the number of unit cells in the sample.

The normal-mode phonon displacement  $u_q$  can be expressed in terms of  $a_q^+$  and  $a_q$

$$u_q = \sqrt{\frac{\hbar}{2m\omega_q}} (a_q + a_q^+). \tag{2.8}$$

$\mathbf{u}(\mathbf{r})$  is a Fourier series over the modes  $u_q$ . As a means of including the phase factors to ensure proper accounting of energy and momentum as well as the appropriate unit polarization vectors, (2.8) will be written as a sum over all wavevectors  $q$ ; the appropriate non-temporal phase factors appear as multipliers of the corresponding phonon operators:

$$\begin{aligned}
\mathbf{u}(\mathbf{r}) &= \frac{1}{\sqrt{N}} \sum_q \sum_{j=1,2,3} \sqrt{\frac{\hbar}{2m\omega_q}} (a_q e^{i\mathbf{q}\cdot\mathbf{r}} \hat{\mathbf{e}}_{\mathbf{q},j} + a_q^+ e^{-i\mathbf{q}\cdot\mathbf{r}} \hat{\mathbf{e}}_{\mathbf{q},j}^*) \\
&= \frac{1}{\sqrt{N}} \sum_q \sum_{j=1,2,3} \sqrt{\frac{\hbar}{2m\omega_q}} \hat{\mathbf{e}}_{\mathbf{q},j} (a_q + a_{-q}^+) e^{i\mathbf{q}\cdot\mathbf{r}} \equiv \sum_q \mathbf{u}(\mathbf{q}) e^{i\mathbf{q}\cdot\mathbf{r}}. \tag{2.9}
\end{aligned}$$

By noticing that

$$\frac{1}{\sqrt{V}} \sum_q \leftrightarrow \int \frac{d^3\mathbf{q}}{(2\pi)^3} \tag{2.10}$$

and by comparing expressions (2.3) and (2.7), it follows that

$$\zeta = \frac{Ne^*}{\varepsilon(\infty)} \frac{1}{\sqrt{N}} \sqrt{\frac{\hbar}{2\left(\frac{mM}{m+M}\right)\omega_{LO}}}. \tag{2.11}$$

However, from the dielectric constant due to the electronic response

$$\varepsilon(\omega) = \varepsilon(\infty) + \frac{4\pi}{(\omega_{\text{TO}}^2 - \omega^2)} \frac{Ne^{*2}}{\varepsilon(\infty)} \left( \frac{1}{m} + \frac{1}{M} \right) \text{ evaluated for } \omega = \omega_{\text{LO}} \text{ where } \varepsilon(\omega_{\text{LO}}) = 0, \text{ it}$$

follows that

$$\begin{aligned} \frac{Ne^{*2}}{\varepsilon(\infty)^2} \left( \frac{1}{m} + \frac{1}{M} \right) &= \frac{\omega_{\text{LO}}^2 - \omega_{\text{TO}}^2}{4\pi\varepsilon(\infty)} \\ &= \frac{\omega_{\text{LO}}^2}{4\pi} \left[ \frac{1}{\varepsilon(\infty)} - \frac{1}{\varepsilon(\infty)} \frac{\omega_{\text{TO}}^2}{\omega_{\text{LO}}^2} \right] \\ &= \frac{\omega_{\text{LO}}^2}{4\pi} \left[ \frac{1}{\varepsilon(\infty)} - \frac{1}{\varepsilon(0)} \right], \end{aligned} \quad (2.12)$$

so that

$$\zeta = \frac{Ne^*}{\varepsilon(\infty)} \frac{1}{\sqrt{N}} \sqrt{\frac{\hbar}{2\left(\frac{mM}{m+M}\right)\omega_{\text{LO}}}} = \sqrt{\frac{\hbar}{2\omega_{\text{LO}}} \frac{\omega_{\text{LO}}^2}{4\pi} \left[ \frac{1}{\varepsilon(\infty)} - \frac{1}{\varepsilon(0)} \right]}, \quad (2.13)$$

and

$$\begin{aligned} H_{\text{Fr}} = \phi_{\text{Fr}}(\mathbf{r}) &= -4\pi i e \zeta \int \frac{d^3\mathbf{q}}{(2\pi)^3} \frac{1}{q} (a_{\mathbf{q}} e^{i\mathbf{q}\cdot\mathbf{r}} - a_{\mathbf{q}}^+ e^{-i\mathbf{q}\cdot\mathbf{r}}) \\ &= -i \sqrt{\frac{2\pi e^2 \hbar \omega_{\text{LO}}}{V} \left[ \frac{1}{\varepsilon(\infty)} - \frac{1}{\varepsilon(0)} \right]} \sum_{\mathbf{q}} \frac{1}{q} (a_{\mathbf{q}} e^{i\mathbf{q}\cdot\mathbf{r}} - a_{\mathbf{q}}^+ e^{-i\mathbf{q}\cdot\mathbf{r}}). \end{aligned} \quad (2.14)$$

Besides, the lattice distortion created by a phonon resulting in a local change in the crystal's energy band; the energy associated with the change is known as the deformation potential and it represents one of the major scattering mechanisms in non-polar semiconductors. Indeed, the deformation-potential interaction is a dominant source of electron energy loss in silicon-based electronic devices. The piezoelectric interaction occurs in all polar crystals lacking an inversion symmetry. In the general case, the application of an external strain to a piezoelectric crystal will produce a macroscopic polarization as a result of the displacements of ions. Thus an acoustic phonon mode will drive a macroscopic polarization in a piezoelectric crystal.

## 2.2 Fundamental optical transitions

In this section, a review on the intrinsic excitonic properties, donor- and acceptor-bound excitons, two-electron satellites, and longitudinal optical (LO)-phonon replicas investigated by low temperature PL spectrum is given. Then, the donor-acceptor-pair (DAP) transition, green, yellow, and orange defect emissions are discussed. Finally, biexciton and exciton-exciton scattering are explored.

### 2.2.1 General conceptions [6,7]

The ground state of the electronic system of a perfect semiconductor is a completely filled valance band and a completely empty conduction band. We can define this state as the “zero” energy or “vacuum” state. If we start from the ground state and excite one electron to the conduction band, we simultaneously create a hole in the valance band. In this sense an optical excitation is a two-particle transition. The same is true for the recombination process. An electron in the conduction band can return radiatively or nonradiatively into the valance band only if there is a free space, i.e., a hole. Two quasi-particles, an electron and a hole, are annihilated in the recombination process. What we need for the understanding of the optical properties of the electronic system of a semiconductor is therefore a description of the excited states of the N-particle problem. The quanta of these excitations are called excitons, which have been classified as Wannier exciton and Frenkel exciton. It should be mentioned that in insulators like NaCl, or in organic crystals like anthracene, excitons also exist with electron-hole pair wavefunctions confined to one unit cell. These so-called Frenkel excitons cannot be described in the effective mass approximation. In Wannier excitons, the Bohr radius (i.e. the mean distance between electron and hole) is larger compared to the lattice constant. This situation is well realized in



narrow-gap semiconductors which usually have large  $\epsilon$  ( $\gg 1$ ) and small  $\mu$  ( $\ll m_0$ ). Therefore, we always deal with Wannier excitons in all semiconductors, inclusive of ZnO certainly. Here we will consider the Wannier excitons more specifically.

Using the effective mass approximation, the Coulomb interaction between electron and hole leads to a hydrogen-like problem with a Coulomb potential term  $\frac{-e^2}{4\pi\epsilon_0\epsilon|r_e - r_h|}$ . Excitons in semiconductors form, to a good approximation, a hydrogen or positronium like series of states below the gap. For a simple parabolic band in a direct-gap semiconductor one can separate the relative motion of electron and hole and the motion of the center of mass. This leads to the dispersion relation of exciton as shown in Fig. 2-4

$$E_{\text{ex}}(n_B, \mathbf{K}) = E_g - Ry^* \frac{1}{n_B^2} + \frac{\hbar^2 \mathbf{K}^2}{2M}, \quad (2.15)$$

where  $n_B = 1, 2, 3, \dots$  is the principal quantum number,  $Ry^* = 13.6\text{eV} \frac{\mu}{m_0} \frac{1}{\epsilon^2}$  is the exciton binding energy,  $M = m_e + m_h$ , and  $\mathbf{K} = \mathbf{k}_e + \mathbf{k}_h$  are the translational mass and wave vector of the exciton, respectively. The series of exciton states in (2.15) has an effective Rydberg energy  $Ry^*$  modified by the reduced mass of electron and hole and the dielectric constant of the medium in which these particles move. The radius of the exciton equals the Bohr radius of the H atom again modified by  $\epsilon$  and  $\mu$ . Using the material parameters for typical semiconductors one finds that the orbits of electron and hole around their common center of mass average over many unit cells and this in turn justifies the effective mass approximation in a self-consistent way. These excitons are called Wannier excitons. The exciton Bohr radius of bulk ZnO is 2.34 nm. Based on cyclotron resonance measured polaronic mass as  $0.28m_0$  [8] for  $\mathbf{H} \parallel \mathbf{c}$  corresponding to the bare mass of  $0.24m_0$ , which is consistent with Faraday

rotation measurement by Mollwo *et al.* [9], in the strong confinement regime, Senger *et al.* [10] demonstrated exciton radius in ZnO quantum dots changed dramatically as the crystal size closes to 2.34 nm to determine the Bohr radius of bulk exciton as 2.34 nm. Independently, we also found dramatic band-gap enlargement when the size approaches 2.34 nm.[11] This value is now commonly used in literatures.[12,13]

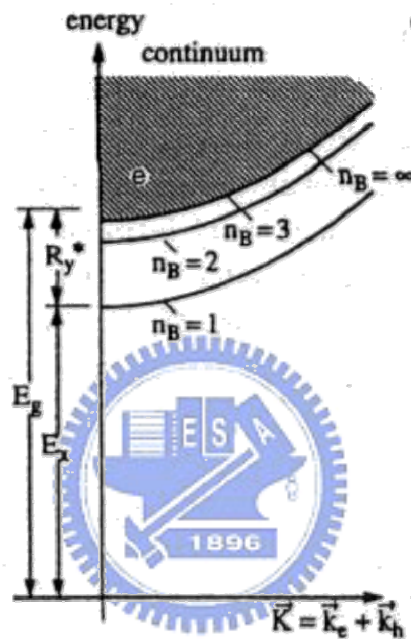


Fig. 2-4 A pair excitation in the scheme of valence and conduction band in the exciton picture for a direct gap semiconductor. [6]

## 2.2.2 Exciton-related emission

Exciton photoluminescence (PL) is very sensitive to the quality of crystal structures and to the presence of defects. Therefore, the regularities of the change in exciton spectra as a function of composition and structural peculiarities enable one to use them to determine the quality of the crystal optically. Impurities and their associations, main lattice defects and their impurity associations, and exciton and exciton impurity complexes all play an important role in the luminescence, which significantly complicates the observation of free-exciton PL. Generally, PL

spectrum of single crystal ZnO consists mainly of two bands. The one in UV region corresponds to near-band-edge (NBE) emission is attributed to exciton states; the other one in visible region is due to structural defects and impurities.

### 2.2.2.1 Free excitons and polaritons [7,14]

The optical properties of a semiconductor are connected with both intrinsic and extrinsic effects. For a start, the intrinsic excitonic features in the 3.376–3.450 eV range are discussed. The wurtzite ZnO conduction band is mainly constructed from the *s*-like state having ( $\Gamma_7^c$ ) symmetry, whereas the valence band is a *p*-like state, which is split into three bands due to the influence of crystal field and spin-orbit interactions. The ordering of the crystal-field and spin-orbit coupling split states of the valence-band maximum in wurtzite ZnO was calculated by our group using tight-binding theory. The obtained electronic band structure of wurtzite ZnO is shown in Fig. 2-5. The valence-band symmetry ordering (A- $\Gamma_9$ , B- $\Gamma_7$ , and C- $\Gamma_7$ ) in ZnO is the same as that observed in low temperature PL and magnetoluminescence measurements by other researchers.[15-17]

Group theoretical arguments and the direct product of the group representations of the band symmetries ( $\Gamma_7$  for the conduction band,  $\Gamma_9$  for the A valence band, upper  $\Gamma_7$  for the B valence band, and lower  $\Gamma_7$  for the C valence band) will result in the following intrinsic exciton ground state symmetries:

$$\Gamma_7 \times \Gamma_9 \rightarrow \Gamma_5 + \Gamma_6, \quad \Gamma_7 \times \Gamma_7 \rightarrow \Gamma_5 + \Gamma_1 + \Gamma_2$$

The  $\Gamma_5$  and  $\Gamma_6$  exciton ground states are both doubly degenerate, whereas  $\Gamma_1$  and  $\Gamma_2$  are both singly degenerate.  $\Gamma_5$  and  $\Gamma_1$  are allowed transitions with  $\mathbf{E} \perp \mathbf{c}$  and  $\mathbf{E} \parallel \mathbf{c}$ , respectively, but the  $\Gamma_6$  and  $\Gamma_2$  are forbidden.

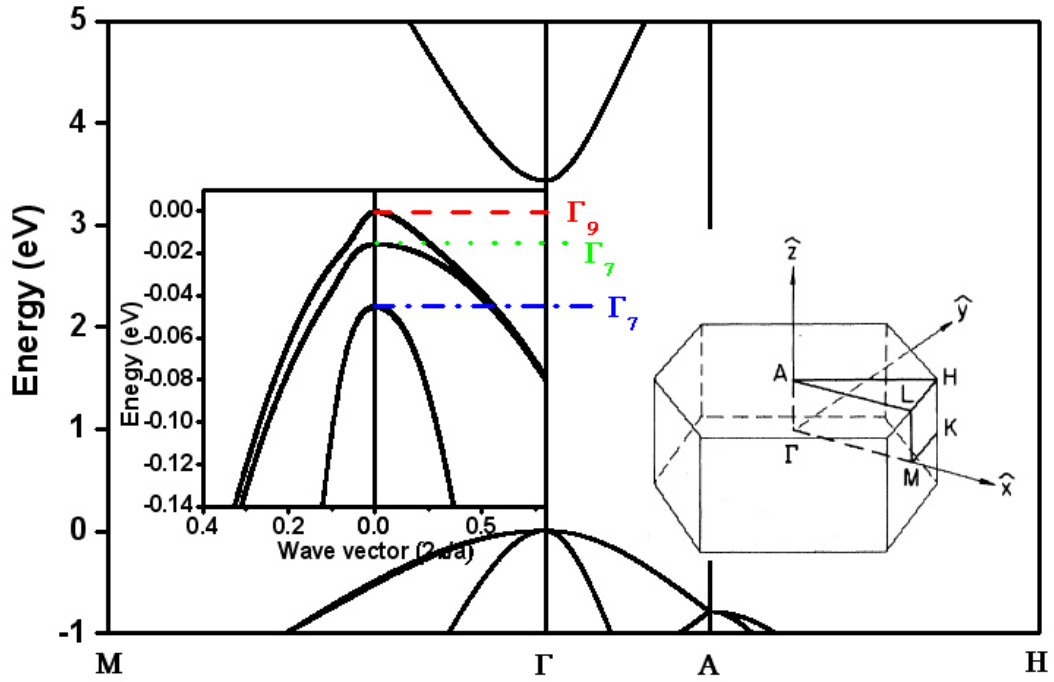


Fig. 2-5 The electronic band structure of wurtzite ZnO. [unpublished]

Figure 2-6 displays the PL spectrum in the range of fundamental excitonic region measured at 10 K in the  $\mathbf{E} \perp \mathbf{c}$  polarization geometry for a high quality ZnO crystal. The A-free exciton and its first excited state emission are observed at  $FX_A^{n=1} = 3.3771$  eV ( $3.3757$  eV for  $\Gamma_6$ ) and  $FX_A^{n=2} = 3.4220$  eV for  $\Gamma_5$  ( $3.4202$  eV for  $\Gamma_6$ ) band symmetry, respectively. Although, at  $k = 0$ ,  $\Gamma_6$  exciton is forbidden in the current measurement mode of polarization, it is still observable, due to the fact that the photon has finite momentum. Geometrical effects such as not having the sample orientation exactly perpendicular to the electric field may be also a reason for observing  $\Gamma_6$  transition. Using the energy separation of ground state and excited state peak positions, the exciton binding energy and band gap energy can be predicted. The energy difference of about 45 meV gives an A-free exciton binding energy of 60 meV and a corresponding band gap energy of 3.4371 eV at 10 K. Based on the reported energy separation of the A- and B-free excitons (in the range of 9–15 meV),

we assigned the weak emission centered at 3.3898 eV, which is about 12.7 meV apart from the A exciton, to the B exciton transition.

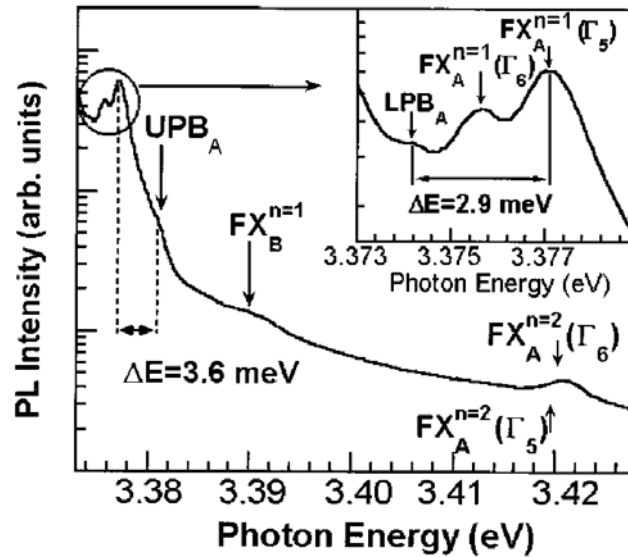


Fig. 2-6 Free excitonic fine structure region of the 10 K PL spectrum for the ZnO single crystal. [14]

Additional fine structure of exciton lines was also observed in low temperature PL spectra. In strongly polar materials like ZnO transverse  $\Gamma_5$  excitons couple with photons to form polaritons. Therefore, as indicated in Fig. 2-6, the  $FX_A^{n=1}(\Gamma_5)$  exciton line has two components. The higher energy component at 3.3810 eV, which is 3.6 meV apart from the A exciton, can be assigned to the so-called longitudinal exciton (upper polariton branch— $UPB_A$ ). The lower energy component at 3.3742 eV, which is about 2.9 meV apart from the A exciton, corresponds to the recombination from the “bottleneck” region, in which the photon and free-exciton dispersion curves cross (lower polariton branch— $LPB_A$ ). As a result, their dispersion curves are illustrated in Figure 2-7, and we will explain the energy diagram of a system consisting of a crystal and radiation below. Since  $\Gamma_6$

excitons do not have transverse character, they do not interact with light to form polaritons, and thus have only normal free-exciton dispersion curves as seen in the PL spectra.

The incident radiation in the exciton band region is converted to the exciton polariton inside the crystal and it has two modes, the upper and lower branches. The energy of the polariton is shown in Fig. 2-7 as a function of wave vector  $k$ . The broken line represents the relation between the energy and wave vector of the photon in vacuum. The absorption of a photon creates an upper-branch polariton at  $a$ , which is then scattered to state  $b$  of the lower-branch polariton. The polariton thus formed is thermalized from  $b$  to  $c$  through phonon and point-defect scattering. The thermalized polariton can be annihilated as a photon at  $d$  (direct radiative annihilation) or move in the crystal to be ionized or annihilated nonradiatively at imperfections, since the thermalized state has a longer lifetime. If the incident radiation energy is below the bottom of the upper-branch polariton, it generates the lower polariton directly.

Here two assumptions are necessary. First, most inelastic scattering is caused by the LO phonon. Second, the probability for a thermalized exciton to be ionized or annihilated at imperfections is larger than that for it to be annihilated as a photon at  $d$  after being scattered from  $b$  to  $c$ . Under these assumptions if the energy difference between the upper polariton state  $a$  and the lower polariton state  $d$  is an integral multiple of the LO phonon energy, the cascade scattering of the polariton into state  $d$  occurs very efficiently and it is annihilated as a photon. If this energy difference is not an integral multiple of the phonon energy, the polariton is scattered and thermalized in the state near  $c$  in the lower-branch polariton and then it is ionized or trapped at imperfections before reaching state  $d$ . Thus the LO phonon structure is

expected in the excitation spectrum of the free-exciton emission.

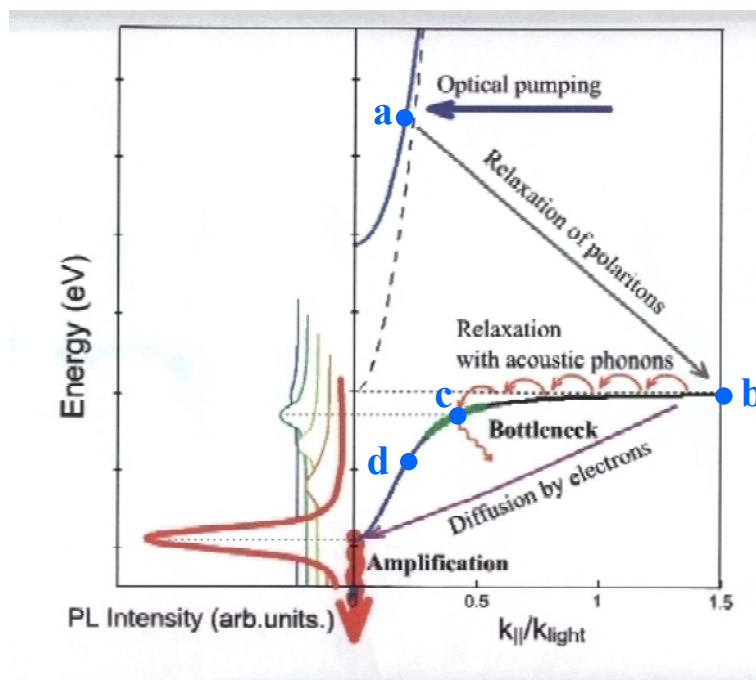


Fig. 2-7 Dispersion curves of exciton and exciton polaritons.

### 2.2.2.2 Bound excitons [14]

Secondly, the spectral region corresponding to the donor and acceptor bound excitons is analyzed. Extrinsic properties are related to dopants or defects, which usually create discrete electronic states in the band gap, and therefore influence both optical absorption and emission processes. In theory, excitons could be bound to neutral or charged donors and acceptors. A basic assumption in the description of the bound exciton states for neutral donors and acceptors is a dominant coupling of the like particles in the bound exciton states. These two classes of bound excitons are by far the most important cases for direct band gap materials. In high quality bulk ZnO, the neutral shallow donor-bound exciton (DBE) often dominates because of the presence of donors due to unintentional impurities and/or shallow donor-like

defects. In samples containing acceptors, the acceptor-bound exciton (ABE) is observed. The recombination of bound excitons typically gives rise to sharp lines with a photon energy characteristic to each defect.

The low-temperature PL spectra are dominated by several bound excitons in the range from 3.348 to 3.374 eV for bulk ZnO sample, as seen in Fig. 2-8. The prominent lines are the A excitons bound to neutral donors that are positioned at 3.3598 ( $D^0_1X_A$ ), 3.3605 ( $D^0_2X_A$ ), 3.3618 ( $D^0_3X_A$ ), 3.3650 ( $D^0_4X_A$ ), and 3.3664 ( $D^0_5X_A$ ) eV. Based on the energy separation between the  $FX_A^{n=1}(\Gamma_5)$  and the DBE peaks, we concluded that the binding energies of the DBEs related to the different donors range from 10 to 20 meV.

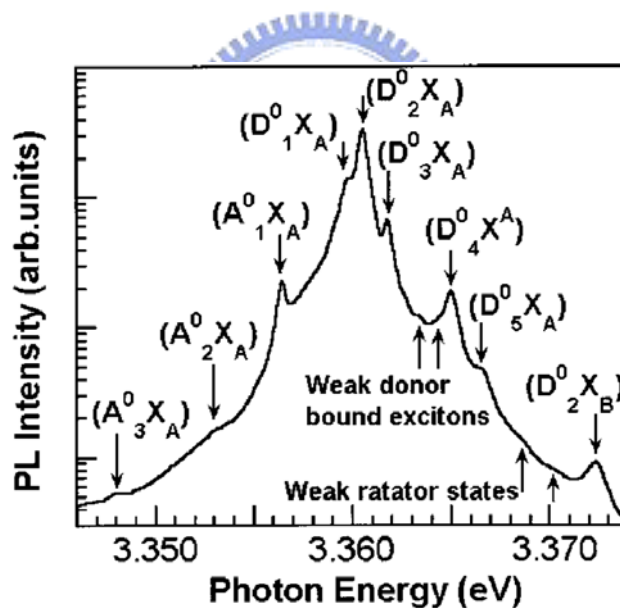


Fig. 2-8 Bound excitonic region of the 10 K PL spectrum for the ZnO single crystal. [14]

On the high-energy side of the neutral DBE, transitions between 3.3664 and 3.3724 eV have been attributed to the excited states or excited rotator states of the neutral-donor-bound excitons. These excited states are analogous to the rotational states of the  $H_2$  molecule. In Figure 2-8, we also seen the relatively strong emission



line at 3.3724 eV ( $D^0_{2X_B}$ ) that is attributed to the transition due to the B-free exciton bound to the same main neutral donor. The energy separation between this peak and the main peak at 3.3605 eV ( $D^0_{2X_A}$ ) is about 12 meV, which is consistent with the energy splitting of the A- and B-free exciton lines. In the lower energy part of the PL spectrum, ABEs at 3.3564 ( $A^0_{1X_A}$ ), 3.3530 ( $A^0_{2X_A}$ ), and 3.3481 eV ( $A^0_{3X_A}$ ) are also observed. However, relative peak intensities of the particular donor-related exciton lines show some differences from sample to sample. This is because the concentration of the particular donor could vary from sample to sample as well as its capture cross section.

### 2.2.2.3 Two-electron satellites [14]

Next, two electron satellites related to the donor-bound excitons are discussed. Another characteristic of the neutral-donor-bound exciton transition is the two-electron satellite (TES) transitions in the spectral region of 3.32–3.34 eV. These transitions involve radiative recombination of an exciton bound to a neutral donor, leaving the donor in the excited state. In the effective mass approximation, the energy difference between the ground-state neutral DBEs and their excited states (TES) can be used to determine the donor binding energies (the donor excitation energy from the ground state to the first excited state equals to 3/4 of the donor binding energy,  $E_D$ ) and catalog the different species present in the material. The spectral region for the expected two-electron satellite transitions is shown in Fig. 2-9 for the ZnO single crystal. The main peak at 3.3224 eV ( $(D^0_{2X_A})_{2e}$ ) is the excited state associated with the most intense neutral DBE at 3.3605 eV ( $D^0_{2X_A}$ ). The shoulder seen at about 3.3268 eV ( $(D^0_{3X_A})_{2e}$ ) on the high-energy side of the main TES peak is related to the excited state of the donor whose ground state emission is at 3.3618 eV

$(D^0_3X_A)$ . A weak emission at 3.3364 eV  $(D^0_4X_A)_{2e}$  is also attributed to the TES transition of the neutral donor whose ground state is at 3.3650 eV  $(D^0_4X_A)$ . From the separation of the ground state and the corresponding excited states, we were able to calculate the donor binding energies as 51 meV for the donor at 3.3605 eV, 47 meV for the donor at 3.3618, and 38 meV for the donor at 3.3650 eV.

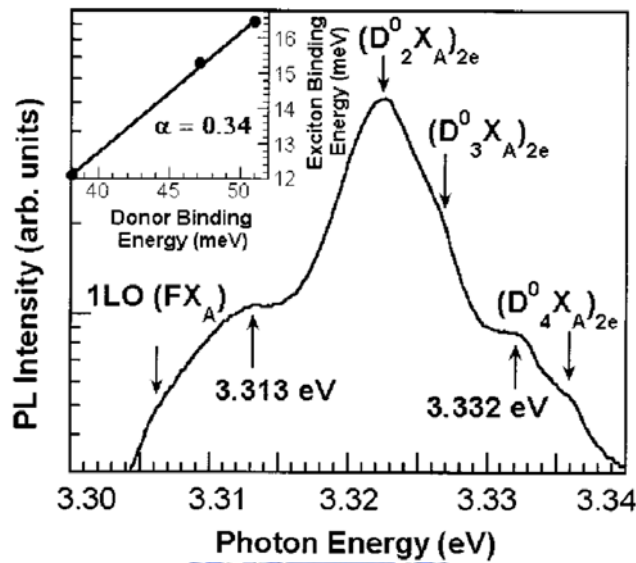


Fig. 2-9 10 K PL spectrum in the TES region of the main bound exciton lines. [14]

From the separation between the A-free exciton and the ground-state neutral DBEs, we can also determine the binding energies of these excitons as 16.5 meV (for 3.3605 eV), 15.3 meV (for 3.3618 eV), and 12.1 meV (for 3.3560 eV). According to the empirical Haynes rule, the binding or localization energy of the DBEs is proportional to the binding energy of the corresponding donor. Indeed, this relation is clearly seen in the inset of Fig. 2-9. Additionally, there are two additional peaks at 3.332 and 3.313 eV on both sides of the main TES lines, which could not be identified at this point, but they may be related to the excitons bound to structural defects.

#### 2.2.2.4 LO-phonon replicas [14]

As indicated in Fig. 2-10, the bump at the higher energy side of the spectrum labeled as 1LO ( $FX_A$ ) has a peak around 3.306 eV, which is the expected value for the 1LO-phonon replica of the free exciton peak (about 71 meV apart from the  $FX_A^{n=1}$  free-exciton peak). Although weak, second and third order LO phonon replicas labeled as 2LO ( $FX_A$ ) and 3LO ( $FX_A$ ) are also observed in the PL spectrum. It should be noted that LO-phonon replicas occur with a separation of 71–73 meV, which corresponds to the LO-phonon energy in ZnO.

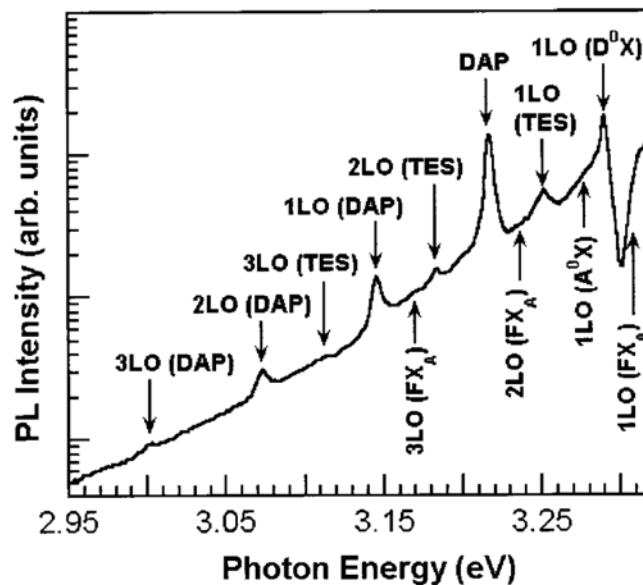


Fig. 2-10 10 K PL spectrum in the region where DAP transition and LO-Phonon replicas are expected to appear. [14]

The peak at 3.2898 is the first LO-phonon replica of both 3.3618 and 3.3605 eV lines, whereas the first LO-phonon replica of 3.3650 eV line is seen as a shoulder on the high-energy side of this intense peak. Resolving the second and higher order LO replicas is even harder because the energy position (3.218–3.223 eV) falls in the

spectral region where the DAP transition and its LO phonon replicas are expected to appear (will be described in the following section). In fact, we observed a radiative recombination peak at 3.217 eV that is attributed to the DAP (labeled as DAP in Fig. 2-10 along with its first, second, and third LO-phonon replicas at 3.145, 3.073, and 3.001 eV, respectively). We can resolve at least two closely spaced peaks at 3.2898 and 3.2920 eV, which are about 72 meV apart from the main neutral DBE lines at 3.3605 and 3.3650 eV. Moreover, LO-phonon replicas are expected to be roughly two orders of magnitude less intense than the neutral DBE lines due to donor-related bound exciton lines couple only weakly with the optical phonons. The relatively broad peak around 3.280 eV is the first LO-phonon replica associated with the most intense ABE line (3.3564 eV). This is indicated as 1LO ( $A^0X$ ) in Fig. 2-10. Finally, first, second, and third order LO-phonon replicas of the TES lines are also clearly observed in the PL spectra. These peaks are labeled as 1LO, 2LO, and 3LO-TES and they are positioned at 3.252, 3.182, and 3.112 eV, respectively.

### 2.2.3 Defect emission [1,18]

Besides exciton-related emissions in the photon energy range of 3.25–3.4 eV, PL spectrum of ZnO usually contains a sharp peak at about 3.22 eV followed by at least two LO-phonon replicas. This emission has been attributed to the DAP transitions involving a shallow donor and a shallow acceptor. This conclusion is based mostly on a characteristic transformation of the DAP emission lines to similar, but shifted, emission lines arising from transitions from the conduction band to the same shallow acceptor ( $e-A$  transitions) with increasing temperature. The DAP line quenches and gives way to the  $e-A$  line at elevated temperatures due to thermal ionization of the shallow donors. From the position of the  $e-A$  and DAP lines, the ionization energy

of the unintentional shallow acceptor in ZnO can be estimated.

In addition to UV excitonic emission peak, ZnO commonly exhibits luminescence in the visible spectral range with dissimilar emission wavelengths due to intrinsic or extrinsic defects. The origin of these emissions, including three different types of defects (green at  $\sim 2.3$  eV, yellow at  $\sim 2.1$  eV, and red at  $\sim 1.8$  eV), has been controversial, especially the green emission. Assignment of various defect emissions to the specific transitions in ZnO is often complicated by the presence of multiple emissions and broad emission peaks containing contributions from multiple transitions. Different fabrication conditions (pressure, temperature, flow rate, etc.) resulted in different defect types and concentrations resulting in different luminescence spectra.

A number of different hypotheses have been proposed to explain the green emission, such as transition between singly ionized oxygen vacancy and photoexcited hole, transition between electron close to the conduction band and a deeply trapped hole at  $V_o^{++}$ , surface defects, etc. While green emission is typically associated with oxygen deficiency, yellow/orange emission is associated with excess oxygen. The yellow/orange defect emission observed in ZnO synthesized by a hydrothermal method is typically assigned to interstitial oxygen, although other hypotheses such as dislocation related luminescence centers and the DAP-type transitions including a shallow donor and the Li acceptor dominate at low temperatures have been proposed. The assignment of the emission to interstitial oxygen has been confirmed by reduction of this emission after annealing in a reducing environment. Unlike green emission, yellow emission is not significantly influenced by the surface modifications. On the other hand, red-orange emission (peak position at  $\sim 640$ – $680$  nm or  $\sim 1.8$ – $1.9$  eV) has been less commonly observed than green and yellow emissions.

#### 2.2.4 Biexciton and exciton-exciton scattering [6,19]

The PL features as mentioned above are under low excitation intensity. With increasing excitation intensity we reach the so-called intermediate density regime. There are, e.g., elastic and inelastic scattering processes between excitons and (at higher temperature) between excitons and free carriers due to excitons density is so high that they start to interact with each other in the regime. These scattering processes may lead to a collision-broadening of the exciton resonances and to the appearance of new luminescence bands, to an excitation-induced increase of absorption, to bleaching, or to optical amplification, i.e., to gain or negative absorption depending on the excitation conditions. Another group of coherent and incoherent interaction processes in this intermediate density regime involves transitions to the excitonic molecule or biexciton. The biexciton is a quasiparticle which consists of two electrons and two holes. If we pump the sample even harder, we leave the intermediate and arrive at the high density regime, where the excitons lose their identity as individual quasiparticles and where a new collective phase is formed which is known as the electron-hole plasma.

In the system with high density of excitons are created in crystal, the biexciton decay can be explained by the following channels indicating in Fig. 2-11(a). (1) As a result of the biexciton decay a lightlike state  $m_t$  of the LPB and an excitonlike state of the LPB are formed. On reaching the crystal surface the lightlike polariton escapes as a luminescence photon  $m_t$ . (2) The biexciton causes a lightlike state of the LPB and a longitudinal exciton state. Reaching the crystal surface the lightlike polariton escapes as a photon  $m_l$ . Figure 2-11(b) diagramed the inelastic exciton-exciton scattering process. As a result of such scattering, one exciton is

excited into a higher state ( $n = 2, 3, 4, \dots, \infty$ ), while the other exciton loses its kinetic energy to occupy the lower polariton branch, whose energy can be given by

$$E_n = E_{ex} - E_b^{ex} \left( 1 - \frac{1}{n^2} \right) - \frac{3}{2} kT \quad (2.16)$$

where  $E_b^{ex} = 60\text{meV}$  is the exciton binding energy of ZnO, and  $kT$  is the thermal energy.

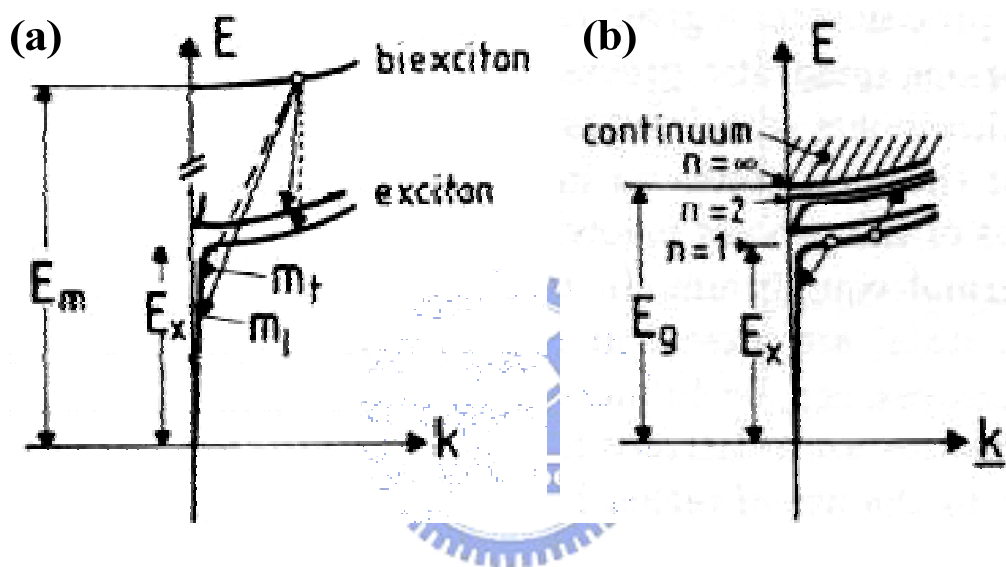


Fig. 2-11 Inelastic scattering processes in the intermediate density regime: biexciton decay (a) and inelastic exciton-exciton scattering (b). [6]

Next, we give an example experimentally related to PL characteristic features of both processes. Figure 2-12 shows PL spectra obtained under various excitation densities in ZnO epitaxial thin films. The lowest curve shows a low-excitation PL spectrum obtained using a continuous wave (cw) He–Cd laser ( $\lambda = 325\text{ nm}$ ). PL due to a free exciton is observed at 3.370 eV and is denoted by  $X$ . There are two peaks at the lower energy side of the  $X$  band which are due to bound excitons ( $I_2$  : 3.362 eV,  $I_4$  : 3.357 eV). The PL band at 3.309 eV denoted by  $X$ -1LO is a 1-LO phonon-assisted

radiative recombination of free excitons. As the excitation intensity increases, a new PL peak, denoted  $M$ , appears at 3.35 eV. With a further increase in excitation intensity above  $470 \text{ W/cm}^2$ , a second peak, denoted  $P$ , emerges at  $\sim 3.32 \text{ eV}$  [Fig. 2-12(d)]. The  $P$  band shifts toward the lower energy side as the excitation intensity increases further. According to previous statements, the  $P$  band originates from inelastic scattering between excitons. The energy of such scattering is roughly located between  $3.318 \text{ eV}$  ( $n = 2$ ) and  $3.303 \text{ eV}$  ( $n = \infty$ ) according to the expression (2.16).

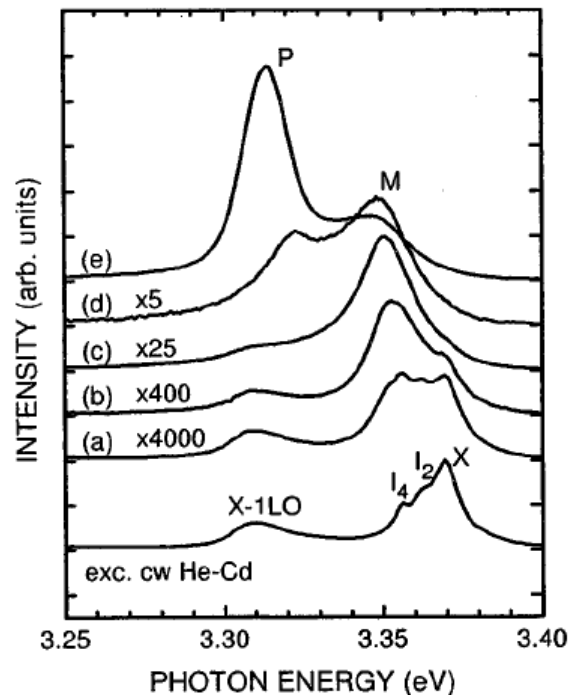


Fig. 2-12 PL spectra of a ZnO epilayer for various excitation intensities of (a) 2.9, (b) 15, (c) 150, (d) 930, and (e)  $4700 \text{ W/cm}^2$  at 77 K. [19]

The integrated PL intensity of the  $M$  band increases superlinearly with increasing excitation density. The asymmetric spectral shape and nonlinear excitation intensity dependence strongly suggest that the  $M$  band is due to a biexciton state. The binding energy of the biexciton is estimated to be 15 meV, which agrees well with the



reported value, 14.7 meV. The kinetics of excitons with increase in excitation intensity would be qualitatively understood as follows. As the excitation intensity increases, the probability of association of excitons becomes frequent, which leads to the formation of biexcitons. With further increase in excitation intensity, the kinetic energy of some of the excitons becomes higher than the biexciton binding energy, which would enhance inelastic exciton–exciton scattering. Hence, the *M* band is gradually taken over by the *P* band, as the excitation intensity increases further.



## References

- [1] Ü. Özgür, Ya. I. Alivov, C. Liu, A. Teke, M. A. Reshchikov, S. Doğan, V. Avrutin, S.-J. Cho, and H. Morkoç, *J. Appl. Phys.* **98**, 041301 (2005).
- [2] R. Loudon, *Adv. Phys.* **50**, 813 (2001).
- [3] M. A. Stroschio and M. Dutta, “*Phonons in Nanostructures*” (Cambridge university press, United Kingdom 2001).
- [4] J. M. Calleja and M. Cardona, *Phys. Rev. B* **16**, 3753 (1997).
- [5] A. P. Jephcoat, R. J. Hemley, H. K. Mao, R. E. Cohen, and M. J. Mehl, *Phys. Rev. B* **37**, 4727 (1988).
- [6] C. F. Klingshirn, “*Semiconductor Optics*” (Springer, Berlin, 1997).
- [7] M. Ueta, H. Kanzaki, K. Kobayashi, Y. Toyozawa, and E. Hanamura, “*Excitonic Processes in Solids*” (Springer-Verlag, Berlin, 1984).
- [8] K. J. Button, D. R. Cohn, M. Ortenbert, B. Lax, E. Mollwo, and R. Helbig, *Phys. Rev. Lett.* **28**, 1637 (1972).
- [9] W. S. Bear, *Phys. Rev.* **154**, 785 (1966).
- [10] R. T. Senger, and K. K. Bajaj, *Phys. Rev. B* **68**, 045313 (2003).
- [11] K. F. Lin, H. M. Cheng, H. C. Hsu, L. J. Lin, and W. F. Hsieh, *Chem. Phys. Lett.* **409**, 208 (2005).
- [12] Y. Gu, I. L. Kuskovsky, M. Yin, S. O’Brien, and G. F. Neumark, *Appl. Phys. Lett.* **85**, 3833 (2004).
- [13] G. Xiong, U. Pal, and J. G. Serrano, *J. Appl. Phys.* **101**, 024317 (2007).
- [14] A. Teke, Ü. Özgür, S. Doğan, X. Gu, and H. Morkoç, *Phys. Rev. B* **70**, 195207 (2004).
- [15] D. C. Reynolds, D. C. Look, B. Jogai, C. W. Litton, G. Cantwell, and W. C. Harsch, *Phys. Rev. B* **60**, 2340 (1999).
- [16] K. Thonke, Th. Gruber, N. Teofilov, R. Schönfelder, A. Waag, and R. Sauer,

Physica B **308–310**, 945 (2001).

[17] C. Boemare, T. Monteiro, M. J. Soares, J. G. Guilherme, and E. Alves, Physica B **308–310**, 985 (2001).

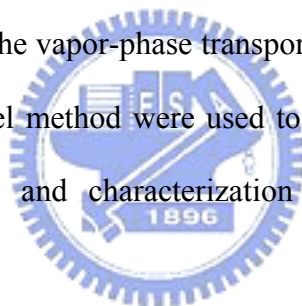
[18] A. B. Djurišić, Y. H. Leung, K. H. Tam, L. Ding, W. K. Ge, H. Y. Chen, and S. Gwo, Appl. Phys. Lett. **88**, 103107 (2006).

[19] A. Yamamoto, K. Miyajima, T. Goto, H. J. Ko, and T. Yao, J. Appl. Phys. **90**, 4973 (2001).



## **Chapter 3 Experimental procedures and characterization techniques**

Incorporating Mg into ZnO has been obtained by molecular beam epitaxy [1,2], metalorganic vapor-phase epitaxy [3], and pulsed laser deposition [4-8] techniques etc. However, these methods are expensive and require high vacuum and formation controlling conditions. Compared with these methods, the sol-gel process is an attractive technique for compound semiconductors preparation because of its simplicity, low costs, and ease of composition control.[9,10] In particular, it has the potential to produce samples with large areas and complicated forms on various substrates. In this research, the vapor-phase transport via a vapor-liquid-solid (VLS) mechanism [11,12] and sol-gel method were used to fabricate MgZnO alloys. The detailed growth mechanisms and characterization techniques of the alloys are discussed as follows.



### **3.1 Synthesis mechanism**

#### **3.1.1 Vapor-Liquid-Solid (VLS) method**

Among all vapor based methods, the VLS methods seem to be the most successful for fabricating nanowires with single crystalline structures and in relatively large quantities. A typical VLS process starts with the dissolution of gaseous reactants into nano-sized liquid droplets of catalyst metal while the liquid droplets are supersaturated with the guest material, followed by nucleation and growth of single crystalline nanorods and then nanowires. The one-dimensional growth is mainly induced and dictated by the liquid droplets, whose size remains essentially unchanged

during the entire process of nanowire growth. In the sense, each of liquid droplets serves as a soft template to strictly limit the lateral growth of an individual nanowire. As a major requirement, there should exist a good solvent capable of forming liquid alloy with the target material, ideally they should be able to form eutectic compounds.

The formation procedure of one-dimensional nanostructure in the VLS method is shown in Fig. 3-1 [13], which demonstrates the formation of semiconductor nanowire using metal catalyst. The reactant metal vapor which could be generated by the thermal evaporation is condensed to the catalyst metal to form a liquid alloy nanocluster as the temperature is low. Nanowires grown after the liquid metal alloys become supersaturated and continue as long as the metal nanoclusters remain in a liquid state. Growth of nanowires will be terminated as the temperature reduces to the point that the metal nanoclusters solidify.

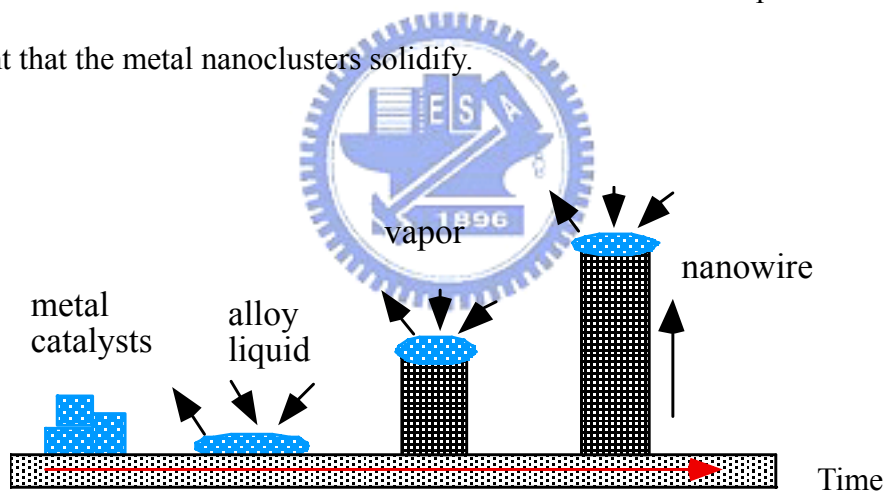


Fig. 3-1 VLS method. [13]

### 3.1.2 Sol-gel process

A colloid is a suspension in which the dispersed phase is so small (~1-1000 nm) that the gravitational force is negligible and interactions are dominated by the short-range forces, such as Van der Waals attraction and surface charge. Sol-gel synthesis has two ways to prepare solution. One way is the metal-organic route with metal alkoxides in organic solvent; the other way is the inorganic route with metal

salts in aqueous solution. It is much cheaper and easier to handle than metal alkoxides, but their reactions are more difficult to control. The metal-organic route uses metal alkoxides in organic solvent. The inorganic route is a step of polymerization reactions through hydrolysis and condensation of metal alkoxides  $M(OR)^Z$ , where  $M = Si, Ti, Zr, Al, Sn, Ce$ , and  $OR$  is an alkoxy group and  $Z$  is the valence or the oxidation state of the metal. First, hydroxylation upon the hydrolysis of alkoxy groups:



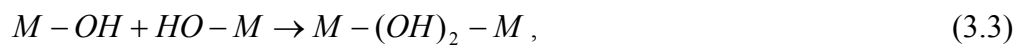
The second step, polycondensation process, leads to the formation of branched oligomers and polymers with a metal oxygenation based skeleton and reactive residual hydroxyl and alkoxy groups. There are 2 competitive mechanisms:

(1) Oxolation: formation of oxygen bridges:



The hydrolysis ratio ( $h = H_2O/M$ ) decides  $X = H$  ( $h \gg 2$ ) or  $X = R$  ( $h < 2$ ).

(2) Olation: formation of hydroxyl bridges when the coordination of the metallic center is not fully satisfied ( $N - Z > 0$ ):



where  $X = H$  or  $R$ . The kinetics of olation is usually faster than those of oxolation.

Figure 3-2 presents a schematic of the routes that one could follow within the scope of sol-gel processing.[14] A sol is a colloidal suspension of solid particles in a liquid, whereas, an aerosol is a colloidal suspension of particles in a gas (the suspension may be called a fog if the particles are liquid and a smoke if they are solid) and an emulsion is a suspension of liquid droplets in another liquid. All of these types of colloids can be used to generate polymers or particles from which ceramic

materials can be made. In the sol-gel process, the precursors (starting compounds) for preparation of a colloid consist of a metal or metalloid element surrounded by various ligands.

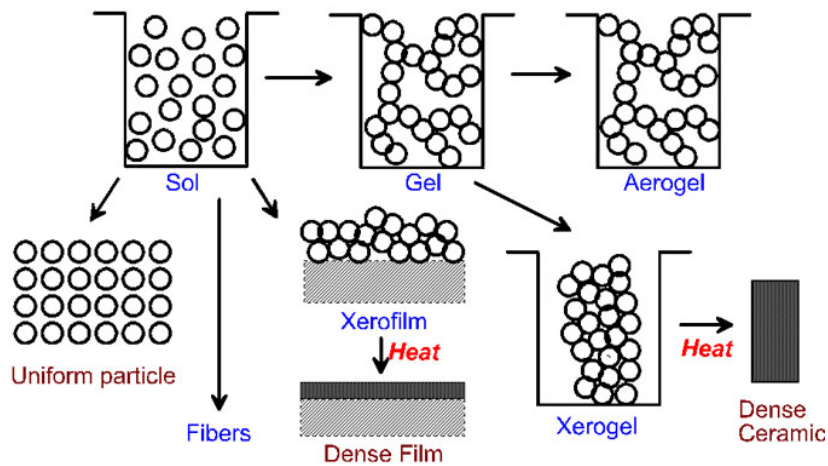


Fig. 3-2 Schematic of the routes that one could follow within the scope of sol-gel processing.

Metal alkoxides are members of the family of metalorganic compounds, which have an organic ligand attracted to a metal or metalloid atom. Metal alkoxides are popular precursors because they react readily with water. The reaction is called hydrolysis, because a hydroxy ion becomes attached to the metal atom. This type of reaction can continue to build larger and larger molecules by the process of polymerization. A polymer is a huge molecule (also called a macromolecule) formed from hundreds or thousands of units called monomers. If one molecule reaches macroscopic dimensions so that it extends throughout the solution, the substance is said to be gel. The gel point is the time (or degree of reaction) at which the last bond is formed that completes this giant molecule. It is generally found that the process begins with the formation of fractal aggregates that they begin to impinge on one another, then those clusters link together as described by the theory of percolation. The gel point corresponds to the percolation threshold, when a single

cluster (call the spanning cluster) appears that extends throughout the sol; the spanning cluster coexists with a sol phase containing many smaller clusters, which gradually become attached to the network.

## 3.2 Sample preparation

### 3.2.1 ZnMgO nanostructures formed by Mg in-diffused ZnO nanowires

ZnO nanowires were synthesized in a simple vapor transport process mediated by “self-catalyst” VLS growth [15] in a horizontal quartz tube furnace. An alumina boat contained the *c*-plane sapphire (0001) substrate and zinc powder was positioned in the center of the quartz tube furnace. Pure Zn metal powder (99.999%) was used as the zinc vapor source. The tube first was evacuated to a pressure below 10 Torr using a mechanical pump; then, the furnace was heated to 550°C at a rate of 50°C/min and high-purity argon gas was injected into the quartz tube at a flow rate of 500 sccm during 1 h of growth. After the growth process was complete, the tube furnace was cooled slowly to room temperature (RT) in Ar-gas ambience.

Although the quartz tube furnace was evacuated to a pressure below 10 Torr, there still contains enough residual O<sub>2</sub> to react with the condensate Zn vapor to form ZnO<sub>*x*</sub> (*x* < 1) in the initial period of nucleation.[16] Because the melting points of Zn and ZnO<sub>*x*</sub> are approximately 419 °C, simultaneously, the liquid phase Zn or ZnO<sub>*x*</sub> would serve as the eutectic solvent for the oxide species. The anisotropic growth of the crystal causes formation of a ZnO (further oxidation by the residual O<sub>2</sub>) nanostructure with a high aspect ratio and the ZnO nanowires are preferentially oriented along the *c*-axis direction due to the growth rate being fastest in this direction.

The ZnO nanowires were then spin-coated by the solution prepared by the



sol-gel approach using acetate of magnesium in a homogeneous aqueous reaction medium. Finally, the samples were sintered at 1000°C for 2 h while diffusion occurred to form the alloy.

### **3.2.2 $Mg_xZn_{1-x}O$ submicropowders synthesized by varying volume ratio of MgO/ZnO**

MgZnO submicropowders were synthesized by the following procedure. Stoichiometric zinc acetate dihydrate [99.5%  $Zn(OAc)_2 \cdot 2H_2O$ , Riedel-deHaen] and magnesium acetate tetrahydrate [99.5%  $Mg(OAc)_2 \cdot 4H_2O$ , Riedel-deHaen] were individually dissolved into diethylene glycol [99.5% DEG, ethylenediamine-tetra-acetic acid (EDTA)] to make 0.1M solutions. The resultant solutions were put separately in a centrifuge operating at 3000 rpm for 30 minutes, and transparent solutions were obtained containing dispersed single crystalline ZnO and MgO nanocrystals, respectively. Next, we mixed the supernatant solutions of ZnO and MgO nanocrystals with desired volume fractions, which were dropped onto sapphire (0001) substrates and dried at 150°C. The Mg contents were controlled by varying the volume ratio of MgO- and ZnO-supernatant solutions from 0–40%. Finally, all the samples were annealed in a furnace at 900°C under air atmosphere for 1 hour, then slowly cooled down to RT.

### **3.2.3 $Mg_xZn_{1-x}O$ powders synthesized by varying molar ratio of Mg/Zn**

$Mg_xZn_{1-x}O$  powders were synthesized using the aqueous sol prepared by stoichiometric zinc acetate dihydrate [99.5%  $Zn(OAc)_2 \cdot 2H_2O$ , Riedel-deHaen] and magnesium acetate tetrahydrate [99.5%  $Mg(OAc)_2 \cdot 4H_2O$ , Riedel-deHaen] (Mg/Zn = 0, 3, and 5% in molar ratio) dissolved into methanol. The sol was dried in a furnace

at 900°C under air atmosphere for 1 hour, and then slowly cooled to RT.

### 3.3 Characterization of lattice dynamics

#### 3.3.1 X-ray Diffraction

The crystal structure were inspected by Bede D1 diffractometer at Industrial Technology Research Institute using a CuK X-ray source ( $\lambda = 1.5405\text{\AA}$ ). We used small angle diffraction. The  $\omega$  was fixed at  $5^\circ$ , the scanning step was  $0.04^\circ$ , scanning rate was 4 degree/min and count time was 1.00 second. Figure 3-3 shown XRD  $\omega$ - $2\theta$  scans geometry. The dashed lines mean the trajectory of the incident beam and the detector to be in motion.

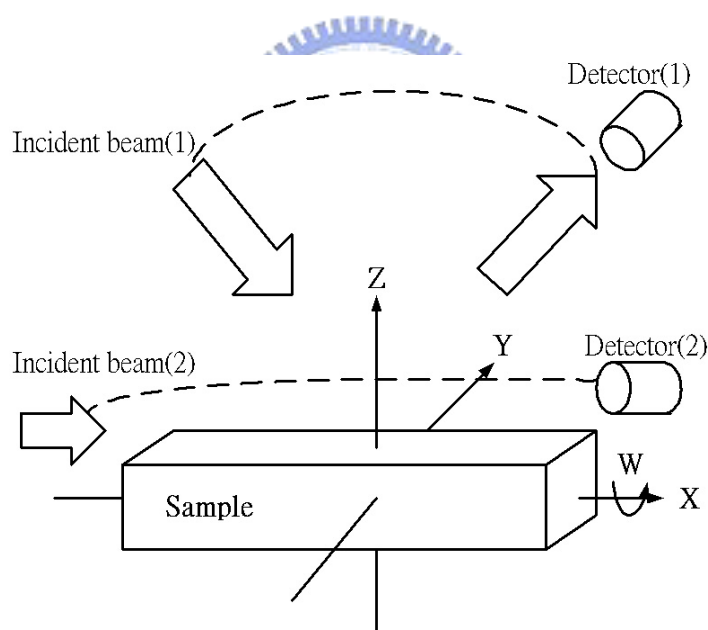


Fig. 3-3 XRD  $\omega$ - $2\theta$  scans geometry.

#### 3.3.2 Scanning Electron Microscopy

The morphology of the products was characterized by field-emission scanning electron microscope (SEM, LEO 1530 and JEOL-2100F).

### 3.3.3 Raman scattering measurement

The experimental setup of Raman spectroscopy consists mainly of three components: a laser system serves as a powerful, monochromatic light source and a computer controlled spectrometer for wavelength analysis of the inelastically scattered light. Figure 3-4 shows the experimental setup schematically. The micro-Raman system was performed in the backscattering geometry with a confocal Olympus (BX-40) optical microscope. The scattered light was dispersed through the triple-monochromator system and detected by a liquid-nitrogen-cooled charge coupled device (CCD). The 515 nm line of a frequency-doubled Yb:YAG laser was used as the Raman excitation source. The best spatial resolution during Raman measurements was 1.0  $\mu\text{m}$  with a spectral resolution of 0.2  $\text{cm}^{-1}$ . Similarly, micro-Raman spectroscopy was carried out using  $\text{Ar}^+$  laser (Coherent INNOVA 90) as the excitation source emitting at a wavelength of 488 nm with power of 40mW, and a SPEX 1877C triple-grating spectrograph equipped with a liquid nitrogen-cooled CCD at 140 K.

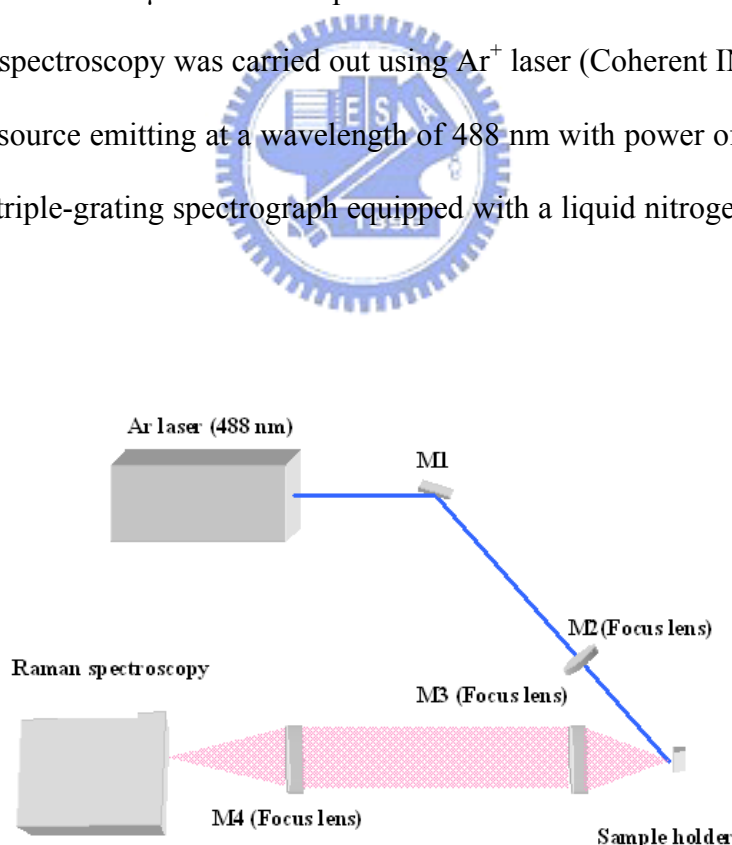


Fig. 3-4 The scheme of the Raman system.

### 3.4 Characterization of optical properties

#### 3.4.1 Photoluminescence system

For photoluminescence (PL) measurement, we used a He–Cd laser ( $\lambda = 325 \text{ nm}$ ) as the excitation source. The schematic of the PL system is shown in Fig 3-5. The excitation laser beam was directed normally and focused onto the sample surface with power being varied with an optical attenuator. The spot size on the sample is about  $100 \mu\text{m}$ . Spontaneous and stimulated emissions were collected by a fiber bundle and coupled into a 0.32 cm focal-length monochromator (TRIAX 320) with a 1200 lines/mm grating, then detected by either an electrically cooled CCD (CCD-3000) or a photomultiplier tube (PMT-HVPS) detector. The temperature-dependent PL measurements were carried out using a closed cycle cryogenic system. A closed cycle refrigerator was used to set the temperature anywhere between 15 K and 300 K.

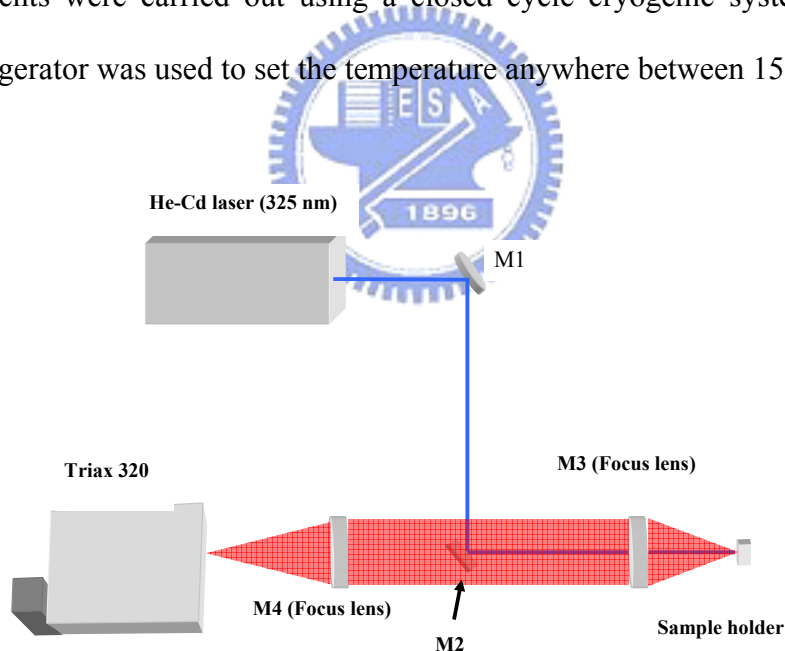


Fig. 3-5 PL detection system.

#### 3.4.2 Optical absorption system

Optical transmission or absorption measurements are routinely used by chemists to determine the constituents of chemical compounds. Optical absorption spectra

were made using a deuterium lamp and the emission light was dispersed by a TRIAX-320 spectrometer and detected by a UV-sensitive PMT. Figure 3-6 is a schematic diagram showing the absorption system.

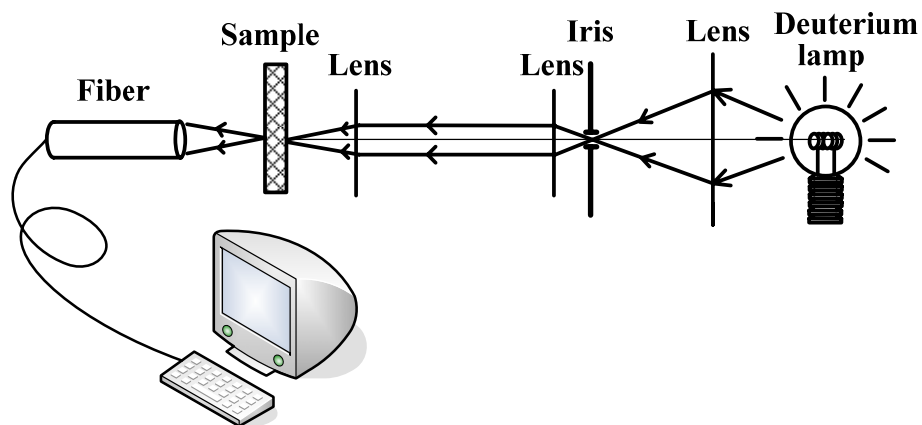


Fig. 3-6 Optical absorption system.



## References

- [1] H. Shibata, H. Tampo, K. Matsubara, A. Yamada, K. Sakurai, S. Ishizuka, and S. Niki, and M. Sakai, *Appl. Phys. Lett.* **90**, 124104 (2007).
- [2] C. R. Ding, S. W. Li, and H. Z. Wang, *Appl. Phys. Lett.* **90**, 241918 (2007).
- [3] W. I. Park, G. C. Yi, and H. M. Jang, *Appl. Phys. Lett.* **79**, 2022 (2001).
- [4] A. I. Belogorokhov, A. Y. Polyakov, N. B. Smirnov, A. V. Govorkov, E. A. Kozhukhova, H. S. Kim, D. P. Norton, and S. J. Pearton, *Appl. Phys. Lett.* **90**, 192110 (2007).
- [5] A. Ohtomo, M. Kawasaki, T. Koida, K. Masubuchi, H. Koinuma, Y. Sakurai, Y. Yoshida, T. Yasuda, and Y. Segawa, *Appl. Phys. Lett.* **72**, 2466 (1998).
- [6] S. Choopun, R. D. Vispute, W. Yang, R. P. Sharma, T. Venkatesan, and H. Shen, *Appl. Phys. Lett.* **80**, 1529 (2002).
- [7] M. Lorenz, E. M. Kaidashev, A. Rahm, Th. Nobis, J. Lenzner, G. Wagner, D. Spemann, H. Hochmuth, and M. Grundmann, *Appl. Phys. Lett.* **86**, 143113 (2005).
- [8] F. K. Shan, B. I. Kim, G. X. Liu, Z. F. Liu, J. Y. Sohn, W. J. Lee, B. C. Shin, and Y. S. Yu, *J. Appl. Phys.* **95**, 4772 (2004).
- [9] A. E. Jimenez-Gonzalez, J. A. Soto Urueta, and R. Suarez-Parra, *J. Cryst. Growth* **192**, 430 (1998).
- [10] D. Bao, H. Gu, and A. Kuang, *Thin Solid Films* **312**, 37 (1998).
- [11] M. H. Huang, Y. Wu, H. Feick, N. Tran, E. Weber and P. D. Yang. *Adv Mater* **13**, 113 (2001).
- [12] M. H. Huang, S. Mao, H. Feick, H. Yun, Y. Wu, H. Kind, E. Weber, R. Russo, and P. D. Yang. *Science* **292**, 1897 (2001).
- [13] Y. Wu and P. Yang. *J. Am. Chem. Soc.* **123**, pp. 3165 (2001).
- [14] C. J. Brinker and G. W. Scherer, “*Sol-Gel Science*”, pp. 303.

[15] H. C. Hsu, H. M. Cheng, C. Y. Wu, H. S. Huang, Y. C. Lee and W. F. Hsieh,  
Nanotechnology **17**, 1404 (2006).

[16] B. D. Yao, Y. F. Chan and N. Wang, Appl. Phys. Lett. **81**, 457 (2002).



## Chapter 4 Raman study of Mg incorporation in MgZnO

### alloys

In an “ideal” crystal with translational symmetry, the spatial correlation function of the phonon is infinite and in a form of plane wave. This results in the usual  $q = 0$  selection rules of Raman scattering. However, in ternary semiconductor alloys, impurity incorporations induced not only topological disorder but also structural disorder. These disorders result basically in the breakdown of translational symmetry of the periodic lattice, which yields the finite of mode correlations and a partial relaxation of the  $q = 0$  selection rule. That is, the  $q \neq 0$  phonons also contributed to Raman scattering. Therefore, the Raman spectra show changes of various phonon modes with compositional disorder, including emergence of local lattice vibration and disorder-activated modes, a shift in phonon frequency and changes of the linewidth and asymmetry.

In ternary semiconductor alloys, the microscopic alloy disorder depends on the growth parameters as well as the alloy composition. In this chapter, two distinct processes were used to fabricate MgZnO compound semiconductors and their Raman vibrational properties were characterized spectroscopically. Raman spectroscopy is a versatile technique for fast and nondestructive study of dopant incorporation, particularly, when impurity-induced modes can be traced back to individual constituents. The difference in sample preparation procedures between two sections lies in the former approach could synthesize the samples with well crystallinity, i.e., intense Raman intensity. Nevertheless, the latter approach has an advantage in that it could modulate the Mg contents in  $\text{Mg}_x\text{Zn}_{1-x}\text{O}$  alloys effectively, i.e.,



Mg-incorporation dependent Raman mode.

## **4.1 Structural and optical properties of ZnMgO nanostructures formed by Mg in-diffused ZnO nanowires**

Recently, Kaschner *et al.* [1] observed anomalous modes (AMs) at about 275, 510, 582, and 643  $\text{cm}^{-1}$  in ZnO:N films and explained the occurrence as local vibrational modes (LVMs) due to vibrating nitrogen-related complexes, Bundesmann *et al.* [2] suggested the same additional modes resulting from the host lattice defects by intentionally doping Fe, Sb, and Al, in the ZnO thin films without N. However, Manjon *et al.* [3] considered that most of the observed AMs correspond to wurtzite-ZnO silent modes allowed by the breakdown of the translational symmetry induced by defects and impurities based on their *ab initio* calculations [4]. Although several works of undoped- and doped-ZnO thin films observed the AMs in the Raman spectra, little was reported about the influence of magnesium incorporation on the lattice dynamics of ZnO. In this section, we reported the synthesis of the ZnMgO nanostructures, which can be achieved simply by thermal diffusion of Mg into the ZnO nanowires prepared by a simple vapor transport method [5]. The Mg composition in  $\text{ZnB}_{1-x}\text{Mg}_x\text{O}$  alloy can be estimated roughly by x-ray diffraction (XRD) and photoluminescence (PL). Especially, magnesium-related AMs are observed by Raman spectra for the first time in ZnMgO system.

### **4.1.1 Morphology**

The SEM images of Mg in-diffused ZnO nanowires (ZMO nanostructures) and ZnO nanowires having the same magnification are presented in Fig. 4-1 and its inset. The morphology of the ZnO nanowires (see the inset) displayed nearly well-aligned

nanowires uniformly distributed over the entire substrate; most of them were grown with length and diameters ranging about 1–2  $\mu\text{m}$  and 100–200 nm, respectively. The ZMO nanostructures consisted of fused filaments, which bundled several nanowires approximately 600–900 nm in diameter. Based on the SEM photographs, the cause of topological change of the obtained structures is illustrated as follows. According to the report of Hsu *et al.* [6], the formation of heterostructured ZnMgO alloy nanowires should result from post-heat treatment of the as-grown ZnO/MgO core-shell structure. In this experiment, in order to obtain the preformed ZnO/MgO core-shell structure, one would expect the solution could spread evenly on the outer layer of the nanowires by capillarity during the spin-coating process, whereas the excess solution had capped on top of the nanowires. After post-annealing treatment, Mg-based precipitates (see the bright region of the SEM image) on the head of fused nanowires correlated presumably with the above observation.

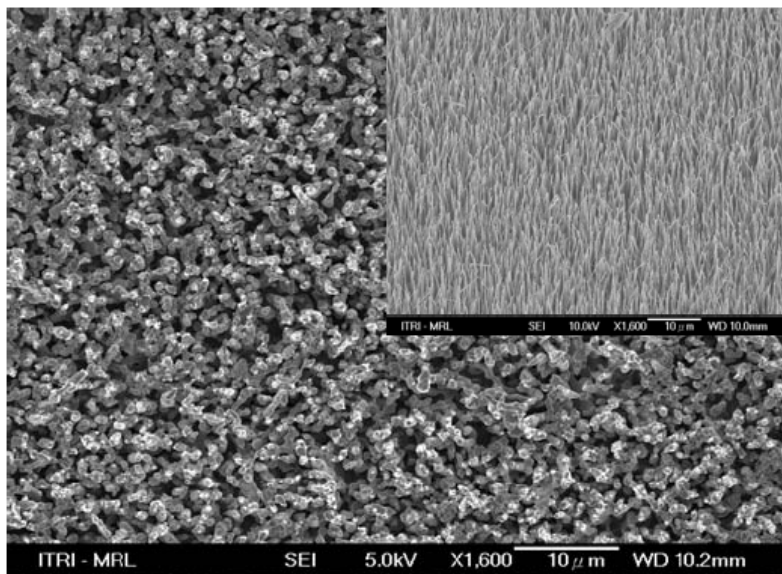


Fig. 4-1 The SEM images of the Mg in-diffused ZnO nanowires. The inset shows the original aligned ZnO nanowires.

#### 4.1.2 Determination of Mg concentration

Shown in Fig. 4-2 are the XRD patterns of the ZMO nanostructures in comparison with the ZnO nanowires. For the ZMO nanostructures, all relatively sharp diffraction peaks can be indexed perfectly to a high crystallinity of hexagonal phase of ZMO with two small signals (denoted by open circles) attributed to MgO cubic phase. The appearance of a secondary phase was due to the precipitates of MgO particles on the top of fused filaments, as described in the SEM image. Additionally, the observed diffraction data were analyzed, using Rietveld analysis software (GSAS), by taking into account the preferred orientation of (002) planes in both samples. The refinement results of ZMO nanostructures, which well fit to the data with  $R_{wp}=4.70\%$ , also are shown in Fig. 4-2.

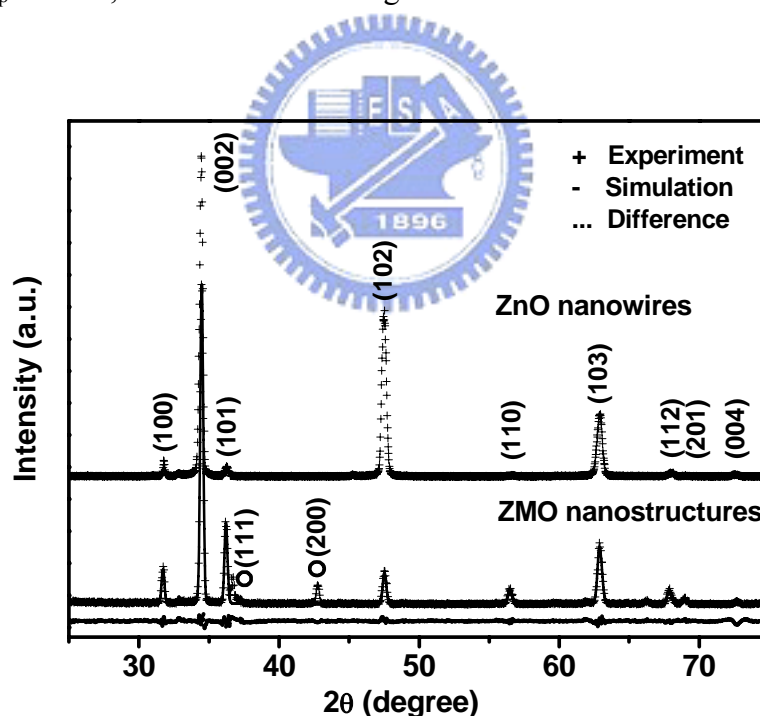


Fig. 4-2 The Rietveld refinement plot of ZMO nanostructures and ZnO nanowires. The open circles indicate the MgO cubic diffraction peaks.

The lattice constant  $a$  are refined to be 3.25394 and 3.25804 Å;  $c$  to be 5.21050 and 5.20251 Å, for ZnO nanowires and ZMO nanostructures, respectively. The

similar dependence of the lattice constant on Mg concentration usually is common in  $Zn_{1-x}Mg_xO$  systems.[7–9] Assume the lattice constant varies linearly following Vegard's law, we determined the Mg content to be  $12 \pm 2.7\%$  and  $8.2 \pm 0.1\%$  according to the relations  $a = 3.25394 + 0.0342x$  and  $c = 5.21050 - 0.097x$  that were deduced from figure 2 in Ref. [7]. Therefore, the variation of lattice constant suggests that  $Mg^{2+}$  is incorporated into the ZnO host lattice and occupies the lattice sites of  $Zn^{2+}$ .

Figure 4-3 shows the normalized room-temperature (RT) PL spectra of the ZMO nanostructures (solid curve) and the ZnO nanowires (short dashed curve). Two PL bands can be observed in the two spectra, one being in the ultraviolet (UV) and the other in the green. The UV emission is assigned to the near band edge (NBE) emission, which originates from the free exciton emission and its replicas.[5,10,11] The broad green emission is commonly attributed to intrinsic deep-level defects in ZnO such as oxygen vacancy, interstitial zinc, antisite oxygen, and ionic dopants.[12–15] Compared with the ZnO nanowires, two obvious differences can be found: the shift of NBE peak position of ZMO nanostructures to the higher energy from 3.26 to  $\sim 3.43$  eV and the increase of intensity of deep-level emission owing to the formation of ternary ZnMgO alloy via Mg diffusion. This blueshift cannot be caused by quantum confinement effects because the sizes of ZMO nanostructures are far larger than the exciton Bohr radius (2.34nm) of bulk ZnO. As a result, Mg doping should be responsible for such a blueshift. Additionally, the broadening of the NBE peak with the full width at half maximum (FWHM), with changing from 105 to 155 meV, is a result of the increase in fluctuation of composition and the lattice disorder in the alloy. The increasing deep-level emission probably comes from surface defects or lattice disorder caused by heat treatment. Therefore, due to the

Mg incorporation, the ZMO nanostructures exhibit the blueshift of NBE peak position and the increased intensity of deep-level emission.

In order to demonstrate the homogeneity of our samples, we measured PL spectra at a dozen points over the whole sample of  $\sim 20 \text{ mm}^2$  and calculated the Mg content based on the formula [16]:

$$E(\text{Zn}_{1-x}\text{Mg}_x\text{O}) = E(\text{ZnO}) + 1.64*x \text{ (eV)} \quad (4.1),$$

where the Mg content in the  $\text{Mg}_x\text{Zn}_{1-x}\text{O}$  thin films had been determined for  $0 \leq x \leq 0.2$ , grown by the pulsed laser deposition. Here,  $E(\text{Mg}_x\text{Zn}_{1-x}\text{O})$  and  $E(\text{ZnO})$  are the NBE emission peak positions of  $\text{Mg}_x\text{Zn}_{1-x}\text{O}$  and ZnO, respectively. The calculated Mg content of the ZMO nanostructures was  $9.5 \pm 1.1\%$ , which is close to that from XRD analysis. The blueshift of the UV emission demonstrated the band gap engineering of ZnO and further confirmed that the Mg ions had incorporated into the ZnO host lattice.

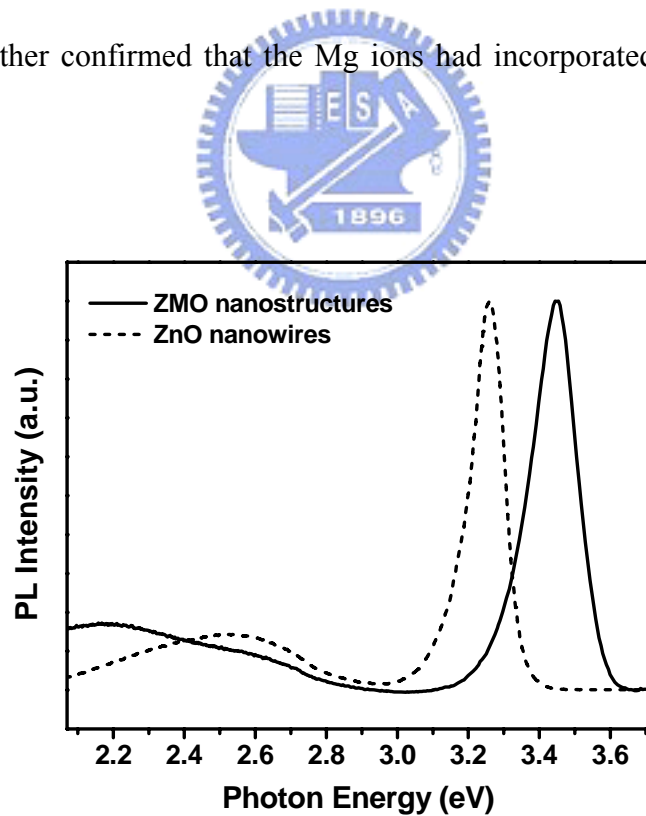


Fig. 4-3 The normalized room-temperature PL spectra of ZMO nanostructures (solid curve) and ZnO nanowires (short dash curve).

### 4.1.3 Raman spectra analysis

We then sought to investigate the influence of Mg doping on microscopic structures and vibrational properties for ZnMgO materials by micro-Raman spectroscopy with a fixed laser spot of about  $2 \mu\text{m}^2$ . The RT Raman spectra of both ZMO nanostructures and ZnO nanowires are shown in Fig. 4-4. We can see that the Raman peak at  $417 \text{ cm}^{-1}$  keeps unshifted in frequency that which comes from the sapphire substrate [2]. The assignments of all observed Raman lines are listed in Table 4-1, according to the previous Raman studies of ZnO.[17–21] It can be seen that although most of the Raman peaks from the ZMO nanostructures correspond well to those of the ZnO nanowires, the Raman spectra of ZMO nanostructures have shown their own characteristic. Firstly, it was interesting to note that  $E_2$  (high) phonon lines redshifted to the lower frequency from  $437.7$  to  $436.4 \text{ cm}^{-1}$  and broadened (FWHM) from  $8.23$  to  $15.3 \text{ cm}^{-1}$  as Mg was introduced into the ZnO nanowires. Secondly, the origin of the vibration mode around  $660 \text{ cm}^{-1}$  still is controversial. Thirdly, two additional AMs around  $383$  and  $510 \text{ cm}^{-1}$  were detected only for ZMO nanostructures, marked as triangles in Fig. 4-4.

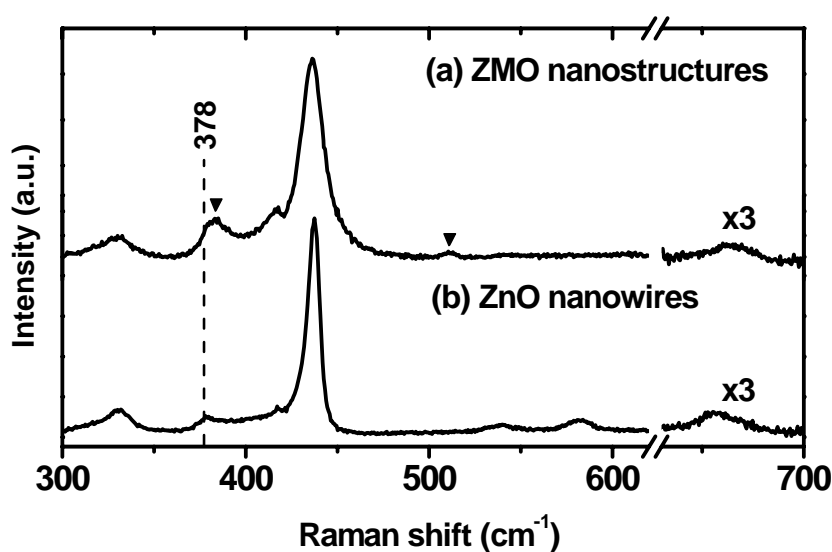


Fig. 4-4 The Raman spectra of ZMO nanostructures (a) and ZnO nanowires (b). Triangles denote the additional modes.

Table 4-1 Phonon modes frequencies in our work and tentative assignments of all the peaks.

$\omega_o(\text{cm}^{-1})$ ZMO nanostructures	$\omega_o(\text{cm}^{-1})$ ZnO nanowires	Assignments
330	330	$E_2(\text{high}) - E_2(\text{low})$ [20,21]
378	378	$A_1(\text{TO})$ [31]
383	—	AM
436	438	$E_2(\text{high})$ [19]
511	—	AM
—	540	$A_1(\text{LO})$ [19]
—	584	$E_1(\text{LO})$ [19]
<b>Broad, from 640-680</b>	<b>Broad, from 650-680</b>	<b><math>2[E_2(\text{high}) - E_2(\text{low})]</math> [20,21] or Intrinsic host lattice defect [28]</b>

In general, as the crystal is alloying, the phonons can be confined in space, owing to the potential fluctuations of the alloy disorder, which gives rise to a relaxation of the  $q=0$  selection rule in Raman scattering.[22,23] Several groups[1,24-26] discussed the same observations in a ZnO system doped with other elements (e.g., N, Mn, Co). Therefore, the spatial phonons confinement arose from alloy potential fluctuations, as  $\text{Mg}^{2+}$  random substitution induced the microscopic structural disorder in the periodic zinc atomic sublattice and broke the translational symmetry. Chen *et al.* [20] and Xing *et al.* [21] assigned the origin of  $660 \text{ cm}^{-1}$  peak to the multiphonon processes  $2[E_2(\text{high}) - E_2(\text{low})]$  in pure ZnO nanostructures whereas Cheng *et al.* [27] reported this mode in ZnO:Ce nanostructures and connected it with the metastable Ce-rich solid solution layer. In our experiments, the vibration mode around  $660 \text{ cm}^{-1}$  also is observed in ZnO nanowires; it should be an intrinsic mode of ZnO induced by  $\text{Mg}^{2+}$  substitution, which is analogous to Yang *et al.* [28] ascribed to intrinsic host lattice defects in Mn-doped ZnO nanostructures.

Furthermore, the AMs around 383 and 510  $\text{cm}^{-1}$  have not been observed in the previous works for ZnMgO systems. We tentatively suggested that these two structures are likely the LVMs related to magnesium. Equation (4.2) [29] gives us a rough estimate of the Mg-related LVM frequency from the effective reduced masses  $\mu = (1/M + 1/m)^{-1}$  of the ZnO and LVM:

$$\frac{\omega(LVM)}{\omega(ZnO)} \approx \sqrt{\frac{\mu_{ZnO}}{\mu_{LVM}}} \quad (4.2)$$

By using  $\omega(\text{ZnO-}E_2(\text{high}))=437.7 \text{ cm}^{-1}$  measured from ZnO nanowires, we obtained 373 and 505  $\text{cm}^{-1}$  for LVMs of Mg on substitutional O and Zn sites in the ZnO lattice, respectively. The calculated frequencies of LVMs for the Mg-Zn and Mg-O pairs are pretty close to the experimental values of 383 and 510  $\text{cm}^{-1}$ . Nevertheless, the line around 510  $\text{cm}^{-1}$  also has been observed in the Raman spectra of Fe-, Sb-, Al-, N- and Ga+N-doped ZnO films.[1,2,30] Owing to the large differences in mass among the dopant species, this 510- $\text{cm}^{-1}$  mode must be related to intrinsic host lattice defects rather than the above-mentioned LVM. Therefore, another possible explanation about the 510- $\text{cm}^{-1}$  band may be attributed to the host lattice defects induced by Mg incorporation. Due to the differences in the ionic radii of Mg impurity and host ions, when  $\text{Mg}^{2+}$  ions occupy the Zn sites, some new lattice defects are introduced or intrinsic host-lattice defects become activated. As a result, some additional vibrational modes, characteristic of substitution-induced vibrations, appear in the Raman spectra that probably connect with the raised intensity of deep-level emission.

In summary, the ZnMgO nanostructures with wurtzite structure were synthesized via thermal diffusion. The dependence of the lattice constant and the NBE emission at RT along with the observation of Mg-related Raman vibration on Mg incorporation confirmed  $\text{Mg}^{2+}$  substitution for  $\text{Zn}^{2+}$  lattice sites. In addition to the host phonons of



ZnO, we found two AMs at 383 and 510  $\text{cm}^{-1}$ , which correlated with the Mg-related lattice vibrations leading to the change in ZnO host lattice. The first-order  $E_2$  (high) phonon line of ZnO:Mg nanostructures was broadened and redshifted as a result of microscopic structural disorder induced by  $\text{Mg}^{2+}$  random substitution. Therefore, the influence of atom substitution on structural disorder is being explored to investigate the reduction of grain size in MgZnO nanostructures and will be addressed in the next section.

## 4.2 Raman study of alloy potential fluctuations in $\text{Mg}_x\text{Zn}_{1-x}\text{O}$ submicropowders

Recently, considerable attention has been devoted to the compositional dependence of the line shape (i.e., linewidth and asymmetry) of wurtzite  $E_2$  phonons using the spatial correlation (SC) model.[32, 33]. For example, Beserman *et al.* [34] have discussed the asymmetric behavior of the  $E_2$  Raman linewidth of  $\text{Al}_x\text{Ga}_{1-x}\text{N}$  alloys attributed to the activation of phonons of  $q \geq 0$  arising from the disorder of the alloys. Wang *et al.* [35], who studied  $\text{Zn}_{1-x}\text{Mn}_x\text{O}$ , have observed that the substitutional disorder can introduce changes in the spectral line position, linewidth, and asymmetry of the first-order  $E_2$  (high) phonon mode. However, there are no reports to our knowledge on compositional disorder related to the line shape of  $E_2$  phonons in  $\text{Mg}_x\text{Zn}_{1-x}\text{O}$  systems. Here, we present the first step to provide a detailed investigation with the SC model on the influence of the first-order Raman spectra in  $\text{Mg}_x\text{Zn}_{1-x}\text{O}$  submicropowders, concentrating on the  $E_2$  (high) mode.

In this section, we report on the preparation of  $\text{Mg}_x\text{Zn}_{1-x}\text{O}$  submicropowders on sapphire substrates using a sol-gel method. By adjusting the Mg compositions within the range of  $0 \leq x \leq 0.14$ , obvious blueshift in the absorption and PL spectra

were observed. Additionally, the broadening and asymmetry of the  $E_2$  (high) spectral line by using micro-Raman spectroscopy shows good agreement with the modified SC model that is based on the finite correlation length of a propagating phonon, due to the alloy potential fluctuations (APFs) and grain size distribution (GSD).

#### 4.2.1 Morphology and bandgap modulation

Figure 4-5 presents an SEM image of the powders; the average crystallite size is  $\sim 150$  nm, which does not reveal a quantum size effect (the Bohr radius of excitons in ZnO  $\sim 2.34$  nm [36,37]).

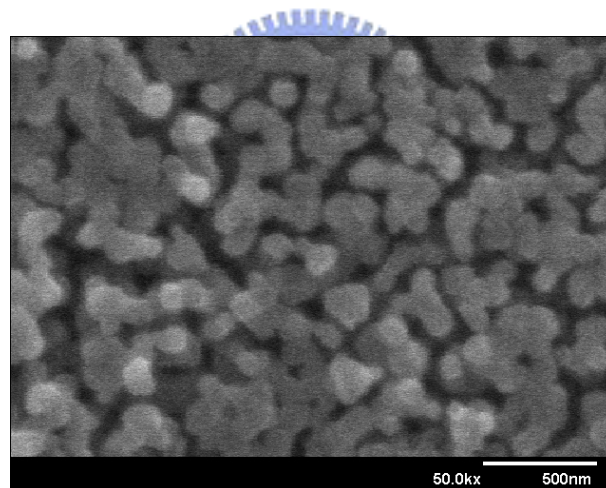


Fig. 4-5 The SEM image of the 10.9% Mg sample.

Shown in figure 4-6 are the PL and absorption spectra taken at RT of five annealed samples having volume ratios of MgO/ZnO equal to 0, 6, 10, 20, and 40%, respectively. All of the PL spectra were dominated by highly efficient NBE emission, which originates from free-exciton emission and its replicas.[5,10,11] The luminescence shows a Stokes shift to the lower-energy side of the absorption edge, which is frequently familiar in alloy semiconductors, where carriers feel different

potentials depending on the local concentration or arrangement of the substituting elements. This effect is larger in ZnO than in III–V materials, because the Bohr radius of the exciton in ZnO is smaller and the exciton is more sensitive to local inhomogeneity.[38] Moreover, the excitonic transition energy exhibits a blueshift of  $\sim 0.24$  eV as the volume ratio of MgO/ZnO increases from 0 to 40%. Similar indications can be seen clearly in the absorption spectra, showing a blueshift from 3.33 to 3.56 eV with increasing MgO content. Namely, Mg doping causes a band-gap enlargement of  $\sim 240$  meV.

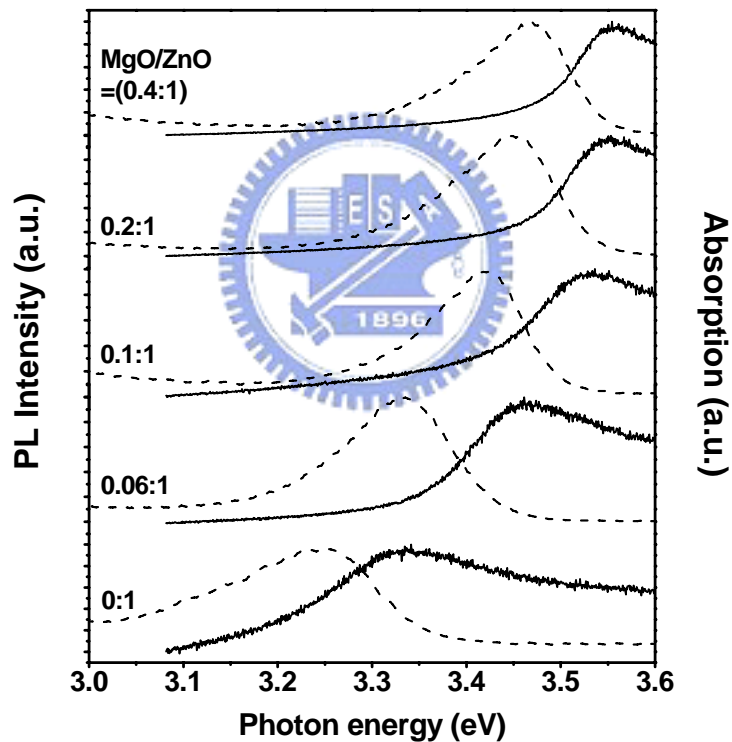


Fig. 4-6 Photoluminescence (solid curves) and absorption spectra (dashed curves) of  $Mg_xZn_{1-x}O$  alloys for different MgO/ZnO volume ratios.

Based on the formula (4.1):  $E(Mg_xZn_{1-x}O) = E(ZnO) + 1.64*x$  (eV), where  $E(Mg_xZn_{1-x}O)$  and  $E(ZnO)$  are the NBE emission peak positions of  $Mg_xZn_{1-x}O$  and ZnO, respectively. The Mg contents in each of our five alloys, with volume ratios of

MgO/ZnO equal to 0, 6, 10, 20, and 40%, were calculated to be 0, 6, 11, 13, and 14%, respectively. Figure 4-7 illustrates the evaluated Mg content of the submicropowders as a function of the volume ratio of MgO/ZnO. The result reveals that MgO has a solubility limit of above 10% in ZnO, in accordance with the present synthesized approach. This tendency closely coincides with that reported for  $Mg_xZn_{1-x}O$  fabricated by a solution-based route, in which MgO did not completely dissolve with ZnO for  $x > 0.1$ . [39] Therefore, the UV emission and absorption exhibits a progressive blueshift with initially increasing MgO content until  $x = 0.1$  or MgO/ZnO(= 0.1:1), demonstrating that  $Mg^{2+}$  is incorporated into the ZnO lattice and occupies the lattice sites of  $Zn^{2+}$ ; thereafter, it tends to slowly blueshift with increasing MgO content, which implies that  $Mg^{2+}$  is no longer completely incorporated into the ZnO lattice.

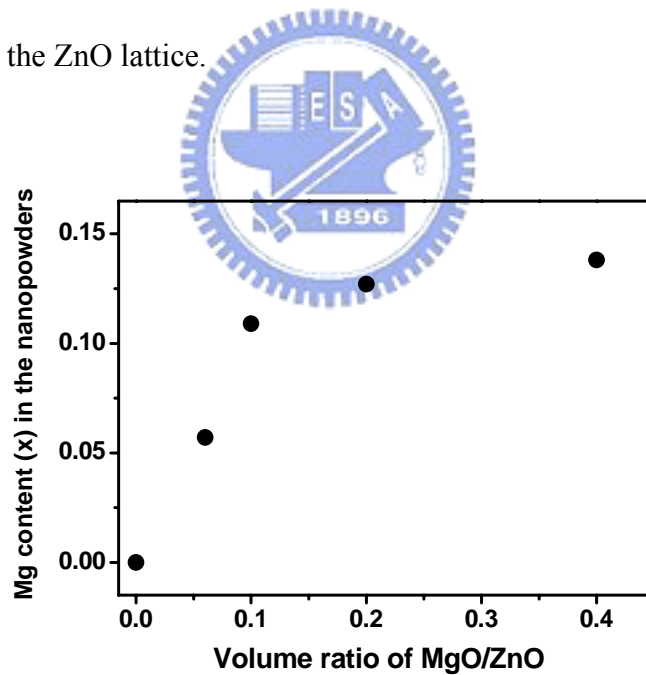


Fig. 4-7 The calculated Mg content in the  $Mg_xZn_{1-x}O$  submicropowders as a function of the MgO/ZnO volume ratio.

#### 4.2.2 Raman spectra analysis

To investigate the influence of Mg doping on the microscopic structures and the

vibrational properties, the micro-Raman spectra of the five samples were measured in a backscattering configuration with a fixed laser spot of about  $2 \mu\text{m}^2$ , as shown in Fig. 4-8 with the inverse  $x$ -sequence compared to that in Fig. 4-6. We found the spectral peaks at 438, and  $584 \text{ cm}^{-1}$  of pure ZnO submicropowders which originate from  $E_2$  (high) and  $E_1$  (LO), respectively. The assignments of the Raman peaks have been reported previously.[19-21] Furthermore, it is interesting to note that the line shape of the  $E_2$ (high) phonon at around  $438 \text{ cm}^{-1}$  depends considerably on the Mg incorporation.

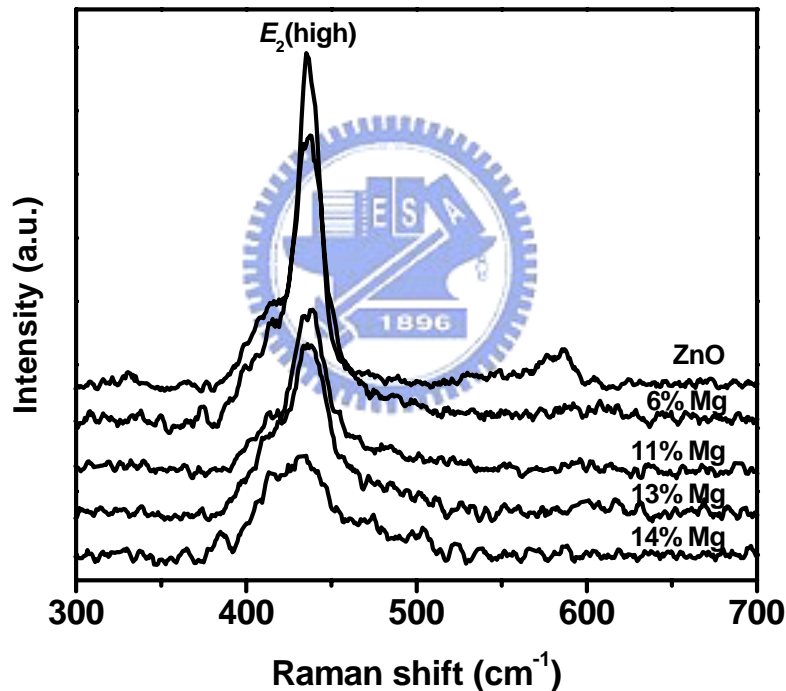


Fig. 4-8 Micro-Raman spectra of the  $\text{Mg}_x\text{Zn}_{1-x}\text{O}$  submicropowders with various Mg contents.

In alloy semiconductors, the phonons can be spatially confined, owing to either the potential fluctuations of the alloy disorder or finite crystalline, which gives rise to a relaxation of the  $q = 0$  selection rule in Raman scattering.[21-23] Therefore, the spatial correlation length of phonon in alloys becomes finite. The localized phonon

mode will lead to the shift and asymmetric broadening of the Raman line shape. Several groups [35,1,24,26] have found these phenomena in ZnO system doped with N, Mn, and Co elements.

The spatial phonon confinement could arise from APFs, as  $\text{Mg}^{2+}$  random substitution induces microscopic structural disorder in the periodic zinc atomic sublattice and breaks the translational symmetry. Besides, Islam *et al.* [40] and Lin *et al.* [41] proposed that the crystallite size distribution could affect the shifts of Raman frequencies and line shapes as well in Si and ZnO nanostructures. Therefore, they modified the Raman spectral intensity expression of the SC model by introducing a Gaussian crystallite size distribution (CSD) of an ensemble of spherical crystallites with mean crystallite size  $L_o$  and standard deviation  $\sigma$ . It can be written as

$$I(\omega) \propto \int_0^1 \frac{f(q)q^2 \exp(-q^2 L_o^2 / 4) dq}{[\omega - \omega(q)]^2 + (\Gamma / 2)^2} \quad (4.3),$$

where  $q$  is presented in units of  $2\pi/a$ ,  $a$  is the lattice constant,  $\omega(q)$  is the phonon dispersion relation,  $\Gamma$  is the linewidth of the  $E_2$  (high) phonon in the bulk ZnO, and  $f(q) = 1/\sqrt{1+q^2\sigma^2/2}$  is the characteristics of the CSD. Setting  $L_o$  and  $\sigma$  as adjustable parameters to fit with the experimental data, we calculated normalized Raman profiles of  $\text{Mg}_x\text{Zn}_{1-x}\text{O}$  submicropowders to depict the Raman line-shapes of the  $E_2$  (high) band; they are plotted in Fig. 4-9. The solid line represents the theoretical fits of the modified SC model, and the open dots are the experimental data. The  $L_o$  values decrease with increasing Mg composition, corresponding to 17, 13.5, 12.5 nm, and 9 nm for  $x \sim 6, 11, 13,$  and  $14\%$ , respectively; nevertheless, the changes of  $\sigma$  and asymmetry  $\Gamma_a/\Gamma_b$  are reversed.

It is understandable that further  $\text{Mg}^{2+}$  incorporated into the ZnO lattice results in the increment of microscopic substitutional disorder, and hence enhances the standard

deviation  $\sigma$  and asymmetrical line shape ( $\Gamma_a > \Gamma_b$ ). In  $\text{Mg}_x\text{Zn}_{1-x}\text{O}$  alloy semiconductors, the correlation length  $L_o$  of  $E_2$  (high) phonon can be interpreted as the average size of the localized regions [23]; thus, the phonon-extended region becomes smaller with increasing Mg content. Accordingly, the localized regions stand for microstructural geometries resulting from sublattice disorder, microcrystallite size or structural damage.[22] Similarly, the Raman spectral position and linewidth  $\Delta\tau$  can also be obtained by the fitting the spectral intensity using the modified spatial correlation mode, in which the  $E_2$  (high) phonon lines are slightly redshifted and remarkably broadened from 15.2 to 40  $\text{cm}^{-1}$  (full width at the half maximum, FWHM) as the Mg concentration in the  $\text{Mg}_x\text{Zn}_{1-x}\text{O}$  nanopowders is increased from  $x = 0$  to 0.14.

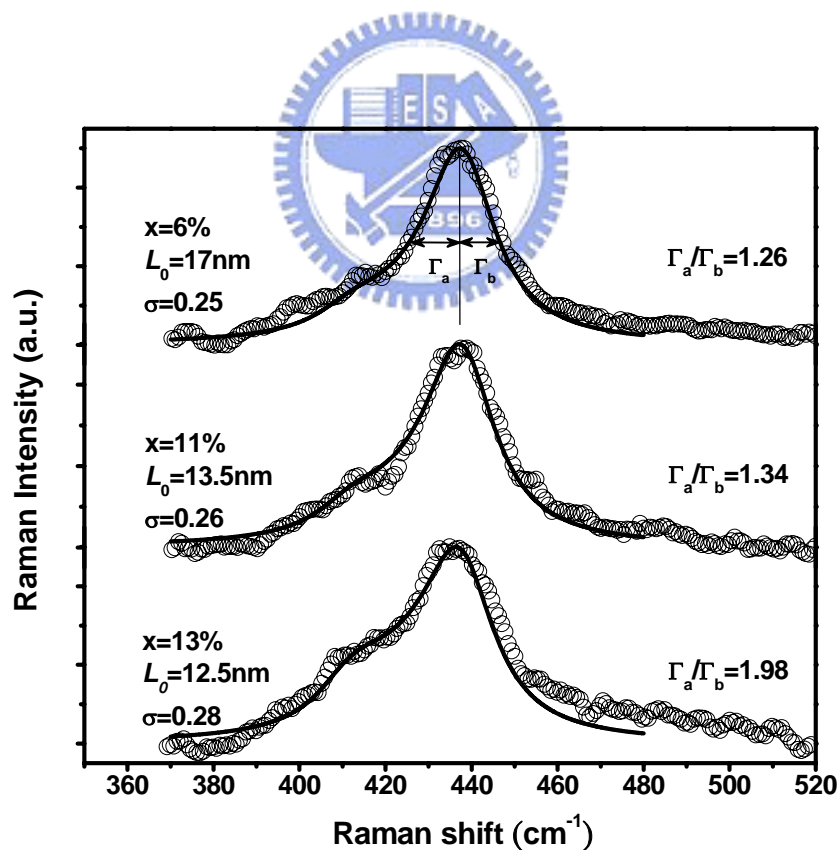


Fig. 4-9 Experimental and calculated line shapes of the  $E_2$  (high) band for  $\text{Mg}_x\text{Zn}_{1-x}\text{O}$  submicropowders with  $x = 6\%$ ,  $11\%$ , and  $13\%$ . The corresponding correlation length  $L_o$ , standard deviation  $\sigma$  and asymmetric broadening  $\Gamma_a/\Gamma_b$  are also labeled.

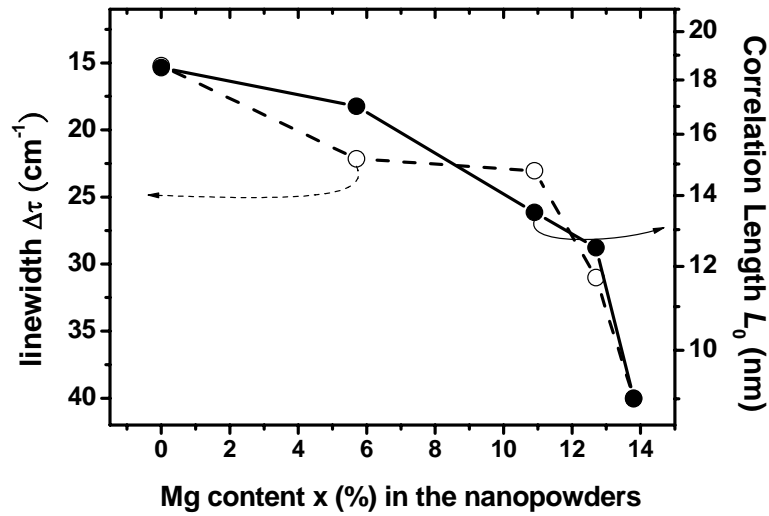


Fig. 4-10 Linewidth  $\Delta\tau$  and correlation length  $L_0$  of  $E_2$  (high) phonon as a function of Mg concentration.

Figure 4-10 reveals that the  $E_2$  (high) phonon linewidth  $\Delta\tau$  and the correlation length  $L_0$  are strongly correlated with the Mg content and vary drastically above  $x \sim 0.1$ . As also revealed in figure 4-7, the actual dopant of Mg above  $x \sim 0.1$  was out of proportion to the volume ratio of MgO/ZnO. Hence, instead of being incorporated into the ZnO lattice, the excess  $Mg^{2+}$  could form MgO clusters surrounding the crystalline MgZnO, which leads to a decrease in the grain size. Namely, the spherical-shape particles of  $\sim 150$  nm, as observed in SEM, are polycrystals formed by the agglomeration of much smaller crystalline subcrystals similar to those shown in the TEM images of Cheng *et al.* [42]. Note that there is no significant blueshift of absorption and NBE due to the quantum size effect for crystal size larger than 7.4 nm [37]; hence, the blueshift of our MgZnO submicropowders is still dominated by the Mg incorporation. Therefore, the  $L_0$  and  $\sigma$  values are appropriate parameters accounting for the disorder due to APFs and GSD of  $Mg_xZn_{1-x}O$  alloys. Consequently, we would suggest that the APFs result in the change of the grain size



with Mg substitution; for  $x > 0.1$ , the grain size diminishes as a result of the random distribution of aggregated  $\text{Mg}^{2+}$  ions in ZnO crystal lattice to form MgO clusters or nanocrystals, which partition a larger MgZnO crystal (e.g.,  $\sim 17\text{--}13.5$  nm) into subcrystals ( $\leq 9$  nm).

We have synthesized  $\text{Mg}_x\text{Zn}_{1-x}\text{O}$  submicropowders with various Mg contents of  $0 \leq x \leq 0.14$  by the sol-gel method. The room-temperature NBE photoluminescence and absorption spectra are shown to be tuned by  $\sim 0.24$  eV towards the UV range upon more Mg substitution. In Raman-scattering studies, the microscopic nature of the substitutional disorder is discussed by analyzing the compositional dependence of the  $E_2$  (high) phonon mode in  $\text{Mg}_x\text{Zn}_{1-x}\text{O}$  alloy. It is shown that the Raman spectral broadening and asymmetry induced by the APFs can be quantitatively explained in terms of the modified SC model, considering GSD. With increasing Mg concentration, the APFs leads to a decrease in grain size, which arose from the surplus  $\text{Mg}^{2+}$  that could form MgO clusters surrounding the MgZnO crystalline.

### 4.3 Summary

In this work, the Mg content in  $\text{Mg}_x\text{Zn}_{1-x}\text{O}$  alloy determined by X-ray diffraction and photoluminescence shows a good coincidence. The blueshift of near-band-edge emission and excitonic absorption along with the observation of Mg-related Raman vibration indicate that  $\text{Zn}^{2+}$  ions are successfully substituted by  $\text{Mg}^{2+}$  ions in ZnO:Mg nanostructures. In Raman-scattering studies, two additional bands around 383 and  $510\text{ cm}^{-1}$  are presumably attributed to the Mg-related vibrational modes except the host phonons of ZnO. The changes in Raman spectral linewidth and the asymmetry of the  $E_2$  (high) mode for various Mg contents can be well described by a modified spatial correlation model that considers grain size distribution. With increasing Mg

concentration, the alloy potential fluctuations lead to a decrease in the grain size, which is induced by the surplus  $\text{Mg}^{2+}$  that could form MgO clusters surrounding the MgZnO crystalline.

We have investigated the influence of Mg incorporation on the lattice dynamics of ZnO and found that the spatial phonon confinement played the critical part in alloy semiconductors. However, due to inhomogeneous linewidth broadening of excitons, the splitting of A and B excitons and donor-bound exciton can still not be resolved in the present work. Therefore, desirable characteristics that need to be achieved in MgZnO systems include: (1) the spectrally resolved fine structure of the exciton states (i.e., the A and B excitons); (2) the observation of phonons acted on exciton-related recombination process; and (3) the observation of spectroscopic signatures associated with various exciton transitions under different temperature and excitation power. In the following chapter we will concentrate on these aspects. The detailed information on interactions between excitons and acoustic phonons, LO phonons, free carriers, and other excitons will be extracted from the relevant optical spectra under various temperature and excitation power.

## References

- [1] A. Kaschner, U. Haboeck, M. Strassburg, G. Kaczmarczyk, A. Hoffmann, C. Thomsen, A. Zeuner, H. R. Alves, D. M. Hoffmann, and B. K. Meyer, *Appl. Phys. Lett.* **80**, 1909 (2002).
- [2] C. Bundesmann, N. Ashkenov, M. Schubert, D. Spemann, T. Butz, E. M. Kaidashev, M. Lorenz, and M. Grundmann, *Appl. Phys. Lett.* **83**, 1974 (2003).
- [3] F. J. Manjon, B. Mari, J. Serrano, and A. H. Romero, *J. Appl. Phys.* **97**, 053516 (2005).
- [4] J. Serrano, A. H. Romero, F. J. Manjon, R. Lauck, M. Cardona, and A. Rubio, *Phys. Rev. B* **69**, 094306 (2004).
- [5] H. C. Hsu, Y. K. Tseng, H. M. Chang, J. H. Kuo, W. F. Hsieh, *J. Crystal Growth* **261**, 520 (2004).
- [6] H. C. Hsu, C. Y. Wu, H. M. Cheng, and W. F. Hsieh, *Appl. Phys. Lett.* **89**, 013101 (2006).
- [7] A. Ohtomo, M. Kawasaki, T. Koida, K. Masubuchi, H. Koinuma, Y. Sakurai, Y. Yoshida, T. Yasuda, and Y. Segawa, *Appl. Phys. Lett.* **72**, 2466 (1998).
- [8] P. Bhattacharya, Rasmi R. Das, and R. S. Katiyar, *Appl. Phys. Lett.* **83**, 2010 (2003).
- [9] W. Q. Peng, S. C. Qu, G. W. Cong, and Z. G. Wang, *Appl. Phys. Lett.* **88**, 101902 (2006).
- [10] B. P. Zhang, N. T. Binh, Y. Segawa, Y. Kashiwaba, and K. Haga, *Appl. Phys. Lett.* **84**, 586 (2004).
- [11] H. C. Hsu, C. S. Cheng, C. C. Chang, S. Yang, C. S. Chang, and W. F. Hsieh, *Nanotechnology* **16**, 297 (2005).
- [12] X. L. Wu, G. G. Siu, C. L. Fu, and H. C. Ong, *Appl. Phys. Lett.* **78**, 2285 (2001).
- [13] B. X. Lin, Z. X. Fu, and Y. B. Jia, *Appl. Phys. Lett.* **79**, 943 (2001).

- [14] K. Vanheusden, W. L. Warren, C. H. Seager, D. R. Tallant, J. A. Voigt, B. E. Gnade, *J. Appl. Phys.* **79**, 7983 (1996).
- [15] S. A. Studenikin, N. Golego, M. Cocivera, *J. Appl. Phys.* **84**, 2287 (1998).
- [16] M. Lorenz, E. M. Kaidashev, A. Rahm, Th. Nobis, J. Lenzner, G. Wagner, D. Spemann, H. Hochmuth, and M. Grundmann, *Appl. Phys. Lett.* **86**, 143113 (2005).
- [17] J. F. Scott, *Phys. Rev. B* **2**, 1209 (1970).
- [18] T. C. Damen, S. P. S. Porto, and B. Tell, *Phys. Rev.* **142**, 570 (1966).
- [19] R. P. Wang, G. Xu and P. Jin, *Phys. Rev. B* **69**, 113303 (2004).
- [20] S. Chen, Y. Liu, C. Shao, R. Mu, Y. Lu, J. Zhang, D. Shen, and X. Fan, *Adv. Mater.* **17**, 586 (2005).
- [21] Y. J. Xing, Z. H. Xi, Z. Q. Xue, X. D. Zhang, and J. H. Song, R. M. Wang, J. Xu, Y. Song, S. L. Zhang, and D. P. Yu, *Appl. Phys. Letter.* **83**, 1689 (2003).
- [22] P. Parayanthal and F. H. Pollak, *Phys. Rev. Lett.* **52**, 1822 (1984).
- [23] L. Y. Lin, C. W. Chang, W. H. Chen, Y. F. Chen, S. P. Guo, and M. C. Tamargo, *Phys. Rev. B* **69**, 075204 (2004).
- [24] G. Du, Y. Ma, Y. Zhang and T. Yang, *Appl. Phys. Lett.* **87**, 213103 (2005).
- [25] J. B. Wang, H. M. Zhong, Z. F. Li, and W. Lu, *J. Appl. Phys.* **97**, 086105 (2005).
- [26] H. Y. Xu, Y. C. Liu, C. S. Xu, C. L. Shao, and R. Mu, *J. Chem. Phys.* **124**, 074707 (2006).
- [27] B. C. Cheng, Y. H. Xiao, G. S. Wu, and L. D. Zhang, *Appl. Phys. Lett.* **84**, 416 (2004).
- [28] L. W. Yang, X. L. Wu, G. S. Huang, T. Qiu, and Y. M. Yang, *J. Appl. Phys.* **97**, 014308 (2005).
- [29] A. Kaschner, H. Siegle, G. Kaczmarczyk, M. Straßburg, A. Hoffmann, C. Thomsen, U. Birkle, S. Einfeldt, and D. Hommel, *Appl. Phys. Letter.* **74**, 3281

(1999).

- [30] H. Harima, *J. Phys. : Condens. Matter* **16**, S5653 (2004).
- [31] B. H. Bairamov, A. Heinrich, G. Irmer, V. V. Toporov, and E. Ziegler, *Phys. Status Solidi B* **119**, 227 (1983).
- [32] H. Richter, Z. P. Wang, and L. Ley, *Solid state Commun.* **39**, 625 (1981).
- [33] I. H. Campbell and P. M. Fauchet, *ibid.* **58**, 739 (1986).
- [34] L. Bergman, M. D. Bremser, W. G. Perry, R. F. Davis, M. Dutta, and R. J. Nemanich, *Appl. Phys. Lett.* **71**, 2157 (1997).
- [35] J. B. Wang, H. M. Zhong, Z. F. Li, and W. Lu, *J. Appl. Phys.* **97**, 086105 (2005).
- [36] R. T. Senger, and K. K. Bajaj, *Phys. Rev. B* **68**, 045313 (2003).
- [37] K. F. Lin, H. M. Cheng, H. C. Hsu, L. J. Lin, and W. F. Hsieh, *Chem. Phys. Lett.* **409**, 208 (2005).
- [38] R. Zimmermann, *J. Crystal Growth* **101**, 346 (1990).
- [39] M. S. Tomar, R. Melgarejo, P. S. Dobal, and R. S. Katiyar, *J. Mater. Res.* **16**, 903 (2001).
- [40] M. N. Islam, A. Pradhan, and S. Kumar, *J. Appl. Phys.* **98**, 024309 (2005).
- [41] K. F. Lin, H. M. Cheng, H. C. Hsu, and W. F. Hsieh, *Appl. Phys. Lett.* **88**, 263117 (2006).
- [42] H. M. Cheng, K. F. Lin, H. C. Hsu, C. J. Lin, L. J. Lin, and W. F. Hsieh, *J. Phys. Chem. B* **109**, 18385 (2005).

## Chapter 5 Acoustic and optical phonon assisted formation of biexcitons

Since the biexciton binding energy is large, 12-20 meV [1-6], in particular, it can be increased to a level comparable to the thermal energy at room temperature in quantum confined structures. Lasing based on biexcitons has been shown to have much lower threshold than that due to exciton-exciton scattering.[7] Recently, the low temperature photoluminescence (PL) of ZnO materials associated with various exciton transitions, especially biexciton recombination, have been investigated by several research groups.[8-13] For example, Yamamoto *et al.* [9] has observed biexciton emission in ZnO thin films grown by plasma-enhanced molecular-beam epitaxy and indicated the biexciton intensity is proportional to the 1.5th power of the excitation density ( $I_{ex}^\alpha$  with  $\alpha = 1.5$ ). Kim *et al.* [12] have synthesized ZnO nanowires by metalorganic chemical vapor deposition and observed biexciton luminescence with  $\alpha = 1.34$  at  $T = 77$  K. The reduction in the exponent was proposed being attributed to the biexcitons are scattered and annihilated by excitons, other biexcitons, and bound excitons.[9,12]

Using the temperature- and excitation power-dependent PL, in this chapter, we will present a detailed discussion on the formation of biexciton assisted by acoustic and optical phonon scattering in ZnO powders prepared by sol-gel method. Surprisingly, other than observed  $\alpha = 1.86$  at  $T = 80$  K, we observed significant reduction in the exponent of excitation intensity for biexciton at  $T = 10$  and  $40$  K. In addition, the quenching of the biexciton PL-intensity may be a result of multi-exciton scattering via increasing densities of excitons.

## 5.1 Morphology and temperature-dependent photoluminescence

Figure 5-1 shows an SEM image of the ZnO powders, which presents an average crystallite size of  $\sim 1 \mu\text{m}$  that does not reveal quantum size effect (Bohr radius of exciton in ZnO is  $\sim 2.34 \text{ nm}$ [14,15]).

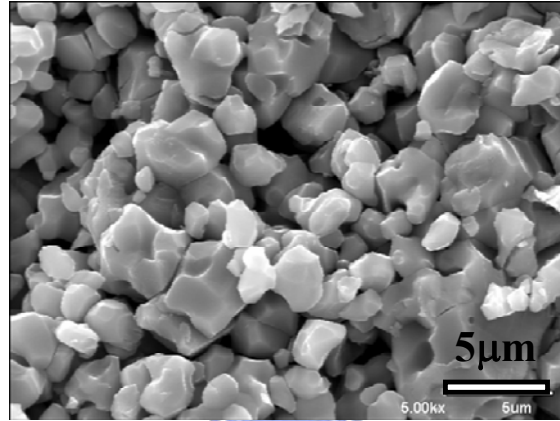


Fig. 5-1 The SEM image of the ZnO powders.

The near band-edge (NBE) emissions of the sample measured at various temperatures are shown in Fig. 5-2. At  $T = 15 \text{ K}$ , the most intense PL emission line at 3.363 eV is attributed to the exciton bound to neutral donor (denoted by  $D^0X$ ). On the high-energy side of the  $D^0X$  line, the A-free exciton emission (denoted by  $FX_A^{n=1}$ ) is observed at 3.373 eV. There are two weak humps positioned at 3.388 and 3.419 eV to the even higher energy. Based on the reported energy separation of A- and B-free excitons ( $\sim 9\text{-}15 \text{ meV}$ ) [16-18], we assigned the emission centered at 3.388 eV to the B-exciton transition, which is about 15 meV apart from the A-exciton; and assigned the other one hump at 3.419 eV to the first excited state  $FX_A^{n=2}$  of A-exciton ( $\sim 45 \text{ meV}$  to the  $FX_A^{n=1}$  state [19]). On the low-energy side of the  $D^0X$  line, the peak at 3.358 eV is attributed to biexciton (labeled BX). The energy spacing between BX and  $FX_A^{n=1}$  emission is 15 meV, which is in agreement with the

previously reported values [8-13]. Besides the broad line at the lower energy shoulder around 3.308 eV labeled as P, we also found several longitudinal optical (LO)-phonon replicas separated by a constant interval of 71-73 meV. The P line can be resolved into two-electron satellite [19], donor-to-acceptor pair [10,11], exciton-exciton scattering [9], and 1LO-phonon replica of  $FX_A^{n=1}$  and  $D^0X$ , respectively. With increasing temperature, the intensity of NBE emission decreases, which is partly due to increasing of non-radiative recombination, and the relative intensity of  $FX_A^{n=1}$  increases whereas that of  $D^0X$  decreases and becomes not detectable for  $T > 80$  K. Notice that the BX emission can be traced up to  $\sim 140$  K (12 meV) although A-exciton, B-exciton, and P line finally merge into a broad peak as further increasing temperature.

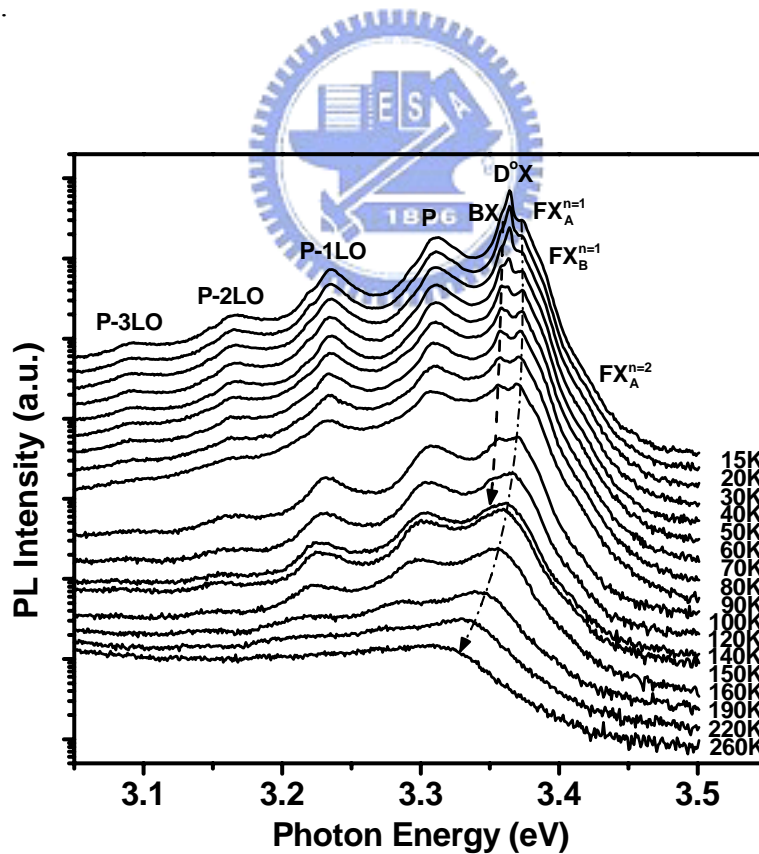


Fig. 5-2 Temperature dependence of PL spectra in ZnO powders. The dashed line on the right-hand side indicates the predicted energy at RT. The dashed line on the left-hand side guides the biexciton emission up to 140 K.



## 5.2 Excitation-power-dependent photoluminescence

Figure 5-3 and Figure 5-4 show the dependence of the PL spectra on the excitation power investigated at 10 and 80 K, respectively. At  $T = 10$  K, the lowest curve (2 mW excitation) presents two peaks at the lower energy side of the BX peak which are located within the above-mentioned P line, denoted as  $P_2$  and  $P_\infty$ , which originate from inelastic scattering between excitons [20]. As a result of such scattering, one exciton is scattered into one of the higher states ( $n = 2, 3, 4, \dots, \infty$ ), while the other exciton loses its kinetic energy to occupy the lower polariton branch, which is roughly located at 3.326 eV and 3.312 eV for its counterpart exciton being scattered to  $n = 2$  and  $n = \infty$ , respectively. In addition, the peak due to 1-LO phonon-assisted radiative recombination of  $D^0X$  is observed at 3.295 eV denoted by  $D^0X$ -1LO. These three bands shift toward the lower energy side and finally merge into a broad P line as further increasing the excitation power.

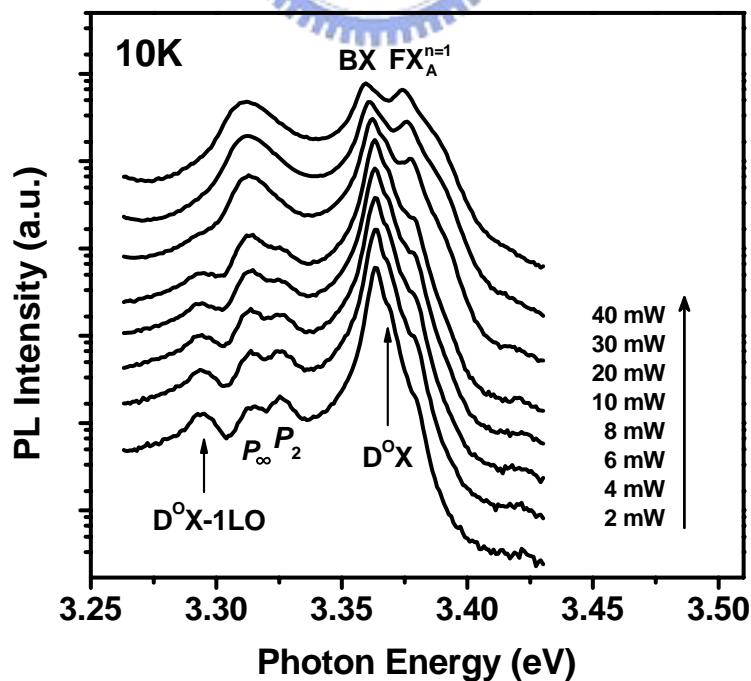


Fig. 5-3 Dependence of the PL spectra on the excitation power measured at 10 K.

For quantitative analysis, the spectral shape of near band edge emission measured at 80 K is decomposed into BX,  $D^0X$ ,  $FX_A^{n=1}$ , and  $FX_B^{n=1}$  by Lorentzian functions. The typical fitting results are shown in the inset of Fig. 5-4 with dashed lines denoting the various emissions and the solid line corresponding to the sum of the theoretical fits, which shows good agreement with the experimental data denoted as the open dots. It is found that the integrated intensity of the free-exciton peak exhibits linear dependence on the excitation power, while that of the biexciton follows a superlinear dependence as  $\sim I_{ex}^{1.86}$  (see Fig. 5-5). The results further support our assignment of  $FX_A^{n=1}$  and BX peaks.

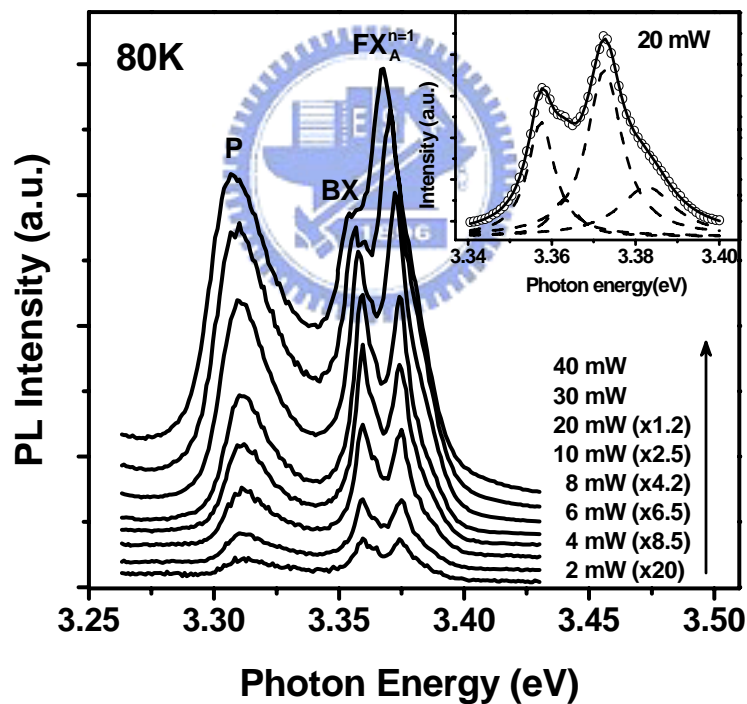


Fig. 5-4 Dependence of PL spectra on excitation power measured at 80 K. The inset shows typically theoretical fit to the PL spectrum for excitation power of 20 mW. Solid lines correspond to the fit and open dots represent the data. The fitted line shapes are also shown separately in dashed lines.

### 5.3 Photoluminescence spectra analysis

In order to further understand the characteristic of the BX line, the PL-integrated intensities of the BX line as a function of excitation power at various temperatures are depicted in Fig. 5-5. Other than at 80 K as discussed above,  $I_{BX}$  is proportional to  $I_{ex}^\alpha$  with  $\alpha \sim 1.86$  but not an ideal exponent of 2. Its possible causes had been proposed to explain this observation: Phillips *et al.* [21] demonstrated that the reduction in the exponent  $\alpha$  is induced in part by the short lifetimes of excitons and biexcitons in direct-band-gap materials. Yamada *et al.* [22] reported the radiative lifetime of biexcitons is shorter than that of excitons, leading to the absence of any quadratic dependence of biexciton density as a function of exciton density.

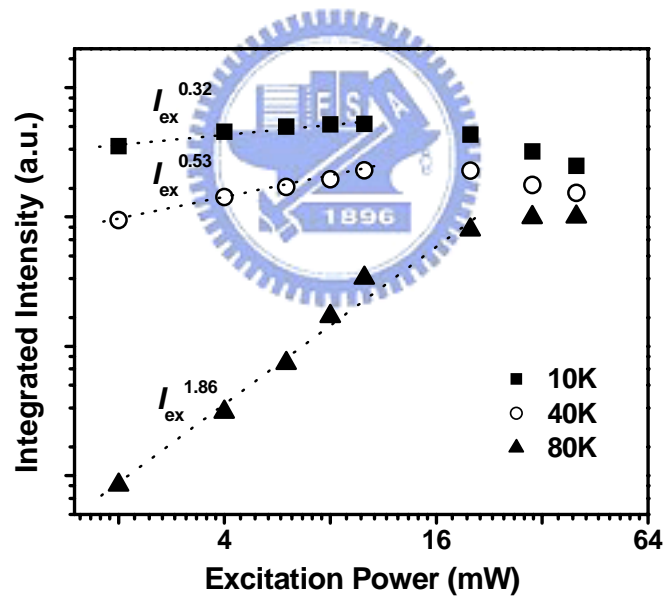


Fig. 5-5 Integrated emission intensity of biexciton as a function of excitation power under various temperatures. The corresponding power dependencies  $I_{BX} \propto I_{ex}^\alpha$  are also labeled.

However, the key issue is why the exponent  $\alpha$  decreases to less than unity ( $\alpha \sim 0.32$  and  $0.53$ ) and the integrated intensity exhibits quenching at high excitation power at 10 and 40 K. These phenomena to our best knowledge have not yet been

reported, although similar quenching effect had appeared in Fig. 4 of Ref. [23] for GaN/AlN quantum dots. We will discuss shortly that the scattering of acoustic and optical phonons could be responsible for different degrees of reducing  $\alpha$  at different measuring temperature, other than the proposed scattered and annihilated by excitons, other biexcitons, and bound excitons [9,12].

As the excitons having kinetic energy less than those of the optical phonons, the only remaining relaxation process, which lowers the kinetic energy of the excitonic gas, is the emission of acoustic phonons.[24] Due to the small energy quanta of the acoustic phonons, the dissipation of the kinetic energy in the excitonic system is rather slow and requires many scattering events before quasi-equilibrium is reached. By elevating the temperature so that the kinetic energy of excitons reaches the energy of the lowest optical phonon, the optical phonon scattering will participate in the exciton relaxation.

We utilized the analysis about emission shift of the free exciton with temperature variation [25]:  $E(T) = E(0) - \lambda / [\exp(\hbar\omega / k_B T_e) - 1]$  to evaluate the effective exciton temperature. By fitting the experimental data (open circles) at bath temperature ( $T_b$ ) of 40 - 100 K for excitation power of 2 mW as the solid line in Fig. 5-6, we obtained the fitting parameters:  $E(0) = 3.379$  eV represents the free exciton emission at  $T = 0$  K (c.f. the reported  $E(0) = 3.379$  eV at  $T = 5$  K [26]),  $\lambda = 24.3$  meV is a proportional coefficient, and  $\hbar\omega = 16.1$  meV is the effective phonon energy, which is close to the lowest optical phonon of 12 meV. The inset of Fig. 5-6 depicts the estimated effective exciton temperature ( $T_e$ ) as a function of excitation power at various  $T_b$ . Notice that the power dependent energy shift corresponds to  $T_e = 32$  to 80 K and 40 to 85 K at  $T_b = 10$  and 40 K. Under these conditions, the exciton kinetic energy or  $T_e$  is inefficient to couple with optical phonons but lowering the

kinetic energy of the excitonic gas by emitting acoustic phonons, and the stochastic approach to the population distribution of the excitons in energy space is justified as in the case of Brownian motion.

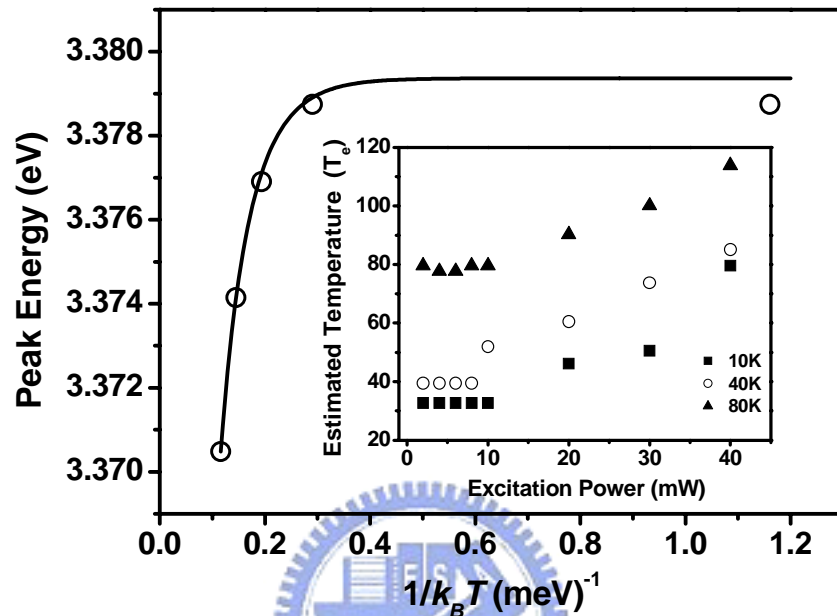


Fig. 5-6 Experimental (open dots) and calculated (solid lines) exciton energies plotted against inverse temperature. The inset shows the dependence of estimated temperatures ( $T_e$ ) on the excitation power under various bath temperatures ( $T_b$ ).

Consequently, the decrease in  $\alpha$  results from the insufficient cooling of excitons by acoustic phonon scattering for bounding exciton pairs to form biexcitons. On the other hand, due to the laser heating,  $T_e$  was elevated above  $T_b$  from 80 to 114 K at  $T_b = 80$  K. When the elevated temperature so as the kinetic energy of excitons approaches to the energy of the lowest optical phonon, near 12 meV in this case, the optical phonon will participate in the exciton relaxation process. The inelastic scattering between excitons with assistance of optical phonons ionizes one of the scattered excitons to  $n = \infty$  state rather than  $n = 2$  state and efficiently cools the other

exciton to the lower polariton branch so that high  $P_\infty$  emission was observed for  $T_b = 80$  K, as shown in Fig. 5-3. Contrarily, without assistance of optical phonon, high  $P_2$  emission was found at  $T_b \leq 40$  K.

## 5.4 Summary

We therefore conclude that high exciton density does not guarantee bounding exciton pairs to form biexcitons, the acoustic phonon scattering is responsible for exciton relaxation at low temperature while optical phonon scattering will participate in at high temperature. The efficient cooling of exciton with assistance of optical phonon scattering allows effectively bounding exciton pairs to form biexcitons; contrarily, the exciton relaxation only via multiple acoustic phonon scattering may not efficiently enough to dissipate the excess kinetic energy of excitons to form biexcitons in turn to reduce the exponent of excitation. Furthermore, multi-exciton scattering via colliding with high density of excitons would result in quenching biexciton luminescence under very high excitation power.

## References

- [1] J. M. Hvam, Phys. Status Solidi B **63**, 511 (1974).
- [2] S. Miyamoto and S. Shionoya, J. Lumin. **12/13**, 563 (1976).
- [3] J. M. Hvam, Solid State Commun. **27**, 1347 (1978).
- [4] H. Schrey and C. Klingshirn, Solid State Commun. **28**, 9 (1978).
- [5] J. M. Hvam, Phys. Status Solidi B **93**, 581 (1979).
- [6] J. M. Hvam, G. Blattner, M. Reuscher, and C. Klingshirn, Phys. Status Solidi B **118**, 179 (1983).
- [7] H. J. Ko, Y. F. Chen, T. Yao, K. Miyajima, A. Yamamoto, and T. Goto, Appl. Phys. Lett. **77**, 537 (2000).
- [8] H. D. Sun, T. Makino, Y. Segawa, M. Kawasaki, A. Ohtomo, K. Tamura, and H. Koinuma, Appl. Phys. Lett. **78**, 3385 (2001).
- [9] A. Yamamoto, K. Miyajima, T. Goto, H. J. Ko, and T. Yao, J. Appl. Phys. **90**, 4973 (2001).
- [10] B. P. Zhang, N. T. Binh, Y. Segawa, K. Wakatsuki, and N. Usami, Appl. Phys. Lett. **83**, 1635 (2003).
- [11] B. P. Zhang, N. T. Binh, Y. Segawa, Y. Kashiwaba, and K. Haga Appl. Phys. Lett. **84**, 586 (2004).
- [12] S. W. Kim, S. Fujita, and S. Fujita, Appl. Phys. Lett. **86**, 153119 (2005).
- [13] X. Q. Zhang, Z. G. Yao, S. H. Huang, I. Suemune, and H. Kumano, J. Appl. Phys. **99**, 063709 (2006).
- [14] R. T. Senger, and K. K. Bajaj, Phys. Rev. B **68**, 045313 (2003).
- [15] K. F. Lin, H. M. Cheng, H. C. Hsu, L. J. Lin, and W. F. Hsieh, Chem. Phys. Lett. **409**, 208 (2005).
- [16] D. C. Reynolds, D. C. Look, B. Jogai, C. W. Litton, G. Cantwell, and W. C. Harsch, Phys. Rev. B **60**, 2340 (1999).

- [17] C. Boemare, T. Monteiro, M. J. Soares, J. G. Guilherme, and E. Alves, *Physica B* **308-310**, 985 (2001).
- [18] D. G. Thomas, *J. Phys. Chem. Solids* **15**, 86 (1960).
- [19] A. Teke, U. Ozgur, S. Dogan, X. Gu, H. Morkoc, B. Nemeth, J. Nause, and H. O. Everitt, *Phys. Rev. B* **70**, 195207 (2004).
- [20] *Semiconductor Optics*, edited by C. F. Klingshirn (Springer, 1997).
- [21] R. T. Phillips, D. J. Lovering, G. J. Denton, and G. W. Smith, *Phys. Rev. B* **45**, 4308 (1992).
- [22] Y. Yamada, T. Mishina, Y. Masumoto, Y. Kawakami, J. Suda, Sz. Fujita, and Sg. Fujita, *Phys. Rev. B* **52**, R2289 (1995).
- [23] S. Kako, K. Hoshino, S. Iwamoto, S. Ishida, and Y. Arakawa, *Appl. Phys. Lett.* **85**, 64 (2004).
- [24] *Excitonic Processes in Solids*, M. Ueta, H. Kanzaki, K. Kobayashi, Y. Toyozawa, and E. Hanamura (Springer, 1984).
- [25] T. Makino, C. H. Chia, N. T. Tuan, Y. Segawa, M. Kawasaki, A. Ohtomo, K. Tamura, and H. Koinuma, *Appl. Phys. Lett.* **76**, 3549 (2000).
- [26] A. Tsukazaki, A. Ohtomo, S. Yoshida, M. Kawasaki, C. H. Chia, T. Makino, Y. Segawa, T. Koida and S. F. Chichibu, and H. Koinuma, *Appl. Phys. Lett.* **83**, 2784 (2003).



## Chapter 6 Reducing exciton–longitudinal optical phonon coupling with increasing Mg incorporation in MgZnO powders

A precise knowledge of the excitonic parameters for  $\text{Mg}_x\text{Zn}_{1-x}\text{O}$  alloys is important because excitons are a sensitive indicator of material quality. Especially the exciton-phonon coupling has significant influence on the optical properties of semiconductors, such as the energy relaxation rate of excited carriers and phonon replicas of excitons in the luminescence spectra. As is well known, polar semiconductors experience a strong Fröhlich interaction that gives rise to exciton-LO-phonon interaction. However, there are few attempts to study the exciton-LO-phonon coupling by photoluminescence (PL) experiments in MgZnO materials. Recently, Wang *et al.* [1] has extracted the exciton-LO-phonon-coupling parameter of laser ablation prepared ZnO nanowires by resonant Raman scattering. It was found that the coupling strength of exciton-LO-phonon ( $\lambda_{\text{EX-LO}}$ ) determined by the ratio of the second- to the first-order Raman scattering cross sections diminishes with decreasing nanowire diameter. A similar observation was also found in ZnO quantum dots.[2] Sun *et al.* [3], who grown ZnO/ZnMgO multiquantum wells by laser-molecular-beam epitaxy, investigated  $\lambda_{\text{EX-LO}}$  by the temperature dependence of the linewidth of the fundamental excitonic peak from optical absorption spectra. The reduction of  $\lambda_{\text{EX-LO}}$  with decreasing the well width was observed, which is consistent with the confinement-induced enhancement of the exciton binding energy ( $E_{\text{XB}}$ ).

In this chapter, the near band-edge (NBE) luminescence properties of  $\text{Mg}_x\text{Zn}_{1-x}\text{O}$

( $0 \leq x \leq 0.05$ ) powders prepared by sol-gel method were comparatively analyzed with those of undoped ZnO powders by temperature-dependent PL. We found that  $E_{XB}$  of Mg-doped ZnO powders raises with increasing Mg substitution. It is inferred that the localization of exciton originating from the compositional fluctuation takes place in  $Mg_xZn_{1-x}O$  alloys. We also investigated  $\lambda_{Ex-LO}$  determined by the exciton peak shift with temperature variation on the basis of a Bose-Einstein expression. A reducing  $\lambda_{Ex-LO}$  was ascribed to increase of  $E_{XB}$  in the  $Mg_xZn_{1-x}O$  powders as the compression of the exciton Bohr radius ( $a_{EB}$ ).

## 6.1 Morphology and temperature-dependent photoluminescence

The average crystallite sizes of  $Mg_xZn_{1-x}O$  and ZnO powders were estimated from the scanning electron microscopy images in Fig. 6-1 and its inset, respectively, to be  $1 \pm 0.5 \mu m$  that does not reveal quantum size effect (Bohr radius of exciton in ZnO is  $\sim 2.34$  nm[4,5]). Accordingly, the exciton behavior was affected mainly by the incorporation of Mg.

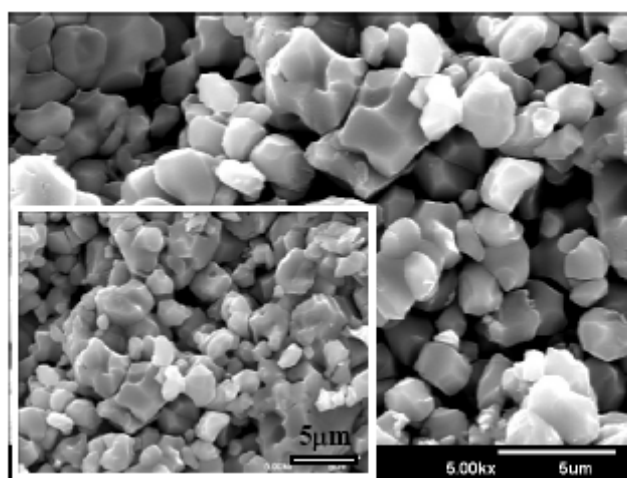


Fig. 6-1 The SEM image of the 5% Mg sample. The inset shows the pure ZnO powders.

The NBE emissions of the ZnO and Mg<sub>0.05</sub>Zn<sub>0.95</sub>O samples measured at various temperatures are shown in Fig. 6-2 and 6-3, respectively. First, we discuss the PL spectra of the undoped sample in order to comparatively assign the PL peaks of the Mg<sub>0.05</sub>Zn<sub>0.95</sub>O powders. At T = 15K (Fig. 6-2), the most intense PL emission line at 3.363 eV is attributed to the exciton bound to neutral donor (denoted by D<sup>0</sup>X). On the high-energy side of the D<sup>0</sup>X line, the A-free exciton emission (denoted by  $FX_A^{n=1}$ ) is observed at 3.373 eV. There are two weak humps positioned at 3.388 and 3.419 eV to the even higher energy. Based on the reported energy separation of A- and B-free excitons (~ 9-15 meV) [6-8], we assigned the emission centered at 3.388 eV to the B exciton transition, which is about 15 meV apart from the A exciton; and the other one hump at 3.419 eV to the first excited state  $FX_A^{n=2}$  (~ 45 meV to the  $FX_A^{n=1}$  state [9]). On the low-energy side of the D<sup>0</sup>X line, the peak at 3.358 eV is attributed to biexciton (labeled BX) based on previous reports.[10-16] Besides the broad line at the lower energy shoulder around 3.308 eV labeled as "P", we also found several LO-phonon replicas separated by a constant interval of 71-73 meV. The P line can be resolved into two-electron satellite [17], donor-to-acceptor pair [12,13], exciton-exciton scattering [11], and 1LO-phonon replica of  $FX_A^{n=1}$  and D<sup>0</sup>X, respectively. With increasing temperature, the relative intensity of  $FX_A^{n=1}$  increases whereas that of D<sup>0</sup>X decreases and becomes not detectable for T > 80 K. This is due to the thermal dissociation of bound exciton into free exciton at higher temperature. As further increasing temperature, the A exciton, B exciton, and P line finally merge into a broad peak. At RT, the exciton peak position at ~ 3.309 eV.

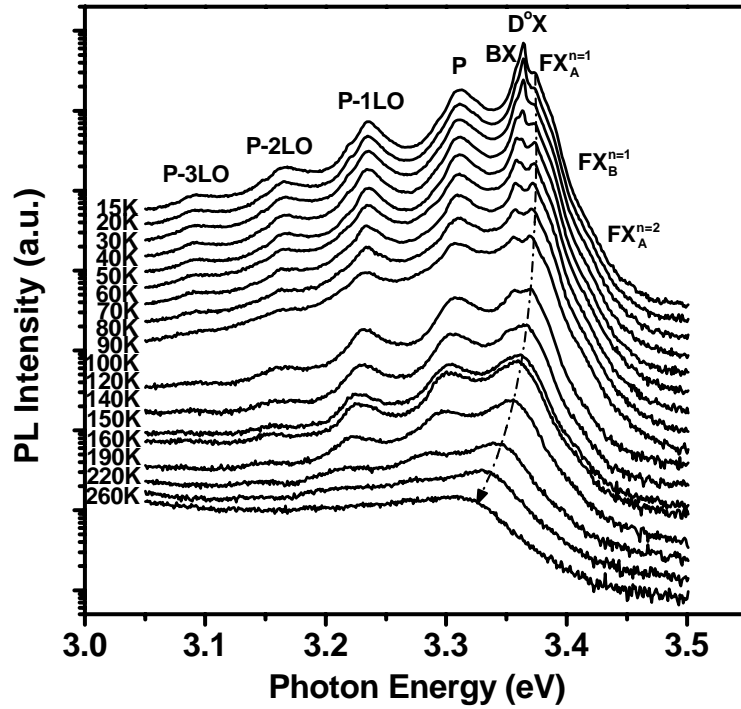


Fig. 6-2 Temperature dependence of PL spectra in ZnO powders. The dashed line indicates the predicted exciton peak position.

The NBE emission of the  $Mg_{0.05}Zn_{0.95}O$  sample was shown in Fig. 6-3; it would evolve from that of the ZnO sample. According to the opposite temperature dependence of the relative emission intensity, the peaks at 3.422 and 3.407 are reasonably assigned to the  $FX_A^{n=1}$  and  $D^{\circ}X$  transitions. The higher energy shoulder at 3.457 eV is related to the B exciton transition, which is 35 meV apart from the A exciton based on the reported theoretical predictions in MgZnO systems [18]. The NBE peak position at RT exhibits a maximum blueshift of  $\sim 74$  meV as 5 at.% Mg was introduced into the ZnO powders. Based on the formula  $E(Mg_xZn_{1-x}O) = E(ZnO) + 1.64 * x$  (eV), the Mg content in the  $Mg_xZn_{1-x}O$  thin films has been determined for  $0 \leq x \leq 0.2$ , grown by pulsed laser deposition.[19] Here,  $E(Mg_xZn_{1-x}O)$  and  $E(ZnO)$  are the NBE emission peak positions of  $Mg_xZn_{1-x}O$  and ZnO, respectively. The calculated Mg contents of our  $Mg_xZn_{1-x}O$  alloys were shown in

Table 6-1, e.g., the molar ratio of Mg/Zn = 5% was estimated to be ~ 4.5%. Therefore, the blueshift of the UV emission demonstrated that the Mg ions had incorporated into the ZnO host lattice.

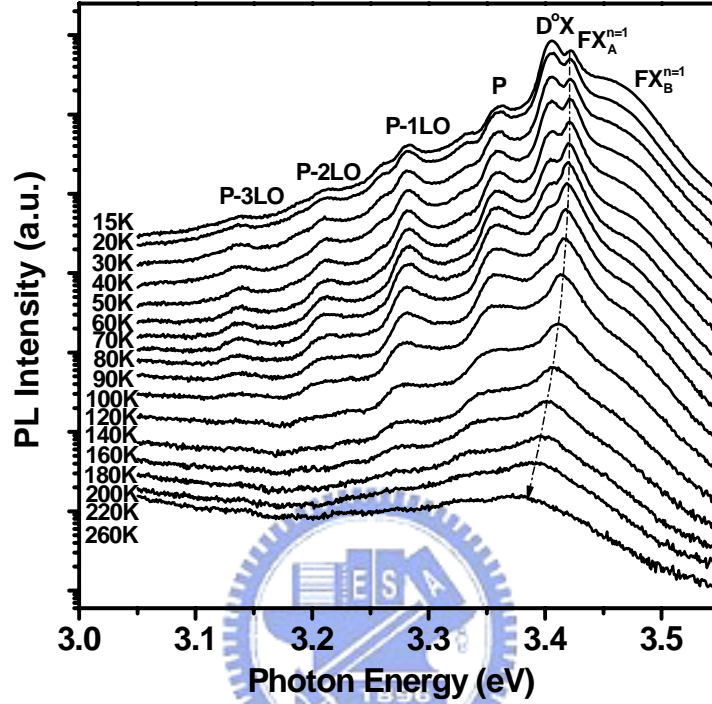


Fig. 6-3 Temperature dependence of PL spectra in  $Mg_{0.05}Zn_{0.95}O$  powders. The dashed line indicates the predicted exciton peak position.

## 6.2 Binding energy

Figure 6-4 and 6-5 show the peak intensity of the  $FX_A^{n=1}$  emission as a function of reciprocal temperature for the undoped and Mg-doped samples, respectively. The data can be described by the equation [20]

$$I = I_o / [1 + a_1 \exp(-E_{a1} / kT) + a_2 \exp(-E_{a2} / kT)], \quad (6.1)$$

where  $E_{ai}$  ( $i = 1, 2$ ) is the activation energy in the thermal quenching process,  $a_1, a_2$  are constants, and  $k$  is the Boltzmann constant. The curve fitting gives rise to two activation energies of about 55 and 11 meV for ZnO powders (Fig. 6-4) and about 73

and 10 meV for  $\text{Mg}_{0.05}\text{Zn}_{0.95}\text{O}$  powders (Fig. 6-5). In regard to the  $E_{a2}$  of  $\sim 10$  meV, Krustok *et al.* [20] have reported that a low  $E_a$  may result from the temperature-dependent capture cross sections of the carriers at the recombination centers, and not from a genuine thermal activation energy. Furthermore,  $E_{a1}$  for ZnO is comparable with  $E_{XB}$ , 60 meV, for ZnO bulk, while that for  $\text{Mg}_{0.05}\text{Zn}_{0.95}\text{O}$  is larger than 60 meV. Table 6-1 clearly shows that the binding energy of  $FX_A^{n=1}$  increases markedly in samples of higher  $x$ . Therefore, it was implied that exciton localization takes place and that the degree of localization increases with increasing  $x$ . The essential origin of the localization is thought to be the spatial fluctuation of the local composition of Mg in the alloys, which results in the spatial fluctuation of the potential energy for the excitons.

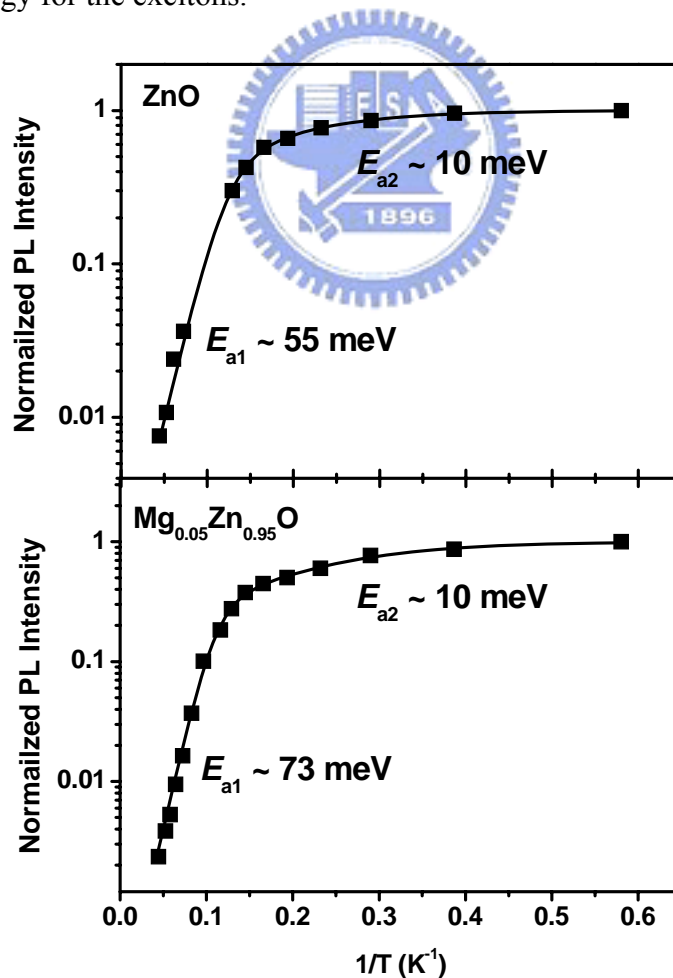


Fig. 6-4 Normalized integrated intensity of ZnO sample as a function of temperature.

Fig. 6-5 Normalized integrated intensity of  $\text{Mg}_{0.05}\text{Zn}_{0.95}\text{O}$  sample as a function of temperature.

### 6.3 Photoluminescence spectra analysis

It is well known the increase of  $E_{XB}$  may result from the decrease of  $a_{EB}$  or effective reduced mass. Due to the electron is more delocalized than the hole in the bulk exciton, the polar lattice experience a net negative charge in the outer regions of the exciton, while it experiences a net positive one in the inner regions. This charge inhomogeneity couples to the polar lattice via the Fröhlich mechanism that leads to reduce  $a_{EB}$  and to reduce the exciton-LO-phonon coupling.[21] Thus, we further deduced the coupling strength of free exciton A with LO phonon from temperature-dependent energy shift of  $FX_A^{n=1}$  as increasing Mg concentration according to the Bose-Einstein expression [22]:

$$E(T) = E(0) - \lambda / [\exp(\hbar\omega_{LO} / k_B T) - 1], \quad (6.2)$$

where  $E(0)$  represents the emission energy of free exciton A at  $T = 0$  K,  $\hbar\omega_{LO} = 72$  meV is the LO phonon energy, and  $\lambda$  is a proportional coefficient which reflects a change in the exciton-LO-phonon interaction. The physical mechanism about exciton-phonon interaction was shown in Fig. 6-6.

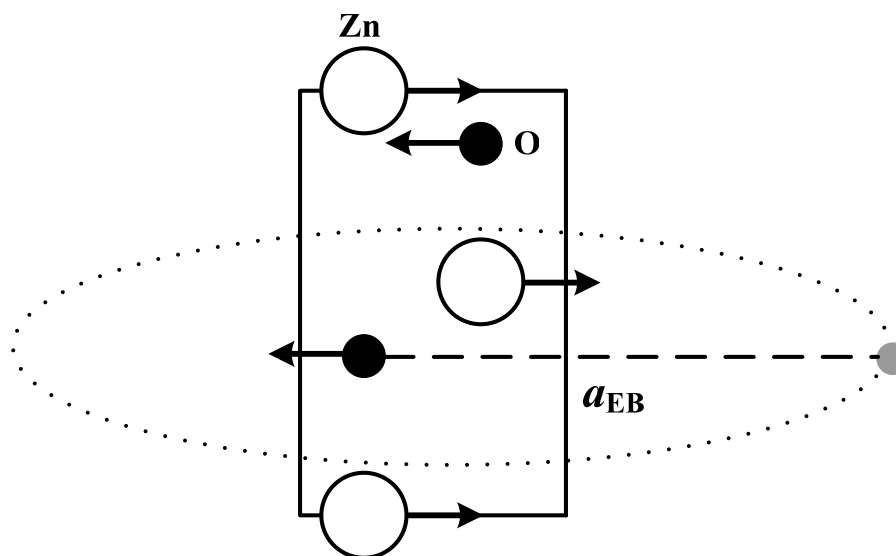


Fig. 6-6 Diagram of exciton-phonon interaction in the unit cell.

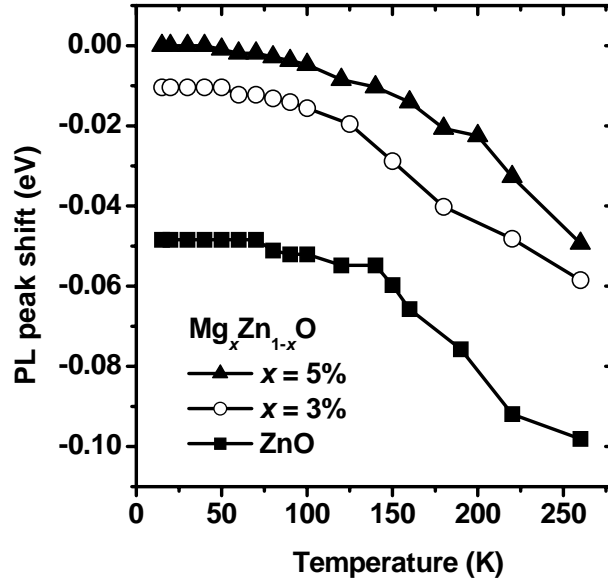


Fig. 6-7 Dependence of PL peak energy positions on temperature for the  $Mg_xZn_{1-x}O$  alloys ( $x = 5\%$ ,  $3\%$ , and zero).

Figure 6-7 depicts the PL-peak energy shift as a function of the temperature with different Mg concentrations. Notice that we had set the PL-peak energy position to zero for  $Mg_{0.05}Zn_{0.95}O$  powders at 15 K. By fitting the experimental data for all the  $Mg_xZn_{1-x}O$  and ZnO powders from  $T = 15$  to 260 K with Eq. (6.2), the exciton-LO-phonon coupling of each  $Mg_xZn_{1-x}O$  sample are compared with ZnO powder by taking the average ratios,  $\lambda_{Mg_xZn_{1-x}O}/\lambda_{ZnO}$ , which are listed in Table 6-1 clearly show decreasing as more Mg incorporation. Even though  $a_{EB}$  and  $\lambda$  are not directly proportional, there is a relation: If  $a_{EB}$  reduces  $\lambda$  will also reduce. Assuming that the Mg-doped ZnO powders have almost the same effective electron and hole masses as the undoped ZnO powders due to a small amount of  $Mg^{2+}$  substitution for  $Zn^{2+}$ , we calculated  $a_{EB}$  from  $E_{XB}$ . The correlation between  $\lambda$  and  $a_{EB}$  normalized to ZnO powders are shown in Fig. 6-8 with open triangles and squares, respectively. Besides, the solid dots are obtained by the modified effective masses, which were corrected from MgZnO electronic band structure using semi-empirical



tight-binding approach  $sp^3$  model [23,24] and virtual-crystal approximation method[25]. Therefore, a contraction of  $a_{EB}$  will make it less polar thereby reducing the coupling to LO phonons. The results show that relaxation by means of LO phonon becomes the less important as the more Mg incorporation. Consequently, we attribute this reducing coupling effect to increase in  $E_{XB}$  with raising Mg mole fraction up to 5% of  $Mg_xZn_{1-x}O$  powders. The reduction of  $\lambda_{EX-LO}$  has to take into account for the  $MgZnO$ -based excitonic device performance in which carrier relaxation to the exciton ground state is a crucial parameter.

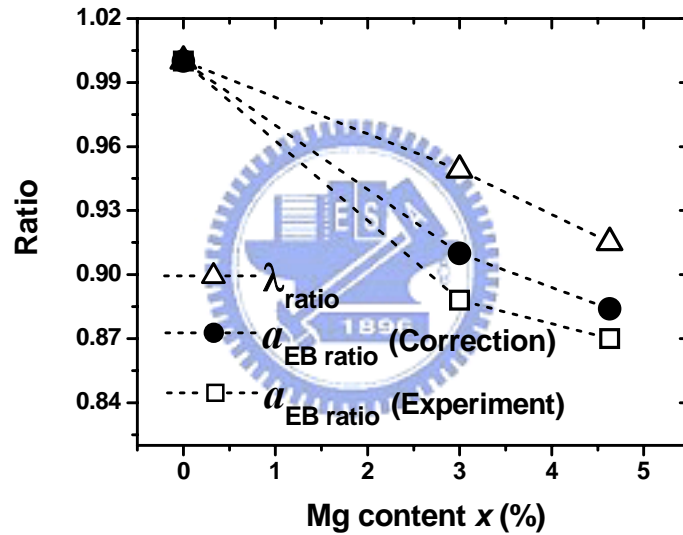


Fig. 6-8 The coupling strength of the exciton-LO-phonon given as the average ratio  $\lambda_{ratio} = \lambda_{Mg_xZn_{1-x}O} / \lambda_{ZnO}$ . For comparison, the diminution of  $a_{EB}$  for experiment and correction is also given as  $a_{EB ratio} = a_{EB Mg_xZn_{1-x}O} / a_{EB ZnO}$ .

Table 6-1 Summary of the results of the temperature-dependent PL characterization.

<b>Samples: Mg<sub>x</sub>Zn<sub>1-x</sub>O</b>	<b>x = 0</b>	<b>x = 3%</b>	<b>x = 5%</b>
<b>Calculated Mg content (%)</b>	<b>0</b>	<b>2.9</b>	<b>4.5</b>
<b>Exciton binding energy (meV)</b>	<b>55 ± 4.7</b>	<b>70 ± 6.7</b>	<b>73 ± 8.4</b>
<b>Exciton-LO-phonon coupling strength</b> $\lambda_{(\text{Mg}_x\text{Zn}_{1-x}\text{O})}/\lambda_{(\text{ZnO})}$	<b>1</b>	<b>0.95</b>	<b>0.91</b>

## 6.4 Summary

The temperature-dependent NBE PL spectra of Mg<sub>x</sub>Zn<sub>1-x</sub>O powders within the range  $0 \leq x \leq 0.05$  were measured from 15 K to RT. The RT excitonic transition energy showed being tuned by  $\sim 74$  meV towards the UV range upon more Mg substitution. We deduced experimentally  $E_{XB}$  showing elevation in powders up to 5% Mg substitution. It is suggested that the localization of excitons, because of the compositional fluctuation, takes place in Mg<sub>x</sub>Zn<sub>1-x</sub>O alloys and that the degree of the localization increases with increasing  $x$ . The reduction of  $\lambda_{\text{Ex-LO}}$  may originate from a diminution in  $a_{\text{EB}}$  making the exciton less polar, which could be explained by the dopant-induced increase of  $E_{XB}$ .

## References

- [1] R. P. Wang, G. Xu, and P. Jin, *Phys. Rev. B* **69**, 113303 (2004).
- [2] H. M. Cheng, K. F. Lin, H. C. Hsu, and W. F. Hsieh, *Appl. Phys. Lett.* **88**, 261909 (2006).
- [3] H. D. Sun, T. Makino, Y. Segawa, M. Kawasaki, A. Ohtomo, K. Tamura, and H. Koinuma, *Appl. Phys. Lett.* **78**, 2464 (2001).
- [4] R. T. Senger, and K. K. Bajaj, *Phys. Rev. B* **68**, 045313 (2003).
- [5] K. F. Lin, H. M. Cheng, H. C. Hsu, L. J. Lin, and W. F. Hsieh, *Chem. Phys. Lett.* **409**, 208 (2005).
- [6] D. C. Reynolds, D. C. Look, B. Jogai, C. W. Litton, G. Cantwell, and W. C. Harsch, *Phys. Rev. B* **60**, 2340 (1999).
- [7] C. Boemare, T. Monteiro, M. J. Soares, J. G. Guilherme, and E. Alves, *Physica B* **308-310**, 985 (2001).
- [8] D. G. Thomas, *J. Phys. Chem. Solids* **15**, 86 (1960).
- [9] A. Teke, U. Ozgur, S. Dogan, X. Gu, H. Morkoc, B. Nemeth, J. Nause, and H. O. Everitt, *Phys. Rev. B* **70**, 195207 (2004).
- [10] H. D. Sun, T. Makino, Y. Segawa, M. Kawasaki, A. Ohtomo, K. Tamura, and H. Koinuma, *Appl. Phys. Lett.* **78**, 3385 (2001).
- [11] A. Yamamoto, K. Miyajima, T. Goto, H. J. Ko, and T. Yao, *J. Appl. Phys.* **90**, 4973 (2001).
- [12] B. P. Zhang, N. T. Binh, Y. Segawa, K. Wakatsuki, and N. Usami, *Appl. Phys. Lett.* **83**, 1635 (2003).
- [13] B. P. Zhang, N. T. Binh, Y. Segawa, Y. Kashiwaba, and K. Haga, *Appl. Phys. Lett.* **84**, 586 (2004).
- [14] S. W. Kim, S. Fujita, and S. Fujita, *Appl. Phys. Lett.* **86**, 153119 (2005).
- [15] X. Q. Zhang, Z. G. Yao, S. H. Huang, I. Suemune, and H. Kumano, *J. Appl.*

- Phys. **99**, 063709 (2006).
- [16] C. J. Pan, K. F. Lin, and W. F. Hsieh, Appl. Phys. Lett. **91**, 111907 (2007).
- [17] A. Teke, U. Ozgur, S. Dogan, X. Gu, H. Morkoc, B. Nemeth, J. Nause, and H. O. Everitt, Phys. Rev. B **70**, 195207 (2004).
- [18] R. Schmidt, B. Rheinlander, M. Schubert, D. Spemann, T. Butz, J. Lenzner, E. M. Kaidashev, M. Lorenz, A. Rahm, H. C. Semmelhack, and M. Grundmann, Appl. Phys. Lett. **82**, 2260 (2003).
- [19] M. Lorenz, E. M. Kaidashev, A. Rahm, Th. Nobis, J. Lenzner, G. Wagner, D. Spemann, H. Hochmuth, and M. Grundmann, Appl. Phys. Lett. **86**, 143113 (2005).
- [20] J. Krustok, H. Collan, and K. Hjelt, J. Appl. Phys. **81**, 1442 (1997).
- [21] J. J. Shiang, S. H. Risbud, and A. P. Alivisatos, J. Chem. Phys. **98**, 8432 (1993).
- [22] T. Makino, C. H. Chia, N. T. Tuan, Y. Segawa, M. Kawasaki, A. Ohtomo, K. Tamura, and H. Koinuma, Appl. Phys. Lett. **76**, 3549 (2000).
- [23] A. Kobayashi, O. F. Sankey, S. M. Volz, and J. D. Dow, Phys. Rev. B **28**, 935 (1983).
- [24] K. F. Lin, C. J. Pan, and W. F. Hsieh, submitted to Appl. Phys. Lett.
- [25] D. W. Jenkins, and J. D. Dow, Phys. Rev. B **39**, 3317 (1989).

## Chapter 7 Conclusion and Prospective

### 7.1 Conclusion

We have synthesized the MgZnO alloys with wurtzite structure for various Mg contents, which can be achieved simply by thermal diffusion and a sol-gel method. The Mg compositions in  $\text{Mg}_x\text{Zn}_{1-x}\text{O}$  alloys were determined roughly by X-ray diffraction and photoluminescence spectroscopy. The relation between the lattice constants and the Mg concentration, i.e., the  $a$ -axis length increases while the  $c$ -axis length decreases with increasing incorporation concentration, usually is common in MgZnO systems. By adjusting the Mg compositions within the range of  $0 \leq x \leq 0.14$ , the blueshift of near-band-edge emission and excitonic absorption demonstrated the band gap modulation of ZnO, achieving a band-gap enlargement of  $\sim 240$  meV at room temperature in present work. The dependence of the lattice parameter and the near-band-edge emission on Mg incorporation indicated that  $\text{Mg}^{2+}$  is incorporated into the ZnO host lattice and occupies the lattice sites of  $\text{Zn}^{2+}$ . Moreover, it is found that MgO has a solubility limit of above 10% in ZnO according to the present prepared approach, which coincides with that reported for  $\text{Mg}_x\text{Zn}_{1-x}\text{O}$  fabricated by a solution-based route.

Due to the differences in the ionic radii of Mg impurity and host ions, when  $\text{Mg}^{2+}$  ions occupy the Zn sites, some new lattice defects are introduced or intrinsic host-lattice defects become activated. As a result, some additional vibrational modes, characteristic of substitution-induced vibrations, appear in the Raman spectra. In addition to the host phonons of ZnO, we found two anomalous modes at 383 and 510  $\text{cm}^{-1}$ , which correlated with the Mg-related lattice vibrations. We suggested that the

383  $\text{cm}^{-1}$  band is likely the local vibrational mode of Mg on substitutional O site in the ZnO lattice, and the 510  $\text{cm}^{-1}$  band is presumably attributed to the host lattice defects.

One of the most important aspects of substitutional semiconductor alloys is the nature of the alloy potential fluctuations (APFs). The APFs destroy translational invariance, an effect that manifests itself as a breakdown of the usual  $q = 0$  Raman selection rule, thus leading to the change of the Raman line shape. In Raman-scattering studies, the microscopic nature of the substitutional disorder is discussed by analyzing the compositional dependence of the  $E_2$  (high) phonon mode in  $\text{Mg}_x\text{Zn}_{1-x}\text{O}$  submicropowders. It is shown that the Raman spectral broadening and asymmetry induced by the APFs can be quantitatively explained in terms of the modified spatial correlation model that considers the grain size distribution. We inferred that the APFs cause a decrease in grain size with increasing Mg concentration. Especially for  $x > 10\%$ , the grain size diminishes as a result of the random distribution of aggregated  $\text{Mg}^{2+}$  ions in ZnO crystal lattice to form MgO clusters or nanocrystals, which partition a larger MgZnO crystal into subcrystals

Additionally, we reported a detailed investigation on the formation of biexciton assisted by acoustic and optical phonon scattering in ZnO powders. Other than the proposed exponent comes near theoretical value of 2, we observed a sublinear dependence on excitation power for biexciton at low temperature ( $\leq 40$  K). It can be considered that the exciton kinetic energy is inefficient to couple with optical phonons but lowering the kinetic energy of the excitonic gas by emitting acoustic phonons. Due to the small energy quanta of the acoustic phonons, the dissipation of the kinetic energy in the excitonic system is rather slow and requires many scattering events before quasi-equilibrium is reached. By elevating the temperature so that the kinetic energy of excitons reaches the energy of the lowest optical phonon, near 12 meV in

this case, the optical phonon will participate in the exciton relaxation process. The efficient cooling of exciton with assistance of optical phonon scattering allows effectively bounding exciton pairs to form biexcitons at high temperature ( $\geq 80$  K). Furthermore, the inelastic scattering between excitons with assistance of optical phonons ionizes one of the scattered excitons to  $n = \infty$  state rather than  $n = 2$  state and efficiently cools the other exciton to the lower polariton branch so that high  $P_\infty$  emission was observed for high temperature. Contrarily, without assistance of optical phonon, high  $P_2$  emission was found at low temperature.

Besides, the interaction between exciton and phonon has significant influence on the optical properties of semiconductors, such as the energy relaxation rate of excited carriers and phonon replicas of excitons in the luminescence spectra. As is well known, polar semiconductors experience a strong Fröhlich interaction that gives rise to exciton-longitudinal optical (LO)-phonon interaction. It is found that the exciton binding energy of  $\text{Mg}_x\text{Zn}_{1-x}\text{O}$  ( $0 \leq x \leq 0.05$ ) powders raises with increasing Mg substitution by fitting the temperature-dependent photoluminescence spectra. It was implied that exciton localization takes place and that the degree of localization increases with increasing  $x$ . The essential origin of the localization is thought to be the spatial fluctuation of the local composition of Mg in the alloys, which results in the spatial fluctuation of the potential energy for the excitons. The strength of exciton-LO-phonon coupling was deduced from the energy shift of exciton emission with temperature variation. The reduction of the coupling strength of exciton-LO-phonon may originate from a diminution in the exciton Bohr radius making the exciton less polar, which could be explained by the dopant-induced increase of the exciton binding energy.

## 7.2 Prospective

Due to numerous unique properties expected in the low-dimensional system, nanometer-scale materials promise to be important in the next-generation optoelectronic devices. Low-dimensional ZnO nanostructures, such as quantum dots (QDs) [1,2], nanoparticles (NPs) [3,4], nanobelts [5], nanowires [6], and quantum wells [7], have been widely investigated for the feasible requirement. In particular, ZnO QDs and NPs are of great interest because of the three-dimensional confinement of carrier and phonon leads not only continuous tuning of the optoelectronic properties but also improvement in device performance. Nevertheless, the surface of QDs is usually composed of uncoordinated atoms, which make the QDs highly active and quench the PL emission. Recently, Demangeot *et al.* [4] have reported the low-temperature PL from ZnO NPs with different particle sizes which were synthesized by a RT organometallic method. The study showed no shift from the low-temperature PL measurement indicated that UV emission was most likely dominated by weakly bound localized defects, which could come from the surface-bound ionized acceptor-exciton complexes, rather than the size-dependent quantum confinement effect. It is therefore important to note that the nanocrystals synthesized by chemical methods indeed occasionally cause the product suffering the active surround, which could intensely transform the intrinsic properties of the core. Accordingly, the demand for surface passivation of the NPs and the QDs is significant. Overcoating the QDs with higher bandgap inorganic materials has been shown to improve the luminescence by suppressing surface nonradiative recombination centers. In these regards, considerable researches have been devoted to the core-shell structure QDs, including CdSe/ZnSe [8], InAs/CdSe [9], Si/SiO<sub>2</sub> [10], and PbSe/PbS QDs [11]. It is known that the band gap of ZnO can be tuned by alloying with MgO; we have



discussed the detailed characteristics of ZnO:Mg alloys in this dissertation. Therefore, similar efforts for the ZnMgO QDs and ZnO/MgO core-shell QDs are strongly demanded from both the fundamental scientific research and photonic application points of view.

Bose-Einstein condensation (BEC) of an ideal gas of bosons has been the subject of intense study in excitonic and atomic systems. Excitons and biexcitons are bosons at low densities. Ideal bosons exhibit a so-called BEC at sufficiently low temperature and high density. BEC is a macroscopic population of one state in  $k$ -space, generally  $k = 0$ . The appearance of an excitonic condensed phase in bulk crystals and quantum-well (QW) structures has been the major subject: Experiments on Cu<sub>2</sub>O are considered to be quite promising.[12-14] In GaAs/AlAs coupled QW's, an anomalous transport behavior of indirect excitons under high magnetic fields, which suggests excitonic superfluidity, was reported.[15,16] A possibility of the condensation of weakly localized excitons in GaAs/Al<sub>x</sub>Ga<sub>1-x</sub>As double QW's was experimentally proposed.[17] With the advent of semiconductor QWs, the possibility of observing the quantum statistics of bosons in two-dimensional systems has been raised. An interesting situation of Bose-Einstein statistics in a QW was reported by Kim and Wolfe [18]: a two-component gas system of excitons and biexcitons. They showed theoretically and experimentally that a well-known square law of the density relation between excitons and biexcitons is modified by Bose-Einstein statistics. Assuming thermal equilibrium between excitons and biexcitons, there exists a situation in which the equilibrium chemical potential ( $\mu$ ) comes close to the biexciton energy per electron-hole pair  $E_{\text{BEX}}/2$ , i.e.,  $E_{\text{BEX}}/2 - \mu \leq kT$ , where  $E_{\text{BEX}}/2$  is lower than the exciton energy ( $E_{\text{EX}}$ ) by a half of the biexciton binding energy. In such a situation, the biexciton density is governed by the strongly

increasing part of the Bose-Einstein distribution function, while a saturation of the exciton density occurs, leading to the appearance of a threshold-like increase of the biexciton density. This behavior can be understood from Bose-Einstein statistics of the exciton-biexciton system. It was experimentally demonstrated from time-resolved PL spectra in the decay processes of excitons and biexcitons in a GaAs QW [18] and GaAs/AlAs superlattice [19] at a bath temperature of 2 and 5 K, respectively. Therefore, time-resolved PL measurements are capable of investigating BEC effect for the bosons. However, there are no reports to our knowledge on the phenomena with a BEC of exciton-biexciton in ZnO-based structures. The precise information of the exciton-biexciton density relationship at various excitation powers and bath temperatures estimated from the line-shape analysis of time-resolved PL spectra will be a long-term goal.



## References

- [1] V. A. Fonoberov and A. Balandin, *Appl. Phys. Lett.* **85**, 5971 (2004).
- [2] K. A. Alim, V. A. Fonoberov, and A. Balandin, *Appl. Phys. Lett.* **86**, 053103 (2005) ; K. A. Alim, V. A. Fonoberov, M. Shamsa, and A. Balandin, *J. Appl. Phys.* **97**, 124313 (2005).
- [3] L. Guo, S. Yang, C. Yang, P. Yu, J. Wang, W. Ge, and G. K. L. Wang, *Appl. Phys. Lett.* **76**, 2901 (2000).
- [4] F. Demangeot, V. Paillard, P. M. Chassaing, C. Pagès, M. L. Kahn, A. Maisonnat, and B. Chaudret, *Appl. Phys. Lett.* **88**, 071921 (2006).
- [5] Z. W. Pan, Z. R. Dai, and Z. L. Wang, *Science* **291**, 1947 (2001).
- [6] M. H. Huang, S. Mao, H. Feick, H. Yan, Y. Wu, H. Kind, E. Weber, R. Russo, and P. Yang, *Science* **292**, 1897 (2001).
- [7] T. Makino, C. H. Chia, N. T. Tuan, H. D. Sun, Y. Segawa, M. Kawasaki, A. Ohtomo, K. Tamura, and H. Koinuma, *Appl. Phys. Lett.* **77**, 975 (2000).
- [8] M. Danek, K. F. Jensen, C. B. Murray, and M. G. Bawendi, *Chem. Mater.* **8**, 173 (1996).
- [9] Y. W. Cao and U. Banin, *J. Am. Chem. Soc.* **122**, 9692 (2000).
- [10] W. L. Wilson, P. F. Szajowski, and L. E. Brus, *Science* **262**, 1244 (1993).
- [11] M. Brumer, A. Kigel, L. Amirav, A. Sashchiuk, O. Solomesch, and N. Tessler, E. Lifshitz, *Adv. Funct. Mater.* **15**, 1111 (2005).
- [12] D. W. Snoke, J. P. Wolfe, and A. Mysyrowicz, *Phys. Rev. B* **41**, 11 171 (1990).
- [13] E. Fortin, S. Fafard, and A. Mysyrowicz, *Phys. Rev. Lett.* **70**, 3951 (1993).
- [14] J. L. Lin and J. P. Wolf, *Phys. Rev. Lett.* **71**, 1222 (1993).
- [15] L. V. Butov, A. Zrenner, G. Abstreiter, G. Böhm, and G. Weimann, *Phys. Rev. Lett.* **73**, 304 (1994).

- [16] L. V. Butov and A. I. Filin, Phys. Rev. B **58**, 1980 (1998).
- [17] E. S. Moskalenko, V. V. Krivolapchuk, and A. L. Zhmodikov, Fiz. Tverd. Tela (St. Petersburg) **42**, 1492 (2000) [Phys. Solid State **42**, 1535 (2000)].
- [18] J. C. Kim and J. P. Wolfe, Phys. Rev. B **57**, 9861 (1998).
- [19] H. Ichida and M. Nakayama, Phys. Rev. B **63**, 195316 (2001).



# 潘晴如簡歷 (Vita)

## 基本資料

姓名：潘 晴 如 (Ching-Ju Pan)

性別：女

出生年月日： 1977 年 02 月 13 日

籍貫：高雄市

永久通訊處：(804) 高雄市鼓山區大順一路 432 巷 46 號

email:[chingju.eo90g@nctu.edu.tw](mailto:chingju.eo90g@nctu.edu.tw);  
[chingjupan@yahoo.com.tw](mailto:chingjupan@yahoo.com.tw)

## 學歷：

1995.9 – 1999.6 私立中原大學物理系 學士

1999.9 – 2001.6 國立交通大學電物所 碩士

2002.9 – 2008.1 國立交通大學光電所 博士

## 博士論文題目：

摻鎂氧化鋅材料之激子-聲子交互作用研究

Influence of phonons on excitonic characteristics in  
Mg-incorporated ZnO

## Publication list

### I. Refereed Journal Publications:

1. **Ching-Ju Pan**, Kuo-Feng Lin, Wei-Tse Hsu, and Wen-Feng Hsieh, “Reducing exciton-longitudinal optical phonon coupling with increasing Mg incorporation in MgZnO powders”, *Journal of Applied Physics*, 102, 123504 (2007).
2. **Ching-Ju Pan**, Kuo-Feng Lin, and Wen-Feng Hsieh, “Acoustic and optical phonon assisted formation of biexcitons”, *Applied Physics Letters*, 91, 11907 (2007).
3. **Ching-Ju Pan**, Kuo-Feng Lin, Wei-Tse Hsu, and Wen-Feng Hsieh, “Raman study of alloy potential fluctuations in  $Mg_xZn_{1-x}O$  nanopowders”, *Journal of Physics-Condensed Matter*, 19, 186201 (2007).
4. **Ching-Ju Pan**, Hsu-Cheng Hsu, Hsin-Ming Cheng, Chun-Yi Wu, and Wen-Feng Hsieh, “Structural and optical properties of ZnMgO nanostructures formed by Mg in-diffused ZnO nanowires”, *Journal of Solid State Chemistry*, 180, 1188 (2007).

### II. Conference:

1. **Ching-Ju Pan**, Kuo-Feng Lin, Wei-Tse Hsu and Wen-Feng Hsieh, “Abnormal phonon modes and alloy potential fluctuations in  $Mg_xZn_{1-x}O$  nanostructures”, in Conference of Year 2007 Annual Meeting of Chinese Physical Society, Chunli, TAIWAN, oral paper (2007).
2. **Ching-Ju Pan**, Hsu-Cheng Hsu, and Wen-Feng Hsieh, “Stimulated emission of ZnMgO sponges formed by simple diffusion MgO capped ZnO nanowires”, in Proceedings of Optics and Photonics Taiwan'05, Tainan, TAIWAN, oral paper (2005).
3. **Ching-Ju Pan**, Wei-Hao Chiu, Hsin-Min Cheng, Hsu-Cheng Hsu, Chun-Yi Wu, and Wen-Feng Hsieh, “Artificial Structure Color”, the design image for the cover competition of Materials Today (2005).
4. **Ching-Ju Pan**, Hsu-Cheng Hsu, and Wen-Feng Hsieh, “Structural effect on optical properties of ZnO inverse opal photonic crystals”, Taiwan Nano Tech, post paper (2005).